

ANALYSIS OF LARGE SCALE PV SYSTEMS WITH ENERGY STORAGE
TO A UTILTIY GRID

A Thesis
Presented to
the Graduate School of
Clemson University

In Partial Fulfillment
of the Requirements for the Degree
Master of Science
Electrical Engineering

by
Joseph M. Lavalliere
May 2016

Accepted by:
Dr. Elham Makram, Committee Chair
Dr. Randy Collins
Dr. Ramtin Hadidi

ABSTRACT

With electric distribution network operators experiencing an exponential increase in distributed energy resource connections to the power grid, operational challenges arise attributable to the traditional methods of building distribution feeders. Photovoltaic (PV) solar systems are the major contributor due to recent technological advancements. Though this renewable energy resource is beneficial to human society, unfavorable electrical conditions can arise from the inherent variability of solar energy. Extreme variability of power injection can force excessive operations of voltage regulation equipment and potentially degrade customer voltage quality. If managed and controlled properly, battery energy storage systems installed on a distribution feeder have the ability to complement solar generation and dampen the negative effects of solar generation.

Now that customers are connecting their own generation, the traditional design assumption of load flowing from substation to customer is nullified. This research aims first to capture the maximum amount of generation that can be connected to a distribution feeder. Numerous deployments of generation scenarios are applied on six unique distribution feeders to conclude that hosting capacity is dependent on interconnect location. Then, existing controllers installed on voltage regulation equipment are modeled in detail. High resolution time series analysis driven from historical measurements is conducted on two contrasting feeders with specific PV generator deployments. With the proper modeling of on-load tap changer controls, excessive operations caused by extreme PV generation swings were captured.

Several services that battery energy storage systems can provide when connected to an individual distribution feeder with significant PV generation include long term absorption of excessive PV generation, dynamic response to extreme PV generation ramping, and release of stored energy for system peak shaving. A centralized master energy coordinator is proposed with the ability to dispatch the battery system in such a fashion to implement each service throughout consecutive days of operation. This solution was built by integrating load and solar energy forecasting predictions in order to construct an optimum charging and discharging schedule that would maximize the asset's lifespan. Multiple load and solar generation scenarios including a consecutive three day run is included to verify the robustness of this energy coordinator.

ACKNOWLEDGMENTS

I would like to thank my advisor, Dr. Elham Makram, for providing me the opportunity to expand my knowledge of the power systems industry and her unwavering support and encouragement throughout my journey. I would also like to thank the Dr. Lubkeman and David Mulcahy of North Carolina State University for their collaborative discussions related to the work towards one of the first CAPER projects named “Distribution Planning Criteria and Tools for Future Distributed Energy Resource Penetration Scenarios using Probabilistic Approaches”. Finally, I would like to thank my committee members, Dr. Randy Collins and Dr. Ramtin Hadidi as well as the CAPER and CUEPRA Industry members for providing the necessary resources needed to complete my work and their valuable feedback and support.

TABLE OF CONTENTS

	Page
TITLE PAGE	i
ABSTRACT.....	ii
ACKNOWLEDGMENTS	iv
LIST OF TABLES	vii
LIST OF FIGURES	viii
 CHAPTER	
I. INTRODUCTION	1
1.1: Thesis Outline	1
II. IMPACT OF PV ON PEAK LOAD SHAVING AT CLEMSON UNIVERSITY	4
2.1: Introduction of the Campus Distribution System	4
2.2: System Description and Historical Data Used.....	6
2.3: Critical Day Selection.....	8
2.4: Simulation Architecture and Modelling	10
2.5: Analysis of Proposed PV-DG Deployments on CUCS	17
III. FEEDER HOSTING CAPACITY OF DISTRIBUTED GENERATION...	23
3.1: Distribution System Design Characteristics	23
3.2: Supervised Analysis of DER-PV Impacts	32
3.3: Load Level Selection for DER-PV Hosting Capacity Analysis	37
3.4: Iterative Static Hosting Capacity Analysis	41
3.5: Distribution System Characteristics Impact to DER-PV H.C.	46
IV. CAPTURING DER-PV IMPACTS TO VOLTAGE REGULATION MECHANISMS	57
4.1: Distribution System Volt/VAR Control Schemes	57
4.2: Centralized Integrated Volt-VAR Control.....	72
4.3: Quantifying the Level of Variability of DER-PV	80

4.4: DER-PV Impact to Voltage Regulation Equipment Operations	90
V. COORDINATED CONTROLLER BETWEEN VOLTAGE REGULATION DEVICES AND LARGE SCALE BESS ON UTILITY DISTRIBUTION SYSTEMS	100
5.1: The Need for a Distributed Energy Resource Management and Forecasting Controller	100
5.2: A Novel Master Energy Coordinator Reliant on BESS and DER-PV Operation	107
5.3: Distribution Equipment Controllers under the Master Energy Coordinator	122
5.4: Benchmarking the Centralized MEC and Associated Field Agent Controllers	131
REFERENCES	144

LIST OF TABLES

Table	Page
2.1 CUCS System Loads and PV POI Locations	7
2.2 Modeled Cable Characteristics	12
2.3 Selected PV Module Characteristics.....	15
2.4 PV-DG Location and Electrical Properties.....	18
3.1 Proportions of Three-Phase Conductor Ampacity	26
3.2 Summary of POI Locations & Tested Injection Levels.....	34
3.3 Summary of Seasonal Load Averages and Standard Deviations.....	40
3.4 Summary of Hosting Capacity Algorithm Performance.....	44
3.5 Results of Least Squares Regression	53
4.1 Voltage Regulation Device Settings	75
4.2 Daily PV Plant Generation Categorized by DARR	87
5.1 Proposed Daily Energy Yield Linear Model Regression Results.....	116
5.2 Input Output Data Point Tags of an OLTC & SC Controller	123
5.3 Selected Advanced Lead Acid Battery Bank Characteristics	132

LIST OF FIGURES

Figure	Page
2.1	Clemson University Campus System One Line Diagram.....5
2.2	Net Load Characteristics with 5.5MVA GT and Proposed PVAs 8
2.3	Feeder 5B Daily Peak Percent PV-DG Penetration..... 9
2.4	Interaction between MATLAB and Simulink..... 10
2.5	Power Flow Percent Error per CUCS Feeder..... 13
2.6	Solar Angles Depiction 14
2.7(a)	Estimated and Measured Real Power of Node 33 PVA on 3/30/14..... 16
2.7(b)	Estimated and Measured Real Power of Node 33 PVA on 9/05/14..... 16
2.8	PV Estimation Function and Model Interaction 17
2.9(a)	Visualization on the Types of Proposed PVA Installations PV1 Rooftop Design 18
2.9(b)	Visualization on the Types of Proposed PVA Installations PV4 Canopy Design Rendering 18
2.10	Net System Load on 3/30 from 7:00am to 8:00pm 19
2.11	PV penetration on Feeders 4, 5B, and System from 7:00am to 8:00 pm 20
2.12(a)	Peak Penetration Time Instance on 3/30: Apparent Power Profiles 20
2.12(b)	Peak Penetration Time Instance on 3/30: Voltage Profiles 20
2.13	Net System Load on 9/05 from 7:00am to 8:00pm 21

List of Figures (Continued)

Figure	Page
2.14 DG Penetration of Feeder 3, 4, 5, and PCC from 7:00am to 8:00pm	21
2.15(a) Peak Penetration Time Instance on 9/05: Apparent Power Profiles	22
2.15(b) Peak Penetration Time Instance on 9/05: Voltage Profiles	22
3.1(a) 2014 pdf of Ambient Temperature in Western NC	27
3.1(b) 2014 pdf of Wind Speed in Western NC	27
3.2(a) Ampacity Rating Dependency on Operating Conditions Loading vs. Operating Temperature	28
3.2(b) Ampacity Rating Dependency on Operating Conditions Ambient Temperature vs Ampacity	28
3.3(a) Topology and Conductor Phasing of Test Feeder 01.....	29
3.3(b) Topology and Conductor Phasing of Test Feeder 02.....	29
3.3(c) Topology and Conductor Phasing of Test Feeder 03.....	29
3.3(d) Topology and Conductor Phasing of Test Feeder 04.....	29
3.3(e) Topology and Conductor Phasing of Test Feeder 05.....	29
3.3(f) Topology and Conductor Phasing of Test Feeder 06.....	29
3.4(a) Comparison of Loading Characteristics: Connected Phase Unbalance	30
3.4(b) Comparison of Loading Characteristics: Customer Type Proportions	30
3.5 System Design Characteristics of Analyzed Feeders.....	31
3.6 Simplified CYME Model of Feeder 04	33

List of Figures (Continued)

Figure	Page
3.7(a) Supervised CYME DG Hosting Capacity Results of Zone 2: Voltage Profile Impacts	33
3.7(b) Supervised CYME DG Hosting Capacity Results of Zone 2: Apparent Power Impacts	33
3.8 Feeder 04 VREG Zones Under Testing	34
3.9(a) Scenario 5 Results of Utility-Scaled DG Connection: Voltage Profile Impacts	35
3.9(b) Scenario 5 Results of Utility-Scaled DG Connection: Real Power Impacts	35
3.10(a) Scenario 1 & 3 Comparison: S1 Voltage Impacts	35
3.10(b) Scenario 1 & 3 Comparison: S3 Voltage Impacts	35
3.11 OpenDSS Feeder Model Architecture	36
3.12(a) Compilation of Historical SCADA Data Annual Distribution of Feeder Load	38
3.12(b) Compilation of Historical SCADA Data Monthly Averages between 10AM-4PM.....	38
3.13(a) Seasonal Comparison of 2014 Load between Feeders Summer kW Distributions	39
3.13(b) Seasonal Comparison of 2014 Load between Feeders Winter kW Distributions.....	39
3.14(a) Daytime Average and +/- 2 Standard Deviations with Monthly CSI Summer Peak Solar Time Instances	41
3.14(b) Daytime Average and +/- 2 Standard Deviations with Monthly CSI Winter Peak Solar Time Instances	41
3.15 Detailed Hosting Capacity Flow Chart	42

List of Figures (Continued)

Figure	Page
3.16(a) Permissible POI Locations on Feeder 01	43
3.16(b) Permissible POI Locations on Feeder 03	43
3.17(a) Feeder 03 Single-Phase Voltage Impacts: No DER-PV	45
3.17(b) Feeder 03 Single-Phase Voltage Impacts: 1.2MW DER-PV	45
3.18(a) Simulation Results for Feeder 01 under Minimum Load- Bus Voltage Violations	45
3.18(b) Simulation Results for Feeder 01 under Minimum Load- Conductor Loading Violations.....	45
3.19(a) Captured Max Bus Voltage at Each Iteration: Feeder 02	47
3.19(b) Captured Max Bus Voltage at Each Iteration: Feeder 03	47
3.20(a) Percent of Locations with Violations: Feeder 02.....	47
3.20(b) Percent of Locations with Violations: Feeder 03.....	47
3.21(a) Sensitivity to DG Capacity with Mean Loads: Voltage Violations	49
3.21(b) Sensitivity to DG Capacity with Mean Loads: Ampacity Violations	49
3.22(a) Sensitivity to DG Capacity with Min. Loads: Voltage Violations	49
3.22(b) Sensitivity to DG Capacity with Min. Loads: Ampacity Violations	49
3.23(a) Seasonal Shift in the DG Hosting Capacity on Feeder 01: Voltage Violations	50
3.23(b) Seasonal Shift in the DG Hosting Capacity on Feeder 01: Ampacity Violations	50

List of Figures (Continued)

Figure	Page
3.24(a) Minimum DER-PV Capacity Dependency of Distance From Substation on Feeder 02	51
3.24(b) Minimum DER-PV Capacity Dependency of Distance From Substation on Feeder 03	51
3.25(a) Second Order Model Prediction Results: Feeder 01	53
3.25(b) Second Order Model Prediction Results: Feeder 02	53
3.26(a) Maximum Allowed DER-PV Size under Average Summer Load on Feeder 02	54
3.26(b) Maximum Allowed DER-PV Size under Average Summer Load on Feeder 03	54
3.27 Compilation of Critical Levels of DER-PV Hosting Capacity	55
4.1 Autotransformer Equivalent Circuit	58
4.2 Annual Simulation Algorithm Flowchart	62
4.3 One Minute Real and Reactive Power Derivative	63
4.4 Reactive Power of DSCADA, Switch Capacitor, and Derived	64
4.5 Derived Historical Switch Capacitor Operations on Feeder 03	65
4.6 Annual QSTS Daily Average Single Phase P & Q Errors	66
4.7 MATLAB Implemented VRR Sequential Control	67
4.8 Time-Integrating VRR Control Mode	68
4.9 Voltage Averaging VRR Control Mode	69
4.10 Annual Distribution of OLTC Control Voltage on Feeder 03	70
4.11 Annual OLTC Tap Position Differential per Control Scheme	70

List of Figures (Continued)

Figure	Page
4.12 Difference in OLTC Controller Responses.....	71
4.13 Location of Voltage Regulation Equipment on Feeder 04	75
4.14 Annual Switch Capacitors Historical Operations on Feeder 04.....	76
4.15 Annual Derived Reactive Power Demand on Feeder 04	76
4.16 Single Phase P & Q on Feeder 04 during a Summer Week.....	77
4.17 Error of Powers between DSCADA and OpenDSS on Feeder 04.....	78
4.18 Reactive Power of Feeder 04 and Switch Capacitors During a Summer Week.....	78
4.19 OLTC/SVRs Tap Positions on Feeder 04	79
4.20 PV Plant Locations of Annual Measurements	81
4.21 CSI and B_{ncl} Profiles on Sample Days.....	83
4.22 Sampled Days of Increasing VI at Site 03	85
4.23 Relationship between VI & CI at Site 03.....	85
4.24 SNL Solar Day Classification Scheme	86
4.25 Relationship between Site 03 VI & Site 04 DARR	88
4.26 Cumulative Probability of Site 04's Ramp Rates	88
4.27 DARR Category 5 Days Ramp Rate Distribution per DER-PV Site.....	89
4.28(a) DER-PV Point of Interconnections Test Locations on Feeder 02.....	90

List of Figures (Continued)

Figure	Page
4.28(b) DER-PV Point of Interconnections Test Locations on Feeder 03.....	90
4.29 Observed Solar Energy and Daytime Load Metrics	91
4.30 Monthly Observed Solar Variability Metrics	92
4.31(a) Cumulative Daily OLTC Tap Changes on Feeder 02.....	93
4.31(b) Cumulative Daily OLTC Tap Changes on Feeder 03.....	93
4.32(a) Voltage Deviations during Select Days on Feeder 03- DOY=34, VRR Control Voltage	94
4.32(b) Voltage Deviations during Select Days on Feeder 03- DOY=34, OLTC Tap Position.....	94
4.32(c) Voltage Deviations during Select Days on Feeder 03- DOY=101, VRR Control Voltage	94
4.32(d) Voltage Deviations during Select Days on Feeder 03- DOY=101, OLTC Tap Position.....	94
4.33 Impact of Connected DER-PV to Feeder 03 Load on a One Week Span.....	95
4.34 Observed Voltage Range during Peak Solar Interval on Feeder 03.....	95
4.35(a) Example from Feeder 02: P.U. Voltage Deviation	97
4.35(b) Example from Feeder 02: P.U. Voltage Deviation Index Aggregation	97
4.36(a) Average Daytime Voltage Deviation Index: Feeder 02.....	97
4.36(b) Average Daytime Voltage Deviation Index: Feeder 03.....	97
4.37(a) Maximum Impact Day on Feeder 03: Five Second TVDs	98

List of Figures (Continued)

Figure	Page
4.37(b) Maximum Impact Day on Feeder 03: Total Feeder Power.....	98
4.38(a) Feeder 03's Daily Average TVD Relationship CI & DARR Solar Energy Dependency.....	99
4.38(b) Feeder 03's Daily Average TVD Relationship CI & DARR Solar Variability Dependency.....	99
5.1 Duck Chart Example at the Distribution Feeder Level.....	101
5.2 MEC-F1 Process Topology.....	108
5.3 Methodology in Obtaining BESS Charge Rate Schedule.....	110
5.4 Projection of PAR_{CB} and Resulting SoC Limit.....	111
5.5 Winter and Summer Solstice CSI and B_{ncI} Profiles	112
5.6(a) BESS Operation Schedule during Solar Generation Window – Charge Rate	113
5.6(b) BESS Operation Schedule during Solar Generation Window – State of Charge	113
5.7 MEC-F2 Process Topology.....	114
5.8 Relationship between Solar Coefficients and Observed DER-PV Normalized Daily Energy Yield.....	115
5.9 MEC-F2 Formulation of Target DoD Enforced during Peak Shaving Mode	117
5.10 Resulting Target DoD from a Static Annual Simulation of MEC-F2	118
5.11 MEC-F3 Process Topology.....	119
5.12 A Three Day Snapshot (2/3 – 2/5) for Testing the MEC's Functionality	120

List of Figures (Continued)

Figure		Page
5.13	Master Energy Coordinator I/O Scheme.....	121
5.14	Communication Architecture of Incorporating a MEC and BESS	122
5.15	Feeder On-Load Tap Changer Time Sequential Controller.....	124
5.16	Switch Capacitor Reactive Power Controller	124
5.17	BESS Controller Logic & Topology.....	125
5.18	Four Daily Samples of DER-PV Five Second Real Power Derivatives	127
5.19	BESS Controller A - Enabled during Solar Generation.....	129
5.20	BESS Controller B - Enabled during a Peak Loading	130
5.21	Feeder 03 Topology and Point of Interconnection Locations of Proposed DER-PV & BESS	133
5.22	Results of Example #1 (5/24/2014) – Stable DER-PV with Evening Peak and High Projected Next-Day Solar Energy	135
5.23	Results of Example #2 (10/15/2014) – Highly Variable DER-PV with Evening Peak and High Projected Next-Day Solar Energy	136
5.24	Results of Example #3 (2/3/2014) – Variable DER-PV with Evening Peak and High Projected Next-Day Solar Energy	137
5.25	Results of Example #4 (11/23/2014) – Low DER-PV with Morning Peak and High Projected Next-Day Solar Energy	138
5.26	Results of a Consecutive Three Day Run (2/3 to 2/5)	141

CHAPTER ONE

INTRODUCTION

1.1 Thesis Outline

Throughout this manuscript, the impacts of distributed energy resources including photovoltaic generation systems and battery energy storage systems connected on electric distribution feeders are explored. From utilizing power flow software packages including MATLAB's SimPowerSystems toolbox, Eaton Corps' CYME, and EPRI's OpenDSS, static and time series power flow computations were initiated on either a full Clemson University distribution system model or six individual distribution feeders provided by the sponsored utility. The overall research efforts can be broken down into four distinct stages, each providing essential insights into potential operational challenges when integrating solar PV facilities on a distribution network.

The first stage consisted of deploying acceptable locations of PV systems throughout the Clemson University main-campus distribution system. The PV facility outputs were derived from historical one second solar irradiance and ambient temperature measurements. The real and reactive power consumed by the individual campus buildings were driven from historical measurements taken on the individual distribution transformers and extracted from an internally managed historian. The possibility of peak shaving occurring with these PV facilities in operation was explored with and without the existing natural gas combustion turbine generator in operation.

The second stage consisted of a review of the technical constraints associated with the allowable maximum generation capacity specific to a certain point of interconnect.

These included voltage and conductor ampacity limits. An iterative algorithm was implemented to test all possible locations where a centralized solar PV facility could be built creating numerous power injections levels. During each scenario, the maximum observed bus voltage and line loading percentage was captured. After conducting this automated process on all six test feeders, significant distribution design characteristics impacting the minimum hosting capacity were explored on top of providing a simplified summary of the allowable distributed generation (DG) capacity ranges.

The third stage consisted of constructing architecture to automate a quasi-static time series (QSTS) power flow simulation utilizing again OpenDSS. In order to capture an accurate representation of the negative impacts variable solar generation can have on voltage regulator tap changes, the simulation was driven off of complete historical measurements of real and reactive power taken at the head-of-feeders and existing PV facilities' point-of-interconnection locations. This procedure was verified from capturing the mean single phase errors of an annual simulation. Three voltage regulator control modes, sequential, time-integrating, and voltage averaging, were modeled and compared via annual simulations. Selecting a sequential control mode and running a key time span within a year, excessive tap operations from connected centralized PV facility deployments were captured. During post analysis, additional metrics were compared including the solar irradiance variability index; clear-sky index; daily aggregate ramp rate; additional daily tap changes; and voltage deviation index.

Lastly, the fourth stage consisted of introducing a large-scale battery energy storage system (BESS) on a 12.47kV distribution feeder with a 3MW PV facility

connected miles away from the substation. Beneficial services this BESS can provide to distribution network operators include energy time shifting, dynamic responses to extreme power ramp rates in order to dampen the voltage variation observed by the on-load tap changer, and lastly discharge the recently captured energy during the most beneficial time of day assumed to be the peak loading period.

A centralized master energy coordinator implemented at the substation was proposed to accomplish these operational goals. The interaction of each function within the coordinator is explained in detail, highlighting the required inputs necessary to construct the scheduled charge and discharge rates of the BESS. This coordinator was designed to be adaptive to the next-day's projected load and solar generation by adjusting the schedules to utilize the BESS to its fullest potential. To verify the centralized coordinator, results from four single day QSTS simulations were provided with each day presenting a unique scenario of load and solar generation. Conclusively, results from a consecutive three day QSTS simulation were provided to highlight the full functionality of this advanced DER coordination technique and the plausible integration into a future distribution management system.

CHAPTER TWO

IMPACT OF PV ON PEAK LOAD SHAVING AT CLEMSON UNIVERSITY

2.1 Introduction of the Campus Distribution System

Universities who manage their own distribution feeders are facing a unique opportunity to decrease their annual electric energy consumption. Electrical systems energizing academic, research, and resident buildings typically have outdated switchgears, transformers, and conductors in dire need of replacement to accommodate an ever increasing load. Clemson University's main campus encompasses a total of 1,400 acres with over 140 buildings, supporting a population of over 20,000 students. This provides ample space for the implementation of renewable generation. In 2015 alone, four projects are underway totaling 1,000,000 ft² of building space, introducing new energy demands to an already constrained electric distribution system.

Upgrades to this distribution system are inevitable but some could be avoided if properly placing DG facilities at critically congested areas. Solar PV has become the most viable option for on-campus DG due to the availability of building rooftops/parking lot areas, a decrease in PV system prices, an increase in electricity rates, and an overall concern about the environment. With Clemson's expected future load increase, another positive impact that PV-DG can introduce is peak shaving. Additional DG power injected during the daylight hours can typically overlap a daily peak load. To test this concept, a MATLAB/Simulink model of the Clemson University Campus System (CUCS) was obtained from previous work presented in [1]. A novel algorithm is built to integrate PV-DG at viable locations utilizing localized load and solar irradiance measurements.

2.2 System Description and Historical Data Used

The CUCS civil and electrical characteristics were provided by Clemson University utility services (CUUS) which included building load locations, cable data, and distribution transformers (DTs) data. Following this information, the system is constructed as seen in Figure 2.1. A 44/12.47 kV transmission retail substation is located at bus 0, considered the point of common coupling (PCC) with the utility. The system operates at a nominal voltage level of 12.47kV with an annual system peak load of 25MVA. It has seven main feeders, five radial and two looped, with the two older 4kV feeders aggregated at their respected 12.47/4.16kV substations (nodes 1 and 123). Nine tie switches were modeled with one normally closed between nodes 135 and 162 connecting Feeders 1 & 2. One 5.5MVA gas turbine (GT) generator is used for peak shaving at node 124. In addition, one 15 kW photovoltaic array (PVA) exists at node 33. Overall, the Simulink model consisted of 201 line sections or 16.52 miles of conductor resulting in 170 nodes with 70 capturing three phase V-I measurements.

The majority of the buildings on campus have three phase services with dedicated DTs ranging from 30kVA to 1500kVA that step down to a utilization voltage of either 480V or 208V. Schneider Electric Prologic monitoring devices were installed at 125 locations throughout campus measuring both the initial lines coming out of the main substation and individual building three phase loads. A local database managed by Schneider Electric's power monitoring expert tool created by StruxtureWare [2] records the telemetered data every 15 minutes and stores for future use. Three phase real and reactive power are extracted from all the 125 installed locations on only selected days

throughout 2014. The Simulink model of this system has 106 sets of single-phase series RLC (constant P,Q) loads connected to the node numbers listed in Table 2.1.

Table 2.1: CUCS System Loads and PV POI Locations

Node Number	Description	Node Number	Description
0	Duke Energy 44kV Source	75	Poole Ag. Building
1	4.16kV System East	77	Rhodes Hall
5-17	Lightsey Bridge Apartments	78	Riggs Hall
20	PV10	79	Riggs Hall, BSMT
21	Biosystems Research Complex	81	Stadium Suites
23	Godley-Snell Research Center	84	Fike Rec. Center/PV6
25	Band Practice Field	88-101	Memorial Stadium
27	Service and Support	99	PV5
30-31	Hinson CWP	103	Jervey Athletic Center
33	Fluor Daniel/PV1	105-108	D. Kingsmore Stadium
34	Harris A. Smith Building/PV3	110,112-113	Rugby Fields
37	PV4	115	Pump Station
38	PV9	116-117	Rowing Boathouses
42-43	Littlejohn Coliseum (1)	123	4.16kV System West
45,47	Littlejohn Coliseum (2)	124-132	Central Energy Facility
50	Life Sciences Center	134	President's Home
53-54	East Chiller Facility	136	Byrnes Hall
56-57	Brooks Center	138-148	Calhoun Courts
58	Strom Thurmond Institute	152	Redfern Health Center
61	Hendrix Student Center	154	Edwards Hall
63	Daniel Hall	156	Schilletter Hall
64	Barre Hall	159	Vickery Hall
66	McAdams Hall	160	Jordan Hall
67	McAdams Hall-Annex/PV2	162	Manning Hall
68	Lehotsky Hall/PV7	165	Sikes Hall
70	Lee Hall/PV8	166	Alumni Center
71	Academic Success Center	168	Kinard Annex
73	Rhodes Hall Annex	169	Long Hall

Monitoring real-time weather conditions of Clemson, SC is accomplished by utilizing synced weather sensors located on the roof of Riggs Hall. The installed

instruments include a digital thermometer to measure the ambient temperature (T_a) [°C] and most importantly a pyranometer to measure direct beam solar irradiance G_D [W/m²]. These units produce one second analog measurements which are fed through a CR1000 Datalogger, converting the signals to a digital serial format for transfer and storage. All measurements are stored to a local SQL database. From this, data samples of the timestamp, ambient temperature, and direct beam solar irradiance were extracted using the MATLAB-Database Toolbox before data quality algorithms were applied.

2.3 Critical Day Selection

Running simulations on every day of the year would require a large computational time and be cumbersome to extract all the required datasets. To test how the CUCS can handle a significant penetration of PV-DG, key times of the year are selected based on the historical annual system loading characteristics as portrayed in Figure 2.2.

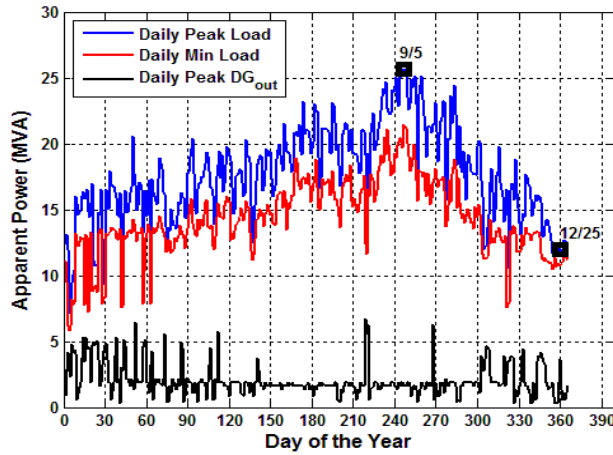


Figure 2.2: Net load characteristics with 5.5MVA GT and Proposed PVAs

Two critical times are selected to assess the impacts of PV-DG installations [3], the maximum percent penetration of generation to load and the peak loading condition. The first critical day occurs when there is the maximum percentage of PV (MP-PV)

experienced on the system compared to load [3]. Feeders 4 and 5B are selected to integrate PV-DG rooftop and parking lot facilities after the utility services conducted a civil survey. Feeder 5B is selected for this calculation due to it having a historically smaller load and a greater proposed PV-DG capacity. A historical annual load profile of Feeder 5B and the generation of the PVA at node 33 were obtained at 15 minute intervals. An estimation of the total feeder PV-DG performance is found by converting the 15kW PVA output to per-unit before scaling up to the feeder's proposed capacity.

$$\%PV_{DG} = \frac{\sum_{i=1}^5 S_{i,PV}(t)}{S_{5B,Load}(t)} \quad (2.1)$$

To arrive at this critical day, Eq. (2.1) is applied at each time interval and the daily maximum percent penetration is selected and displayed in the figure below.

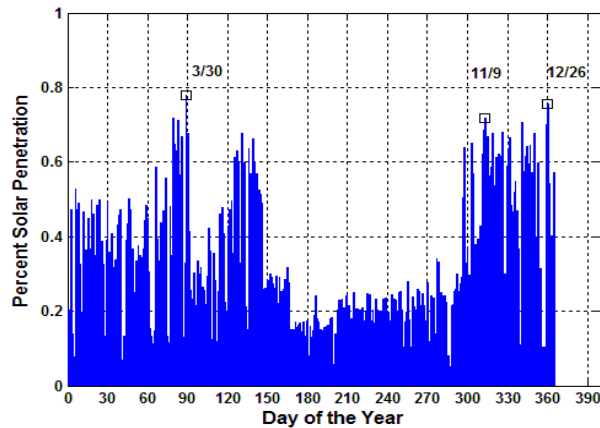


Figure 2.3: Feeder 5B Daily Peak Percent PV-DG Penetration

The percent solar penetration was significantly higher during the spring and winter seasons due to substantially lower loading. Taking into account the irradiance data quality of potential days, 3/30/2014 is selected to simulate the MP-PV of feeder 5B, with a maximum percent solar penetration of approximately 79%.

To arrive at the second critical day, the daily coincident maximum and minimum system real power is concluded and displayed in Figure 2.2. The daily peak DG output of the GT and 15kW PVA is displayed in black. From observation, spikes signifying GT operation typically occurred during the winter months when the regional grid's time-of-use rate was the highest. After disregarding any CUUS generation days, 9/5/2014 is concluded to have the peak loading condition of the year with approximately 25MVA. On this Friday, classes were in session and the ambient air temperature reached 80°F with high humidity resulting in a large air conditioning load and lower power factor (PF).

2.4 Simulation Architecture and Modelling

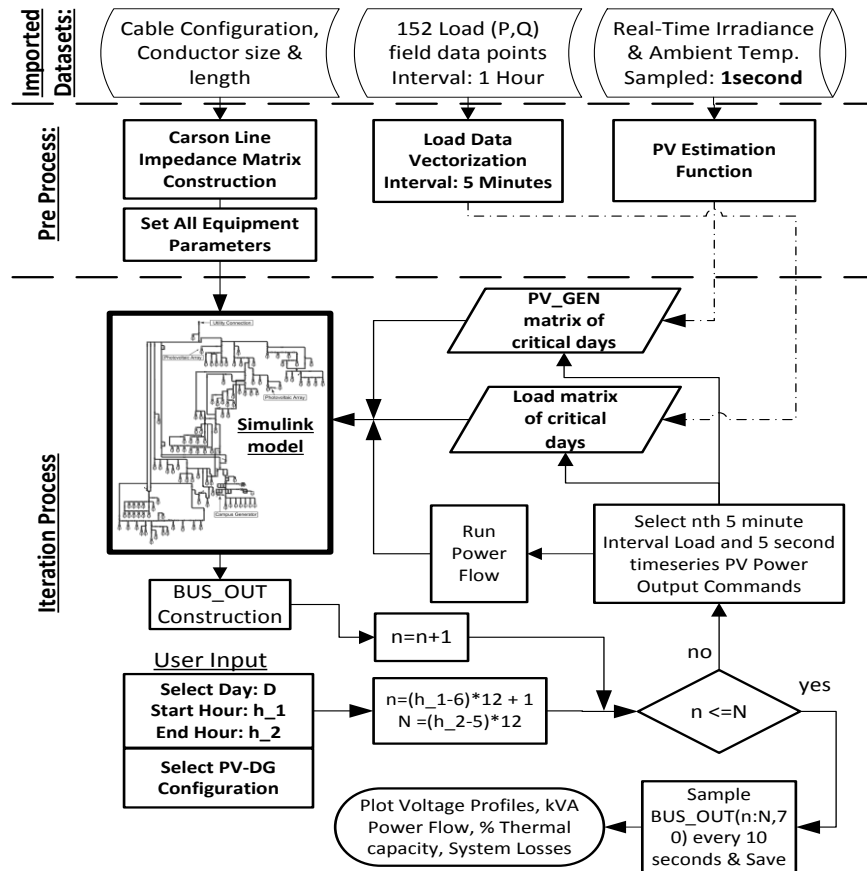


Figure 2.4: Interaction between MATLAB and Simulink

Now that it has been concluded the two critical days for simulation in 2014 are 3/30 and 9/5, a MATLAB algorithm is built to interact with the Simulink model as shown in Figure 2.4. The algorithm can be divided into three main stages; import datasets, preprocess, and iteration process. For the import datasets stage, three main datasets are acquired and imported. This includes all system parameters, (15-min.) recorded load profiles, (1-sec.) solar irradiance, and (1-sec.) ambient temperature readings. Built functions processed these three datasets to set system parameters, assign historical measurements to corresponding Simulink loads, and estimate PV-DG generation output.

In the construction of system parameters, an Okonite MV-105 datasheet [4] is referenced to obtain the cable design and electrical characteristics needed to properly model the existing cables. It is assumed that phase conductors are tape shielded and positioned in a triangular configuration; inside underground cable trays or conduit. An unshielded neutral conductor is to be in the middle of this configuration. Applying these assumptions on configuration and cable design, Carson's line equations are used to construct the raw impedance matrix for each type of conductor [5]. Then, each matrix is Kron reduced to only include the phase conductor's impedances. Because the three-phase PI section line element is used to model these cables, a change-of-basis matrix is applied to convert to symmetrical components. Table 2.2 presents the calculated positive and zero sequence resistances, inductances, and capacitances for each type of conductor used. Overall reach of each conductor type is also provided making it apparent that 350kcmil was dominantly used for the backbone of these feeders.

Table 2.2: Modeled Cable Characteristics

Conductor Size (AWG/KCM kcmil)	Total Reach (km)	Thermal Limit (A)	Positive Seq. Resistance (R_1) [Ω /km]	Positive Seq. Inductance (L_1) [mH/km]	Positive Seq. Capacitance (C_1) [μ F/km]
#2	7.054	200	0.601	0.4708	0.1257
1/0	1.683	215	0.380	0.4459	0.1452
4/0	0.663	315	0.192	0.3947	0.2092
350	16.99	415	0.120	0.3766	0.2619
500	0.192	500	0.087	0.3710	0.2817
750	0.014	614	0.062	0.3556	0.3371

In regards to the assignment of historical measurements to corresponding Simulink loads, the first step is to interpolate measurements from 15 to 5 minute intervals. This enables the capture of a more accurate relationship between load and potentially highly variable PV generation. Due to the system typically having three phase loads, the unbalance between phases is typically 1-3%. Therefore for simplicity, balanced three phase loads are assumed with power measurements dividing evenly among phases.

When PV-DG facilities are installed on distribution feeders, it is vital that the simulation model represents the physical system to guarantee an accurate study. Using telemetered readings, hourly power consumption data of all seven feeders are extracted during the peak loading conditions. To verify the campus model, power flow calculation is run from 7:00am to 7:55pm and the percent errors (PE) of real and reactive power flow based on Eq. (2.2) are presented in Figure 2.5.

$$PE(t, n) = \frac{TELE(t, n) - SIM(t, n)}{TELE(t, n)} \cdot 100\% \quad (2.2)$$

The PCC real and reactive powers PE are consistently around 7% and 4%, respectively. One aspect that needs to be noted is the quality of incoming telemetered data. On multiple occasions, building load measurements result in negative reactive power. This suggests that the measurement equipment (PTs and CTs) are not properly installed and the phasing is incorrect. Therefore, this percent error was deemed acceptable to complete an assessment of PV-DG impact and peak load shaving.

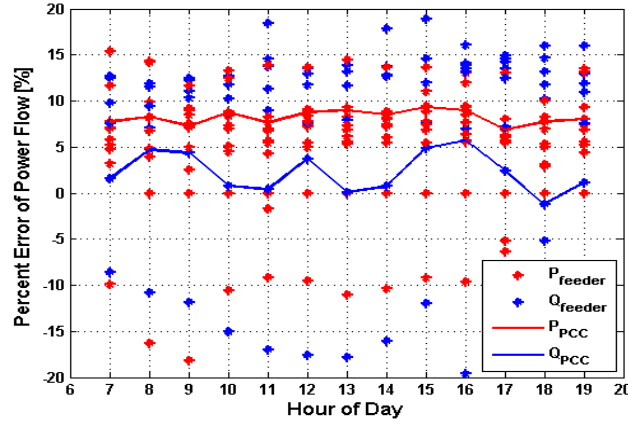


Figure 2.5: Power Flow Percent Error per CUCS Feeder

The third pre-function accepts the one second weather conditions datasets and derives estimated 60 second PV output power. The irradiance measurements acquired from Riggs Hall are of direct beam radiation (G_D) from a vertical fixture. The proportion of G_D striking the surface of a PVA depends on the solar incidence angle (θ). This proportion can be calculated using Eq. (2.3), accepting four dependent variables derived from site location and panel orientation [6].

$$\cos \theta = \cos \beta \cdot \cos(\phi_s - \phi_c) \cdot \sin(\Sigma_c) + \sin \beta \cdot \cos(\Sigma_c) \quad (2.3)$$

$$G_{BC} = G_D \cdot \cos(\theta) \quad (2.4)$$

From observing the orientation of the existing Fluor Daniel 15kW PVA (node 33) it was assumed that the Azimuth angle (ϕ_c) is -25° while the Tilt angle (Σ_c) is known to be 30° . Note that these angles were held constant when applying to other proposed PVA sites. Two additional angles explain the position of the sun known as the solar altitude and azimuth angles. The solar Altitude (β) is the vertical angle between the sun and the ground. The solar Azimuth (ϕ_s) represents the location of the sun in relation to due south as depicted in Figure 2.6. It is assumed an angle in the southeast direction is positive.

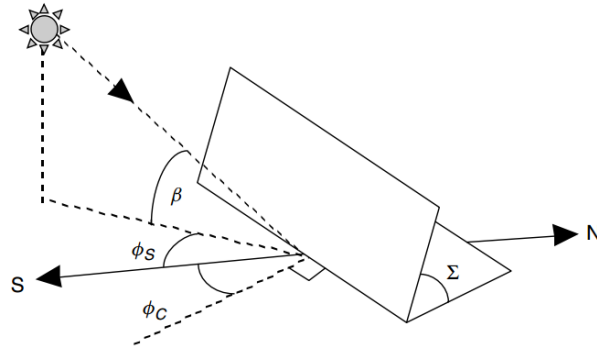


Figure 2.6: Solar Angles Depiction

The direct beam radiation (G_{BC}) based on Eq. (2.4) is the most significant proportion of the total solar irradiance (G_C) colliding on the PV panel surface. There are also two other forms of radiation; diffused (G_{DC}) and reflected (G_{RC}). Threlkeld and Jordan [6] developed a model to estimate the proportion of incoming radiation scattered by atmospheric moisture particles or reflected by clouds. A Diffusion Factor (C), as shown in Eq. (2.5), is used to represent this proportion of direct beam radiation. Observing the PVA Tilt angle with C , the diffused radiation is found by applying Eq. (2.6).

$$C = 0.095 + 0.04 \cdot \sin \left[\frac{360}{365} (n - 100) \right] \quad (2.5)$$

$$G_{DC} = G_B \cdot C \cdot \left(\frac{1 + \cos(\Sigma_C)}{2} \right) \quad (2.6)$$

Reflected radiation is the third component of G_C and is the least insignificant. This solar insolation depends on the local ground reflectance (ρ), of which ordinary ground has a reflectance of 0.2 [6]. Using this assumption, the reflected radiation was estimated using Eq. (2.7). Aggregating all three types of possible solar radiation, Eq. (2.8) will provide an estimate of the total solar radiation colliding on the surface of a given PVA.

$$G_{RC} = I_B \cdot \rho \cdot (C + \sin \beta) \left(\frac{1 + \cos(\Sigma_C)}{2} \right) \quad (2.7)$$

$$G_C = G_{BC} + G_{DC} + G_{RC} \quad (2.8)$$

The power generated by a PVA is the product of multiple factors including solar cell efficiency, temperature de-rates, PVA surface area, and balance of system (BOS) losses. While referencing an Amersco [7] solar panel's electrical characteristics as summarized in Table 2.3, the power generated is estimated using Eq. (2.9) [8]. The BOS efficiency is assumed to 80% (k_{BOS}) which includes losses from the connection wiring and the dc/ac inverter [9].

$$P_{PVA}(G_C, T) = k_1 \cdot A_S \cdot G_C (1 - k_T \cdot (T - T_{STC})) \cdot N_{PVM} \cdot k_{BOS} \quad (2.9)$$

Table 2.3: Selected PV Module Characteristics

Parameter	Symbol	Value	Unit
Maximum Power	P_{max}	190	W
Module Efficiency	1.683	15.20%	N/A
Temperature Coefficient	0.663	-0.5%	1/°C
Surface Area	16.99	1.2537	m ²
Reference Temperature	0.192	25	°C

To verify this procedure, the estimate of the Fluor Daniel PVA is compared to the telemetered 15minute power readings on 3/30 and 9/05. The blue points in Figure 2.6 are the measurements from on-campus telemetry equipment with accuracy of the nearest kW. The red line represents the PVA estimated output. Verifying this procedure, the overall trends of estimated kW closely follow the measurements but present more variability.

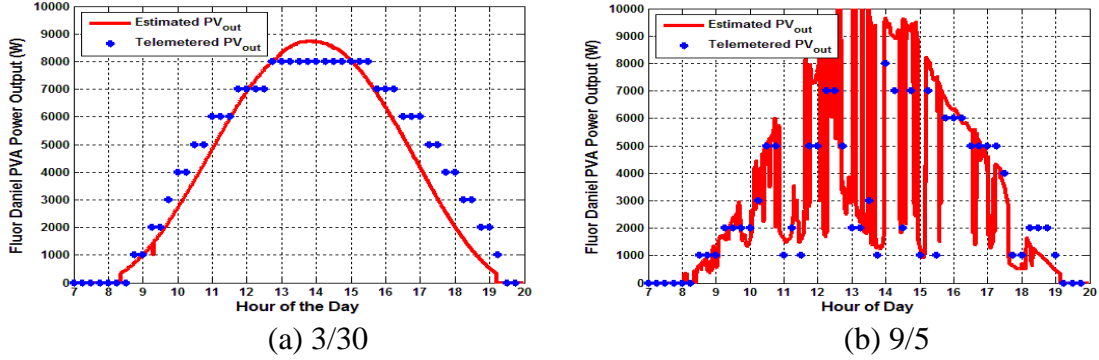


Figure 2.7: Estimated and Measured Real Power of Node 33 PVA

A constant power model is used to represent the PVA systems because it can accurately control a desired operating point under steady state conditions. Figure 2.7 provides the overall process flow of the PVA model controlled by incoming power commands ($P_{PV}^*(t)$ and $Q_{PV}^*(t)$) derived from Eq. (2.6).

$$\left| V_{\phi}^*(t) \right| = \left| \frac{\left(P_{PV}^*(t) + Q_{PV}^*(t) \right) \cdot \frac{2}{3}}{V_{m,\phi_a}(t-1)} \right| \cdot X_{PV} + V_{m,\phi_a}(t-1) \quad (2.7)$$

To achieve integration of this model within Simulink, a controlled voltage source is connected in series with a reactance (X_{PV}) [10]. For feedback control, the voltage of phase “a” at the output terminals ($V_{m,\phi_a}(t-1)$) is constantly measured and applied to

Eq. (2.7). The result provides a new commanded phase voltage magnitude which is issued to each controlled voltage source.

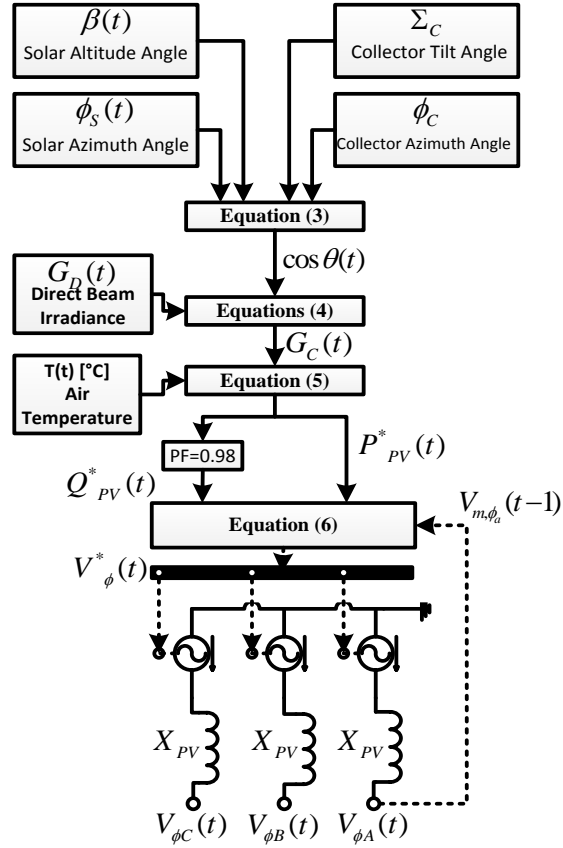


Figure 2.8: PV Estimation Function and Model Interaction

2.5: Analysis of Proposed PV-DG Deployments on CUUS

The constant power PV model is connected at ten locations along the 170 node distribution system as summarized in Table 2.4. The buildings are selected based on results from a CUUS civil survey of rooftop viability and facility capacity is determined from a conservative factor of 4W/ft². Four of these locations are parking lots on-campus, proposing canopy fixtures installed over the parking spots as shown in Figure 2.9(b).



(a) PV1 Rooftop Design



(b) PV4 Canopy Design Rendering

Figure 2.9: Visualization on the Types of Proposed PVA Installations

Table 2.4: PV-DG Location and Electrical Properties

PV-DG Location Name	Node #	Feeder #	Power Capacity [kW]	DT Rating [kVA]	PVA Reactance (X_{pv}) [p.u.]
PV1: Fluor Daniel Building (Rooftop)	33	5B	15	4000	0.05
PV2: McAdams Hall (Rooftop)	67	4	114	1000	0.10
PV3: H.A. Smith Building (Rooftop)	34	5B	20	500	0.05
PV4: P-4 Parking Lot (Canopy)	37	5B	360	500	0.15
PV5: R-3 Parking Lot (Canopy)	99	4	1080	1500	0.30
PV6: Fike Recreation Center (Rooftop)	84	4	45	2000	0.05
PV7: Lehotsky Hall (Rooftop)	68	4	82	1000	0.095
PV8: Lee Hall (Rooftop)	70	4	88.4	500	0.10
PV9: P-3 Parking Lot (Canopy)	38	5B	750	1000	0.25
PV10: C-1 Parking Lot (Canopy)	20	5B	1500	2000	0.35

Now that all proposed PVAs are integrated in the Simulink model and all preprocess functions built, the CUCS is run with the two concluded critical days by having the algorithm iterate the power flow solutions until completion. Due to a computational constraint, the sampled three phase voltage and current values are selected every 10 seconds to decrease the size of the output file. The Simulink environment is simulated using a discrete solution method with a sample time of 0.1 sec. Each power

flow interval extends 300 seconds under a constant P, Q loading condition while the PV output updates every 60 seconds.

Multiple combinations of distributed generation were tested to study the potential peak load shaving on the CUCS utilizing both PV-DG and conventional DG. After running the MP-PV operating condition on 3/30/2014 with and without the PVAs, the impact to net load at PCC is presented in Figure 2.10. At 5:00 pm, the original peak load is 12.479 MW and when the PVAs are in operation, it is dropped to 11.39 MW as represented by the square markers. Larger impacts to load occurred during the early afternoon when demand stabilized but PV was in peak operation.

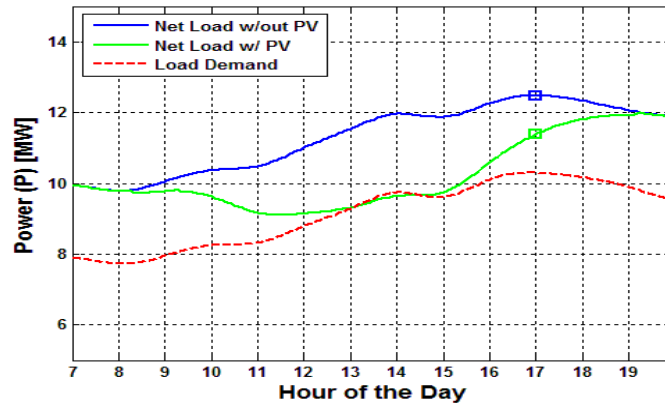


Figure 2.10: Net System Load from 7:00am to 8:00pm

Since all proposed PV-DG are connected to Feeders 4 and 5B, their net upstream demand before and after interconnection is selected and the maximum percent penetration is represented by square markers shown in Figure 2.11. Feeder 5B has an irregular shape due to the load drastically increasing during the middle of the day while Feeder 4 remains relatively flat.

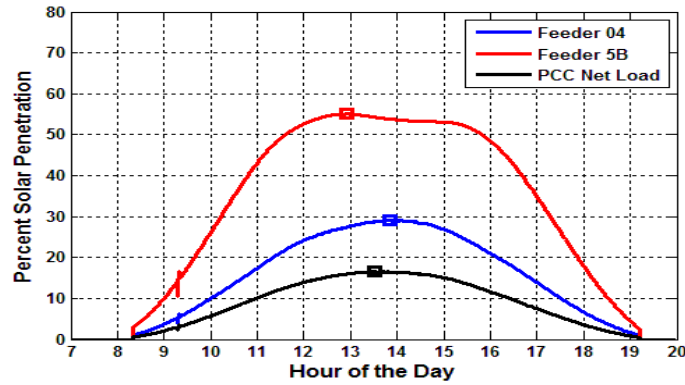


Figure 2.11: PV penetration on Feeders 4, 5B, and System from 7:00am to 8:00 pm

It is observed that the net load has a maximum percent penetration of 16.5% at 1:30PM even though Feeder 4's maximum occurs at 1:50 pm with 29.1% and Feeder 5B's maximum occurs at 12:55 pm with 55.0%. Figure 2.12 provides the apparent power flow and node voltages captured on the two feeders at their respected MP-PV times.

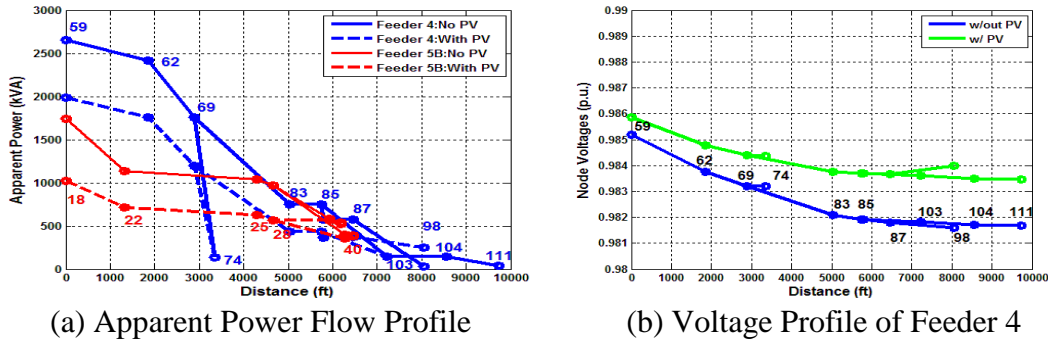


Figure 2.12: Peak Penetration Time Instance on 3/30

Notice how the voltage at node 98, which has a 1,080kW PVA connected to it, rises significantly compared to the rest of the feeder. Nodes 94-101 serve a seasonal load of the Clemson Memorial Football Stadium therefore it is typically minimally loaded. When the PVA is in operation, the feeder head power flow decreases while at node 98 it increases approximately to 480kVA, thus increasing overall voltage.

Moving onto the peak load shaving study with PV-DGs and the local GT, the peak loading day (9/5) of the CUCS has a maximum power demand occurring at 11:05AM of 21.325MW. To reduce this, the 5.5MVA GT is set in operation from 8:15am to 5:30pm using a previous runs dataset recorded on 8/7. This date is selected to capture the drop in efficiency of the GT from high ambient temperatures and humidity. The impact on the net load of the system is shown in Figure 2.13. With GT in operation, the peak loading condition dropped to 17.568 MW.

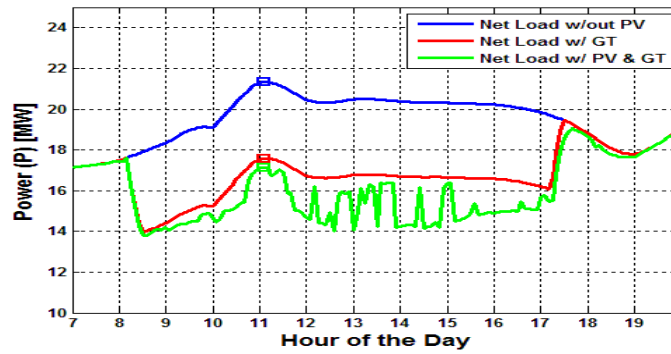


Figure 2.13: Net System Load of Peak Day from 7:00am to 8:00pm

Another case was run with the GT and the PV-DGs in operation using the irradiance dataset portrayed in Figure 2.7 (b). Following the previous simulation procedure with the exception that there are multiple kinds of DG in operation, the times of maximum percent DG penetration can be found in Figure 2.14.

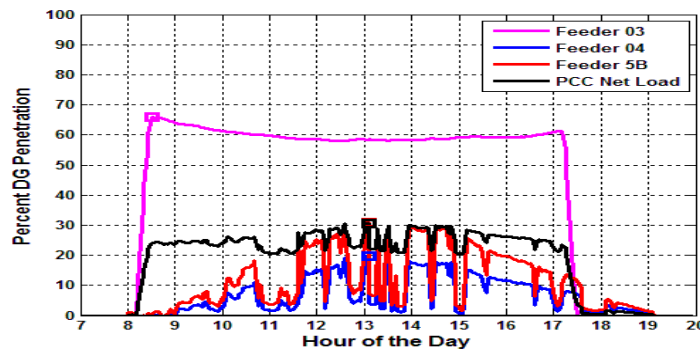
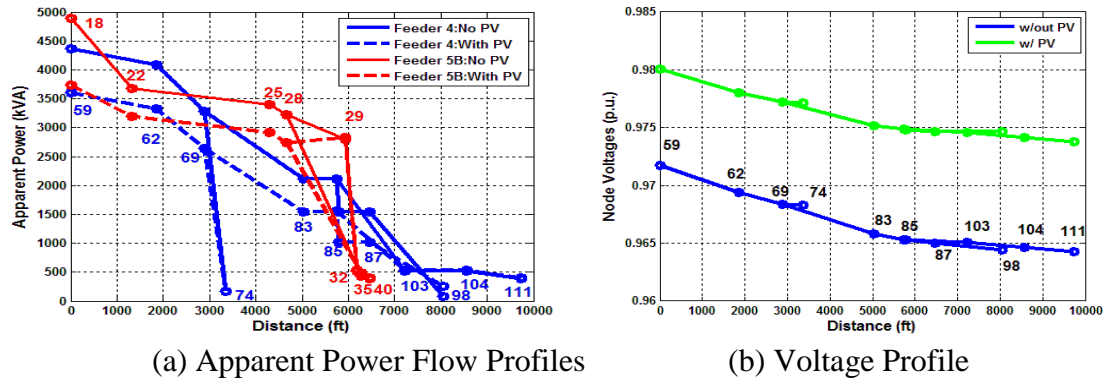


Figure 2.14: DG Penetration of Feeder 3, 4, 5, and PCC from 7:00am to 8:00pm

The GT maximum percent penetration occurred at 8:30am with 66% and stayed relatively constant around 60% due to the turbine generating a constant power output with around a 0.9 PF. Feeders 4 and 5B maximum percent penetrations both occurred at 1:10 pm with 19.6% and 30.9% respectively. Extracting power flow and resulting voltage profiles at these instances, Fig. 2.15 shows similar impacts to 3/30 with voltage support.



(a) Apparent Power Flow Profiles (b) Voltage Profile
Figure 2.15: Peak Penetration Time Instance on 9/05

In this study, a practical distribution system was modeled in detail and the impacts of PV-DGs and a 5.5MVA gas turbine DG were analyzed. Two critical days were simulated, the MP-PV and the peak load. The results show the effectiveness of the model and simulation to study the peak load shaving. Beside the steady-state conditions, a dynamic study needs to take place where the power quality and voltage flicker issues are investigated. The campus distribution system can also be reconfigured to support an emergency micro grid where local DG like the GT and PV-DGs, with the support of battery storage, can sustain a proportion of local demand for a period of time.

CHAPTER THREE

FEEDER HOSTING CAPACITY OF DISTRIBUTED GENERATION

3.1 – Distribution System Design Characteristics

Utilities throughout the United States are experiencing a continuous rise in requests from customers to connect their own electric generation. This is in response to favorable state and federal incentive programs in combination with dropping PV manufacturing and installation costs. As of September 2015, there was a national total of 9,968 megawatts (MW) of installed utility-scale Photovoltaic (PV) capacity [11]. A distributed generation (DG) facility is considered utility-scale if it is greater than 1MW. The southwestern part of the U.S. composes 64% of this total while the South Atlantic region currently contributing 11%. North Carolina is the dominant state in this region with approximately 1,500 MW of installed capacity. This state is actually ranked second when totaling newly installed utility scale PV capacity for the past two years [11].

Duke Energy's service territory encompasses the majority of North Carolina, supporting approximately 3.2 million customers. With such a large volume of interconnect requests, distribution system planning engineers are challenged in evaluating these requests at a reasonable rate. Therefore, a project was proposed to the Center for Advanced Power Engineering Research (CAPER), a consortium between Clemson University, North Carolina State University, and University of North Carolina Charlotte, to develop planning criteria and associated tools for accommodating future integration of distributed energy resources including Solar PV (DER-PV) using probabilistic approaches. This project will provide the utility the capability of modeling the impact of

uncertain future DER penetration scenarios and quantify the options on distribution expansion and upgrade schemes in order to accommodate future DER interconnections.

Duke Energy provided CAPER with six test feeders from two different service territories: Duke Energy Carolinas (DEC) and Duke Energy Progress (DEP). The detailed feeder models were built in CYMDIST, a commercial steady-state snapshot power flow tool mainly used for peak loading analysis [12]. These distribution planning CYME models included the characteristics of the following electrical components: substation transformers, Load Tap Changers (LTCs), Line voltage regulators (VREGs), overhead conductors, underground cables, customer spot loads, fuses, capacitors, and lastly sectionalizers. Distribution transformer (DT) parameters and secondary conductor details were neglected in the CYME models due to the lack of resources to model the vast quantity of customer DTs and secondary lines.

In order to initiate the formulation of novel DER planning criteria and tools for distribution planning, a review of the technical constraints including voltage limits and thermal capacity need to take place. These aspects can limit the amount of new DG that can be installed on existing distribution systems. The voltage limit standard imposed in the United States is ANSI C84.1 of which it imposes two sets of ranges for either service or utilization voltage. Since the secondary lines are not modeled, only the service voltage ranges will be observed. At 12.47kV and 22.9kV nominal service voltages, Range A specifies a maximum of 105% of nominal while Range B specifies 105.8% [13]. Therefore when testing a DG's POI location, a maximum voltage limit of 1.05 p.u. or 126V is enforced.

Overhead conductors commonly have three ratings, normal (continuous), long time emergency (LTE), and short time emergency (STE). The normal rating identifies a maximum amount of current that will ensure the risk of failure to be well below a desired level [14]. A LTE rating is the current level which will introduce the same amount of risk as the normal rating but for a limited amount of time. Sudden rises in current will not instantaneously increase the operating temperature and therefore still ensure safe operation. During more severe circumstances, A STE rating is higher than the LTE rating due to its short time frame. An example was developed in [14] to show the current carrying capacity (commonly referred to as ampacity) for a 795 kcmil 26/7 ACSR conductor to be 992A for normal operation at 100°C (continuous), 1140A for LTE at 115°C (3 hours), and 1310A for STE at 125°C (15 minutes). Therefore, it is obvious there is not a defined answer for what ampacity limit should be imposed when testing a DG's POI but typically the continuous ampacity is enforced.

In the past, distribution feeders were built with Aluminum Cable, Steel Reinforced (ACSR) conductor due to their low-cost, dependability, and favorable strength to weight ratio. The strength of ACSR is the result of its physical design with layers of aluminum alloy 1350 wire wrapped around a steel core [15]. The proportion of steel to aluminum can be controlled to provide a desired mechanical strength and ampacity. Today, utilities are replacing longstanding ACSR conductor with concentric lay stranded Aluminum Conductor (AAC) due to its highest conductivity-to-weight ratio out of all available overhead conductors. AAC is built with aluminum alloy 1360-H19

without a steel core. This results in a relatively poor strength to weight ratio with common distribution sizes of AAC having half the breaking strength as ACSR [15].

The type of conductor selected depends on the geographical area or application. If designing for an urban or suburban distribution feeder, AAC is used due to its sufficient thermal characteristics and light weight. ACSR is used in more rural applications when a smaller conductor can be used with longer spans. Within the Duke Energy territory, typical conductor sizes for a 12.47kV distribution feeder backbone are 336 ACSR and 477 AAC for a 22.87kV feeder. These two conductors have an approximate current carrying capacity of 530A and 646A respectively [16]. The ampacities are approximate because the amperage rating is concluded when the conductor is 75°C and in the presence of an ambient temperature of 25°C with wind travelling at 1.4 mph. After categorizing installed three phase conductor on each test feeder based on the continuous ratings and aggregating the total reach of each group, Table 3.1 was constructed. The highest proportion of each ampacity category is highlighted in red, portraying the unique nature of conductor sizes chosen based on load density and topology.

Table 3.1: Proportions of Three-Phase Conductor Ampacity

Feeder #	0 – 199 A (%)	200 – 399 A (%)	400 – 599 A (%)	600 – 799 A (%)	Total Reach (mi)
1	22.55	34.19	42.65	0.61	11.60
2	34.21	23.95	40.33	1.51	6.89
3	57.44	33.01	9.44	0	18.20
4	53.68	10.64	0	35.69	12.69
5	11.43	0.19	27.77	60.61	7.86
6	23.62	0	39.44	36.93	1.38

Heat is generated from the flow of current driving through the conductor's metal resistance which is commonly known as I^2R losses. Additional factors that can affect the conductor temperature and therefore ampacity include ambient temperature and wind speed. To understand the impact of these weather conditions, a 2014 dataset of ambient temperature and wind speed measured at an altitude of 50 meters at a location in western North Carolina was extracted from [17]. Probability density functions (pdfs) are presented in Figure 3.1 to show the annual distribution of weather conditions that the test feeders would operate under. The red vertical lines portray the standard weather conditions of the provided continuous ampacities, highlighting that a higher ambient temperature can more likely occur as opposed to a lower wind speed.

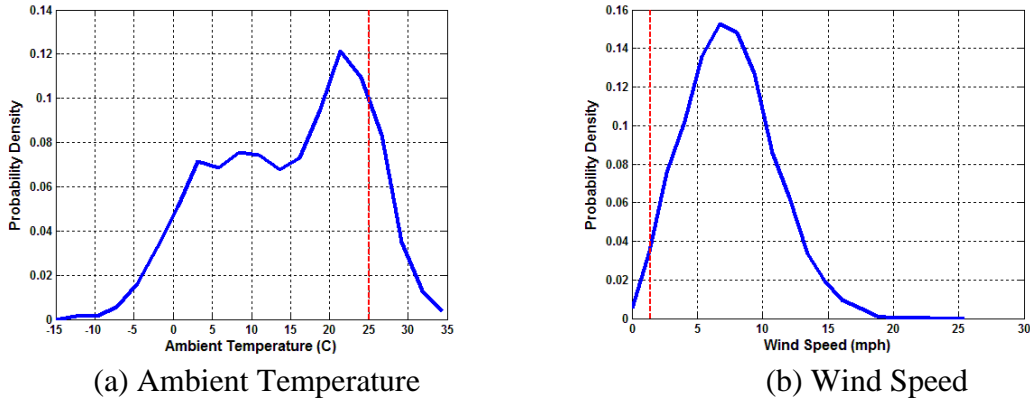


Figure 3.1: 2014 pdf of Weather Conditions in Western North Carolina

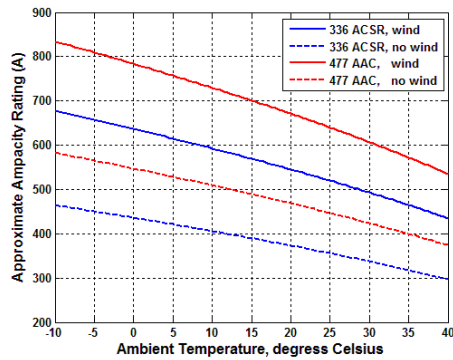
To understand the impact of weather conditions to ampacity, let us first assume a new conductor limit $T_{c,new}$ and a new ambient temperature $T_{a,new}$ is introduced to a conductor. The new ampacity (I_{new}) can be calculated using the equation shown below.

$$I_{new} = I_{old} \cdot \sqrt{\frac{T_{c,new} - T_{a,new}}{T_{c,old} - T_{a,old}}} \quad (3.1)$$

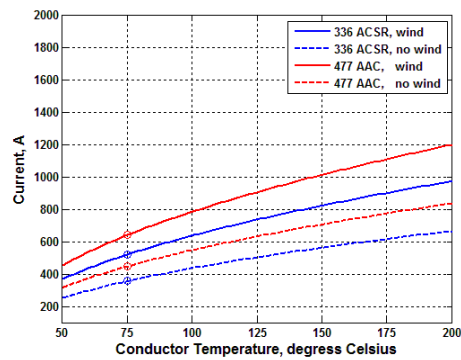
For example, the two common conductor types in DEC and DEP (336 ACSR and 477 AAC) were selected to show the impact of ambient temperature to the ampacity rating. Assuming a conductor operating temperature of 75°C, two conditions were considered: 2.5mph wind and no wind. Figure 3.2 (a) displays the resulting conductor ampacity rating when ambient temperature is varied. From this, it can be concluded that a conductor's ampacity decreases in a non-linear fashion at higher ambient temperatures.

$$T_{c,new} = T_{a,new} + \left(\frac{I_{new}}{I_{old}} \right)^2 \cdot (T_{c,old} - T_{a,old}) \quad (3.2)$$

It is important to consider the maximum operating temperature for a conductor because excess heating causes the aluminum strands to elongate and weaken commonly known as annealing. Slow annealing begins near 100°C and becomes rapid above 200°C [15]. Therefore, it is recommended to operate conductors well below annealing temperature. To show the impact current has on the conductor temperature, Eq. (3.1) is re-arranged to allow the conductor temperature to be calculated based on active current, as shown in Eq. (3.2). Treating the loading or current (I_{new}) as the independent variable, the resulting conductor temperature is portrayed in Figure 3.2 (b).



(a) Loading vs. Op. Temperature



(b) Ambient Temp. vs Ampacity

Figure 3.2: Ampacity Rating Dependency on Operating Conditions

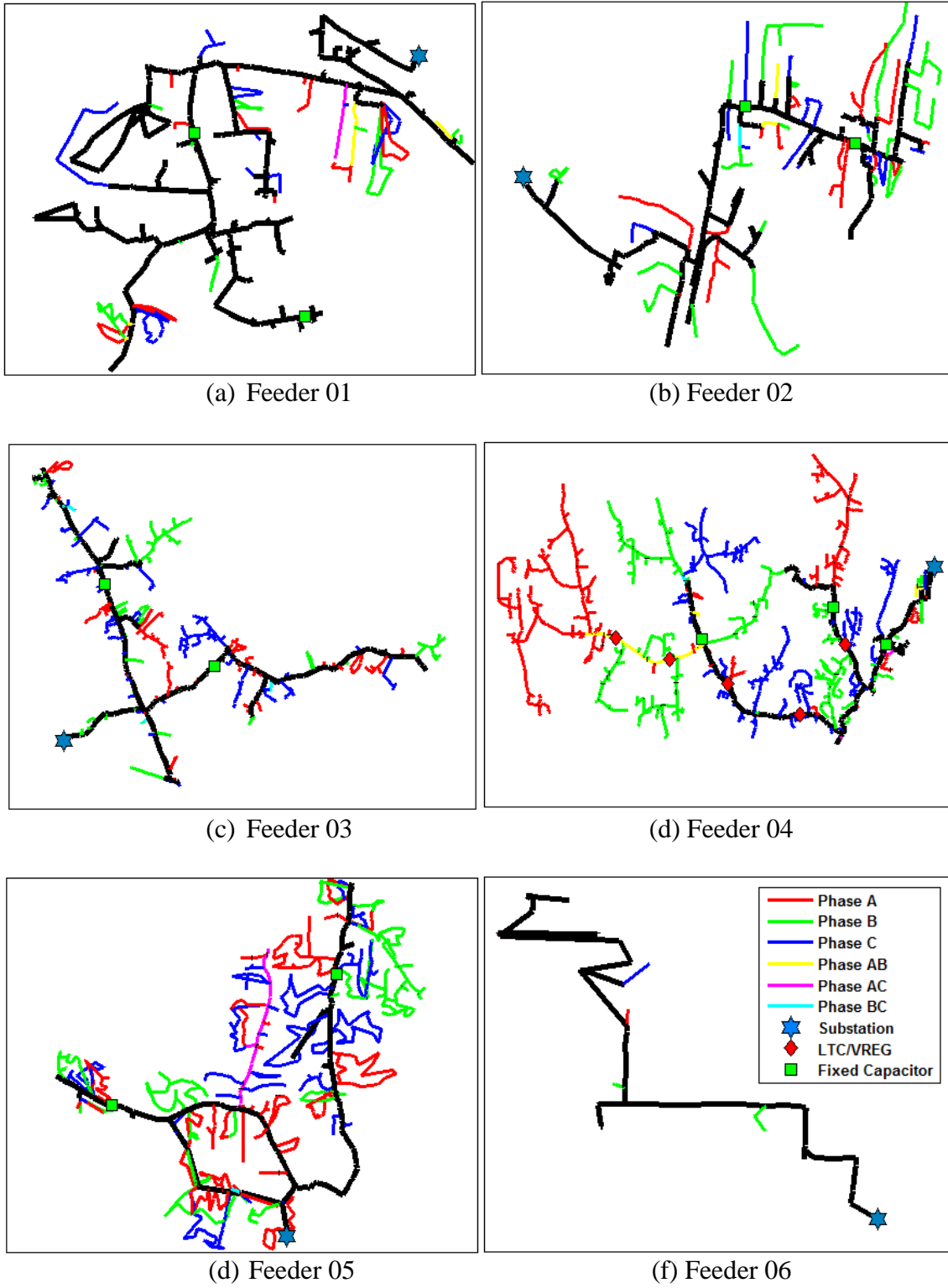


Figure 3.3: Topology and Conductor Phasing of Test Feeders

Unbalanced loading of distribution feeders is very common in the United States due to the dominance of single-phase connections and therefore many single or two phased laterals. From inspection of Figure 3.3 (a-f), it is obvious that these test feeders are no exception. The percentage of connected kVA transformer rating to the total kVA is presented in Figure 3.4 (a) to support this claim. Because Feeder 3 and 5 are severely unbalanced, it is essential that a detailed line model is used that specifies phase and neutral conductor type and configuration. Also understanding the proportion of connected residential to commercial customers can assist in feeder classification which is especially important when introducing a streamlined method for determining DG hosting capacity. Since customer information was not provided, an assumption is made that a transformer rated less than 100kVA is considered a residential load. By enforcing this simple classification scheme, the proportions of customer types are shown in Figure 3.4 (b). After observing how Feeder's 1 and 6 have mostly three-phase lines, it is not surprising that they resulted in the highest proportions of commercial customers.

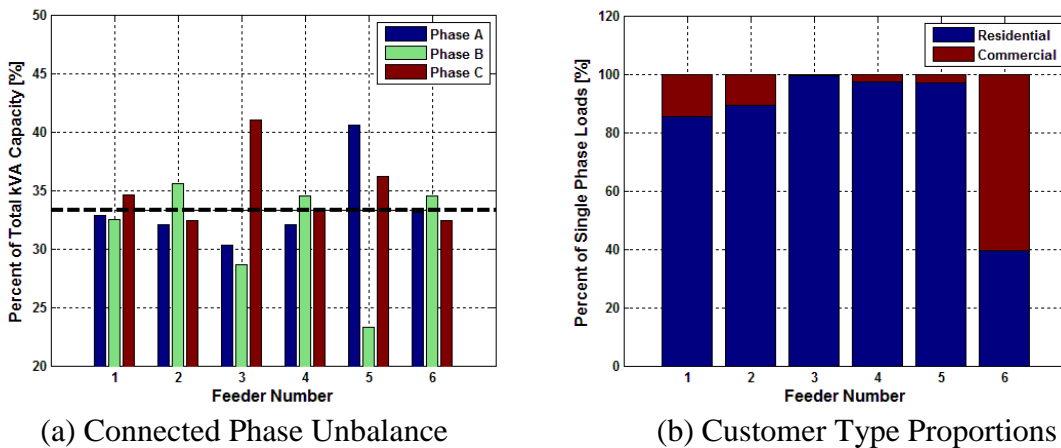


Figure 3.4: Comparison of Loading Characteristics

The impact of an individual distribution feeder's operation from the connection of a DER-PV facility is dependent on the individual feeder's characteristics [18]. Additional factors include annual load shape patterns, PV size, location, and especially annual local solar irradiance profiles. Figure 3.5 was constructed to easily compare main characteristics including voltage class, deployment of voltage regulation equipment (VRE), and feeder peak/valley load with resulting voltage headroom.

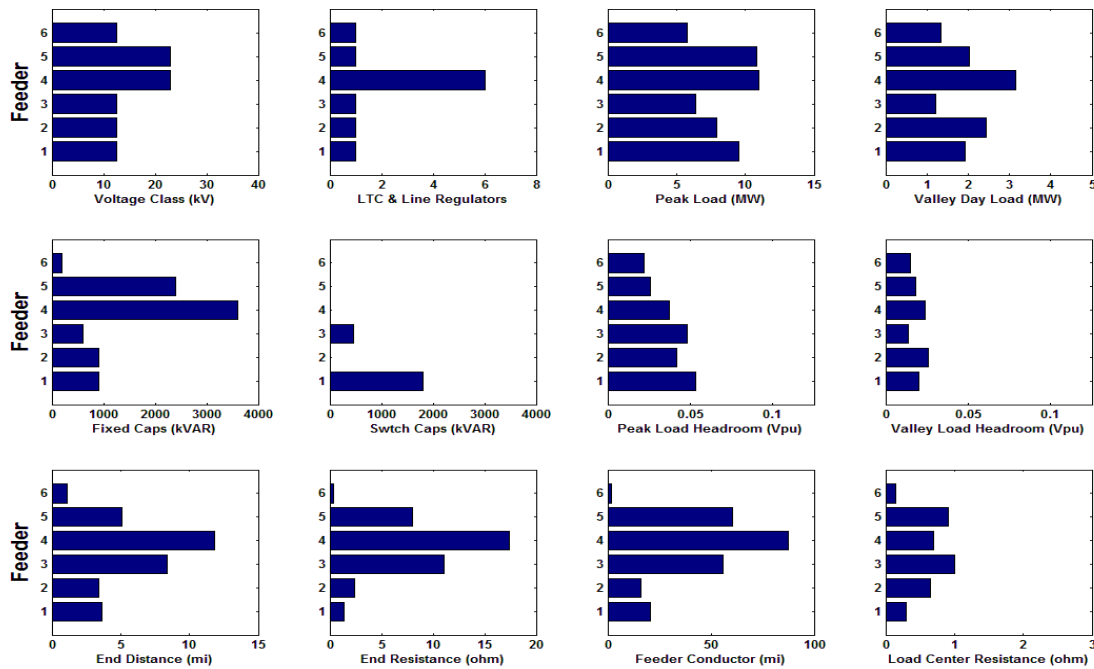


Figure 3.5: System Design Characteristics of Analyzed Feeders

Feeder 04 could be considered an outlier to this group of distribution feeders because it has the greatest number of voltage regulators, installed capacitor capacity, feeder end distance, feeder end resistance, and total modeled conductor span. A load tap changer (LTC) is installed at the head-of-feeder as well as (2) 3-phase line voltage regulators (VREGs), (1) 2-phase VREG, and (2) 1-phase VREGs. On top of this, three 1200kVAR switch capacitors are connected in shunt throughout the circuit evident that a

complex Volt/VAR management structure is in place. Feeder 4 is located within the DEP territory and because of legacy initiatives; two-way communications were integrated on capacitor bank and VREG controllers [19].

3.2 Supervised Analysis of DER-PV Impacts

Feeder 4 was selected to explore the impacts of DG real power injection to a distribution feeder with multiple VREGs connected in series along the main and lateral lines. Initial work consisted of reducing the system to a more conceptual model. This was accomplished by aggregating connected kVA and conductor length per phase within defined sections of line. For simplicity, an apparent length to the equivalent load center was based upon the distribution of individual spot loads. Short laterals were aggregated and modeled as a spot load on the backbone while more significant laterals were modeled in a level of detail similar to the backbone. Additionally, the locations of the voltage regulation equipment dictated when a line section terminated.

Overall, the equivalent system was constructed in CYME as seen in Figure 3.6, consisting of 36 conductor sections with equivalent spot loads and could be divided into five VREG zones. Zone 1 was excluded from future DG Point of Interconnect (POI) test locations because after referring Google Maps, it served a heavily urbanized area with little open land for a utility-scale solar farm. When conducting a permissibility study of DG injection levels, the daytime minimum load of 7.55MVA on April 17th was selected due to the prior analysis in Chapter 2 that a maximum ratio of load to solar generation typically occurs most often in the spring.

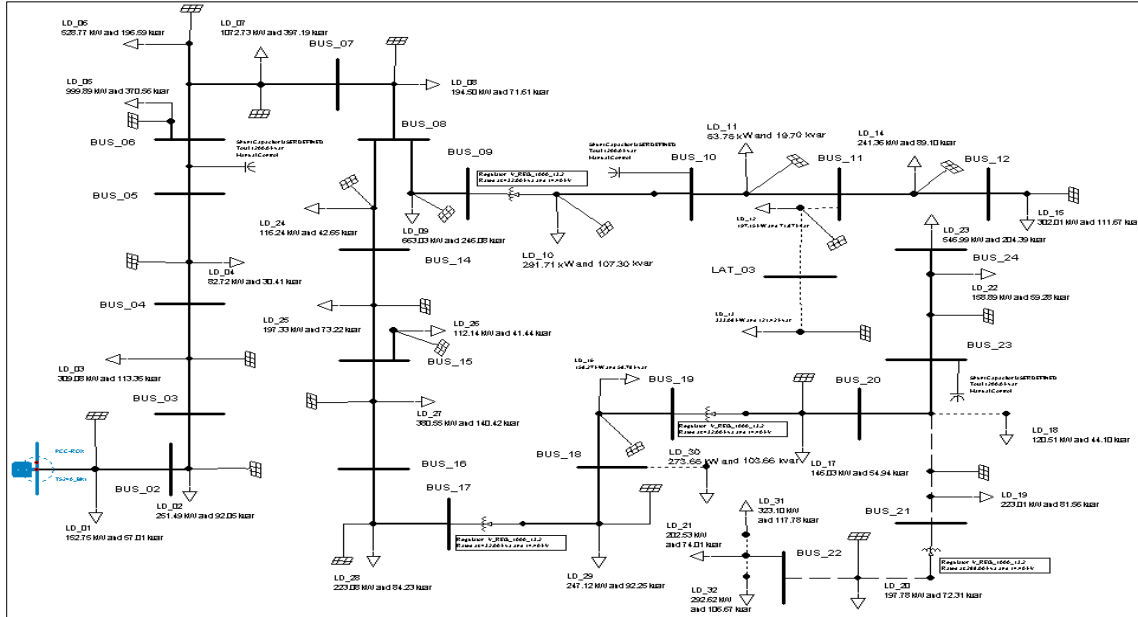
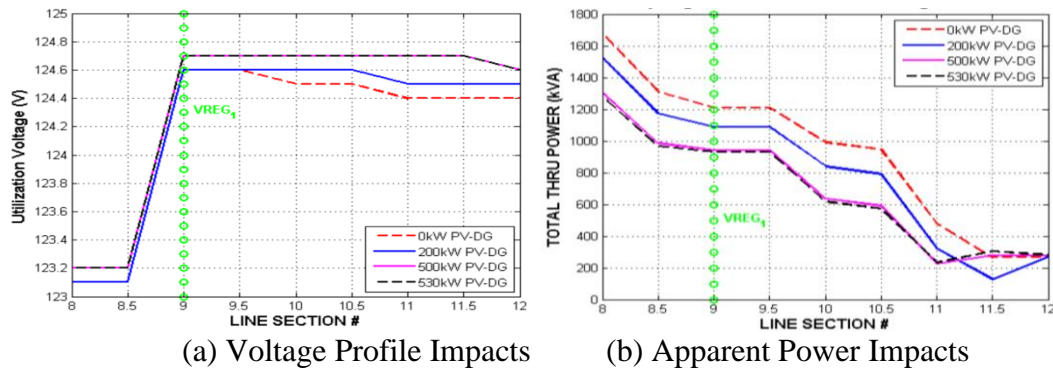


Figure 3.6: Simplified CYME Model of Feeder 4

There were two stages of this permissibility study of DG injection levels, the first solely on Zone 2 and the second on Zones 3-5. Focusing on Zone 2, an individual POI is introduced at the end of the zone (Bus 13). The output of a constant generation source is incremented in 10kW steps until the up-stream regulator reached its maximum buck-tap position. The results shown in Figure 3.7(a & b) present a maximum permissible DG size of 530kW after referencing the voltage and apparent power flow at various DG levels.



(a) Voltage Profile Impacts (b) Apparent Power Impacts
Figure 3.7: Supervised CYME DG Hosting Capacity Results of Zone 2.

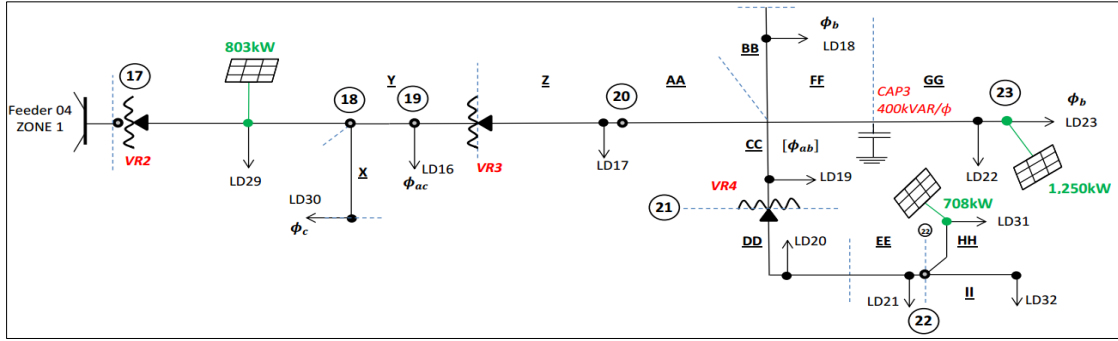


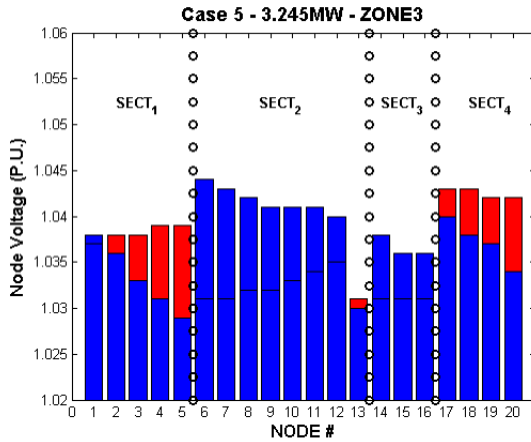
Figure 3.8: Feeder 04 VREG Zones Under Testing

Now considering Zones 3 through 5, Figure 3.8 presents the topology of this section where five different combinations of POIs at maximum permissible real power outputs were tested as summarized in Table 3.2. The capacities of these facilities represent the maximum injection levels before the upstream line regulator was not able to compensate.

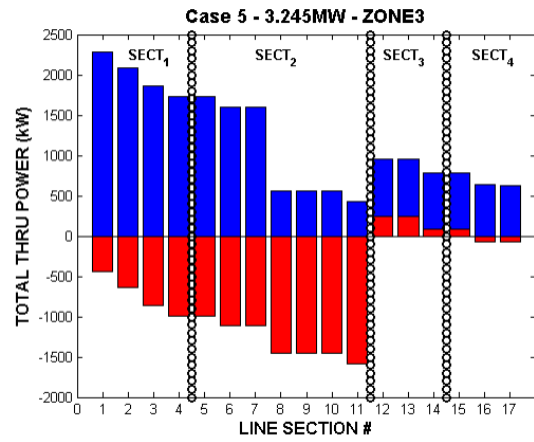
Table 3.2: Summary of POI Locations & Tested Injection Levels

Scenario	%PEN	ZONE3	ZONE4	ZONE5
S1	43.12%	LD29; 803 kW	LD23; 1,215 kW	LD31; 708 kW
S2	33.19%	LD16; 700 kW	LD18; 436 kW	LD32; 840 kW
S3	41.32%	LD16; 700 kW	LD23; 1,250 kW	LD32; 640 kW
S4	29.53%	LD29; 400 kW	LD17; 800 kW	LD20; 500kW
S5	42.97%	-	LD23; 2,015 kW	LD32; 700kW

After comparing the voltage and power flow impacts for all five scenarios, S4 results in the worst voltage profile when DG is placed at the beginning of each VREG zone. Results of S5 as shown in the figures below provide an insight on how a utility-scaled DER-PV can reverse power flow and essentially introduce an inverse voltage drop, lowering the system voltage far worse than previously experienced.



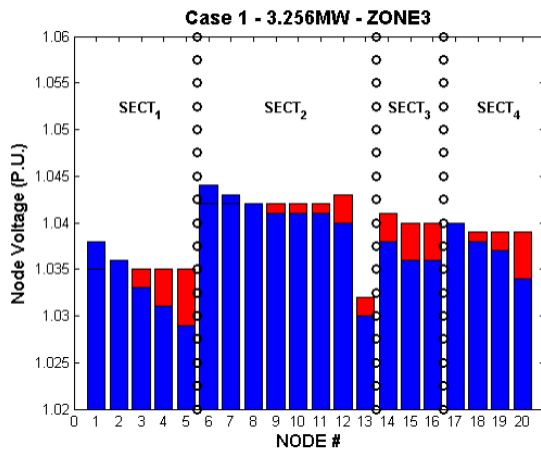
(a) Voltage Profile Impacts



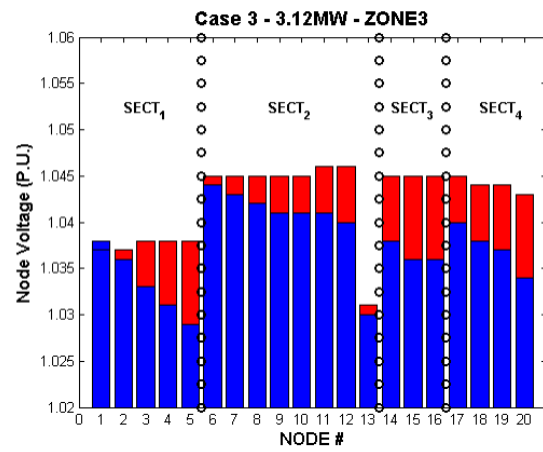
(b) Real Power Impacts

Figure 3.9: Scenario 5 Results of Utility-Scaled DG Connection

Scenarios 1 and 3 (S1 & S3) had very similar power flow results due to the only difference being Zone 3's POI location. The resulting voltage profiles from these scenarios are provided in Figure 3.10 (a & b), depicting the node voltage with and without DG as red and blue respectively. S1 was selected as the most ideal scenario because of a lower voltage rise due to PV generation. This study concluded that location of POIs with respect to VREGs can drastically change the impacts to the feeder voltage profile by consistently moving the VREG taps to their maximum buck positions.



(a) S1 Voltage Impacts



(b) S3 Voltage Impacts

Figure 3.10: Scenario 1 & 3 Comparison

After conducting the DG permissibility study on Feeder 4, it was obvious that CYME required heavy human interaction to set up DER-PV penetration scenarios. Also, since CYME was limited to “snapshot” load flow, the voltage regulation equipment operations were not observed with respect to time. To achieve more robust impact studies and time-series analysis, Open Distribution System Simulation (OpenDSS) was selected for future analysis since it is a tool for electric utility distribution system planning or analysis. It can be implemented as both a stand-alone executable program and as an in-process COM server [20]. With the capability of having a COM interface, OpenDSS can be driven from a variety of existing software platforms including MATLAB. Connecting OpenDSS with MATLAB through a COM interface enables any information within DSS to be extracted and DSS commands to be pushed from MATLAB.

Having this functionality makes it feasible to automate scenario creations, process large quantities of simulation results, initiate Quasi-Static Time series (QSTS) analysis, and model advanced voltage regulation controls. In addition, a toolbox called “Grid Integrated Distributed PV” (GridPV) [21] includes pre-built functions that utilized this COM interface and can extract all possible information on lines, buses, loads, and etc. from DSS to the MATLAB workspace.

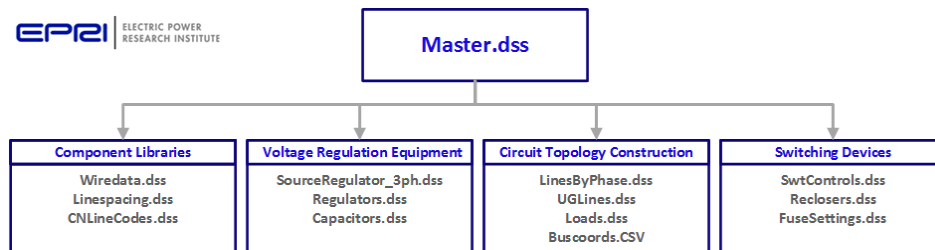


Figure 3.11: OpenDSS Feeder Model Architecture

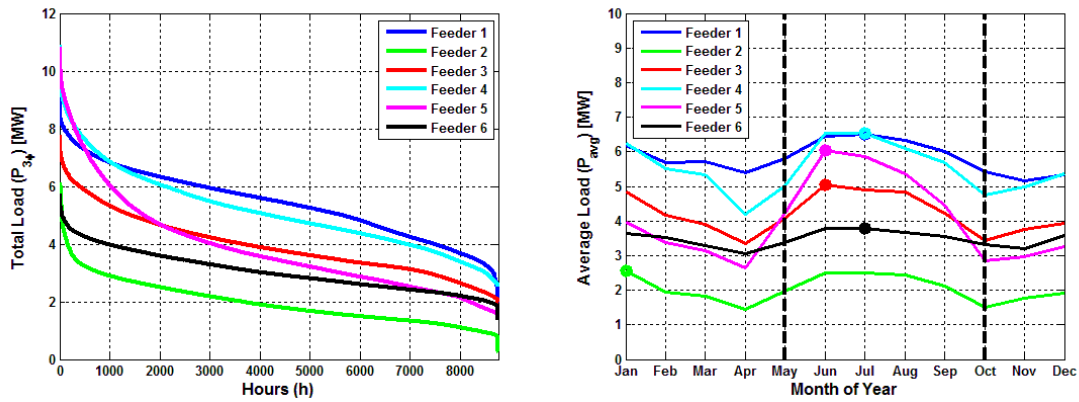
To create OpenDSS models of the six test feeders, the CYME database and circuit connection information were exported and processed using a modified VBA script originally provided from Roger Dugan at EPRI [20]. One feeder model within DSS involves four main code sets: circuit topology construction, component libraries, Voltage Regulation Equipment, and Switching Devices. As illustrated in Figure 3.11, a master file initiated via MATLAB compiles all .dss files. Controls can be associated with Voltage Regulation Equipment and Switching Devices. Also, monitors can be attached to specific buses or nodes which can measure and save various aspects including voltages, currents, all powers, transformer taps, state variables, and Voltage Flicker (PST).

3.3 Load Level Selection for DER-PV Hosting Capacity Analysis

Before automated OpenDSS simulations can be conducted on the six test feeders to test all possible POI location for DER-PV, selection of specific static load levels is required based on the annual distribution of feeder-head power measurements. Fortunately due to Smart Grid initiatives at Duke Energy, the vast majority of distribution substations have data acquisition systems installed interacting directly with supervisory control and data acquisition (SCADA). SCADA systems are responsible in acquiring analog data from transformers and station buses via current and voltage transducers and converting the measurements to various digital formats for transmission and storage [22].

Utilizing two different SCADA historians, feeder-head single phase real and reactive power measurements were extracted spanning the entire year of 2014. Because of a limitation in DEP's SCADA historian, measurements were only available at 15 minutes as opposed to the DEC data extraction interval of 10 minutes. To make the

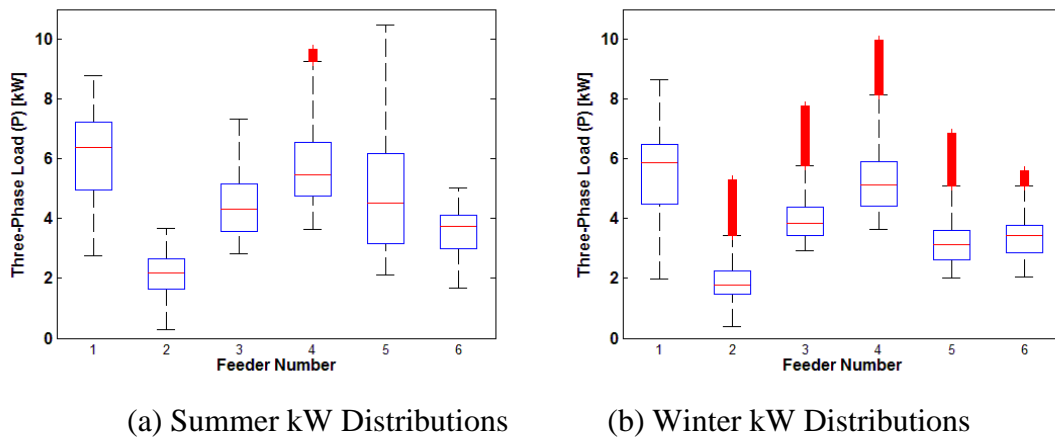
datasets time synchronized, all measurements were interpolated to 1 minute intervals. Then, a data quality algorithm conditioned all six datasets by restructuring, timestamp checking, and linearly estimating the values of any missing data points less than 1 hour spans. Single phase measurements were aggregated to provide insight into each feeder's annual load shape distribution and presented in Figure 3.12(a). Interpreting these load trends, Feeders 01 & 04 operated above 5MW over 60% of the time showing greater potential for a possible utility scale solar PV facility.



(a) Annual Distribution of Feeder Load (b) Monthly Averages between 10AM-4PM
Figure 3.12: Compilation of Historical SCADA Data

It is also important to observe the monthly trends in load, as depicted in Figure 3.12(b). Due to the focus on DER-PV impacts, the monthly averages were based on load between 10AM and 4PM. This is because solar energy will consistently peak during this time interval and be insignificant otherwise. The summer months (shown as in-between the dotted vertical lines) consistently had higher monthly load averages along with yearly peak averages. Feeders 03 through 05 had very drastic seasonal shifts in load typically seen with residential customers, confirming Figure 3.4(b) that these feeders have the highest percentage of residential loads.

In order to make statistical inferences on the load levels at peak solar PV generation, the dataset distributions are required to be approximately normal. A typical means to check this is to observe the quartiles, minimum, maximum, and outliers in a boxplot. Two boxplots of each season are provided in the figures below. The distribution of summer load can be considered approximately normal with slight upper or lower skewness. Winter on the other hand, if excluding the outliers had very symmetrical distributions. After further investigation, these outliers occurred on two days when there were record low temperatures in the South Atlantic region. These days were excluded from future statistical analysis to more accurately represent the population of feeder load.



(a) Summer kW Distributions (b) Winter kW Distributions
Figure 3.13: Seasonal Comparison of 2014 Load between Feeders

After confirming both summer and winter 10AM-4PM collections of load are approximately normal, average load (\bar{P}_S & \bar{P}_W) during each minute interval is calculated along with the variance and standard deviation (s_S & s_W). This procedure was conducted on each feeder with compiled results listed in Table 3.3, providing percentages of annual peak load. To make the results of the DG hosting capacity algorithm conservative,

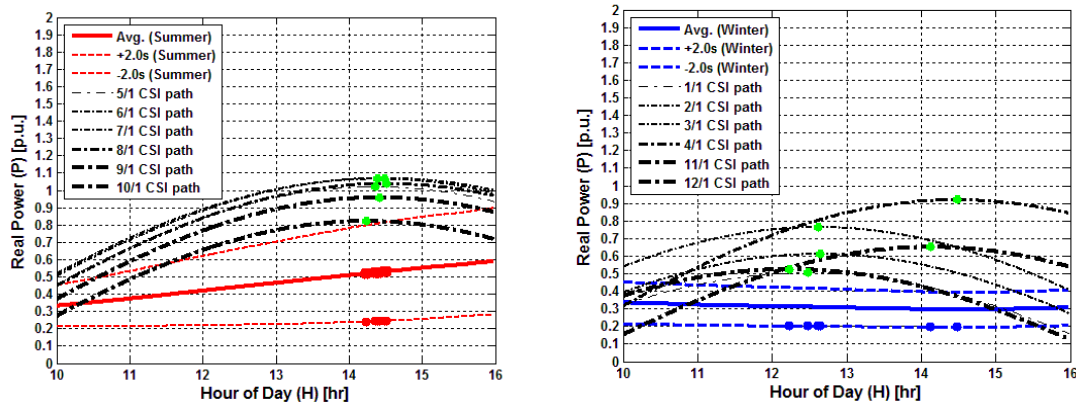
inferences are made on seasonal worst case scenarios of minimum load levels during this peak solar generation interval.

Table 3.3: Summary of Seasonal Load Averages and Standard Deviations

<i>Parameter</i>	Feeder 1	Feeder 2	Feeder 3	Feeder 4	Feeder 5	Feeder 6
Peak	9.53MW	7.93MW	6.36MW	10.95MW	10.94MW	5.75MW
\bar{P}_S	0.70	0.65	0.50	0.62	0.54	0.75
s_S	0.11	0.10	0.10	0.10	0.145	0.095
\bar{P}_W	0.62	0.55	0.40	0.50	0.30	0.70
s_W	0.095	0.025	0.075	0.05	0.05	0.10
$\bar{P}_S - 2 \cdot s_S$	0.48	0.45	0.30	0.42	0.25	0.56
$\bar{P}_W - 2 \cdot s_W$	0.43	0.50	0.25	0.40	0.20	0.50

Utilizing a VBA algorithm developed by NOAA [23], the clear sky irradiance (CSI) profiles at the beginning of each month are obtained, taking into account the rotation of the Earth around the Sun. Figure 3.14 (a) and (b) presents an example of the CSI peaks (shown as green dots) being compared to the coincident feeder load (red or blue dots). Feeder 5 was selected due to its load shape being drastically impacted by season. The CSI paths are also plotted on the same graph after dividing by 1000 W/m² to normalize with P.U. load. The solid colored lines represent the minute averages.

Assuming a normal distribution of one minute load measurements, a 95.45% confidence interval of observed load is presented in-between the colored dotted lines. Two standard deviations away from the average ($\bar{P}_S \pm 2 \cdot s_S$ & $\bar{P}_W \pm 2 \cdot s_W$) form the boundary lines that represent the selected frequency that an event will occur where load is outside this range once every three weeks [24]. Therefore, coincident lower bound loads ($\bar{P}_S - 2 \cdot s_S$ & $\bar{P}_W - 2 \cdot s_W$) at peak CSI are selected to formulate worse-case scenarios in concluding DG hosting capacity.



(a) Summer Peak Solar Time Instances (b) Winter Peak Solar Time Instances
Figure 3.14: Daytime Average and +/- 2 Standard Deviations with Monthly CSI

3.4: Iterative Static Hosting Capacity Analysis

The rise of distributed energy resources, especially solar PV (DER-PV), has prompted utilities to search for alternative methods of performing interconnection studies that are less time consuming and expensive. Use of CYME to perform these studies demands a great deal of human interaction and is unmanageable to test all possible future locations of DER-PV along a distribution feeder. By converting CYME models to OpenDSS files, the circuit model can be altered in an automated fashion through the use of numerical computing environments like MATLAB or PYTHON. One application which exploits this powerful functionality is determining the minimum and maximum hosting capacity of DG along detailed models of distribution feeders.

Hosting capacity is considered to be the maximum amount of generation the feeder can accommodate before impacting system reliability or power quality. This hosting capacity is heavily dependent on location and loading level. It would be extremely beneficial to distribution planners if they can reference a tool which already zoned out of maximum DG capacity when processing interconnection requests. Utilizing

MATLAB, an algorithm is built to identify system constraints with the presence of DG. A flow chart of this process is presented in Figure 3.15 and later applied to all test feeders. The analysis consisted of iterating through all feeder buses (nodes), and testing a location if the Point of Interconnect (POI) criterion was met [25]. Understanding that the majority of installed solar PV capacity in North Carolina is utility-scale, the POI criteria required a three-phase connection at the nominal feeder voltage.

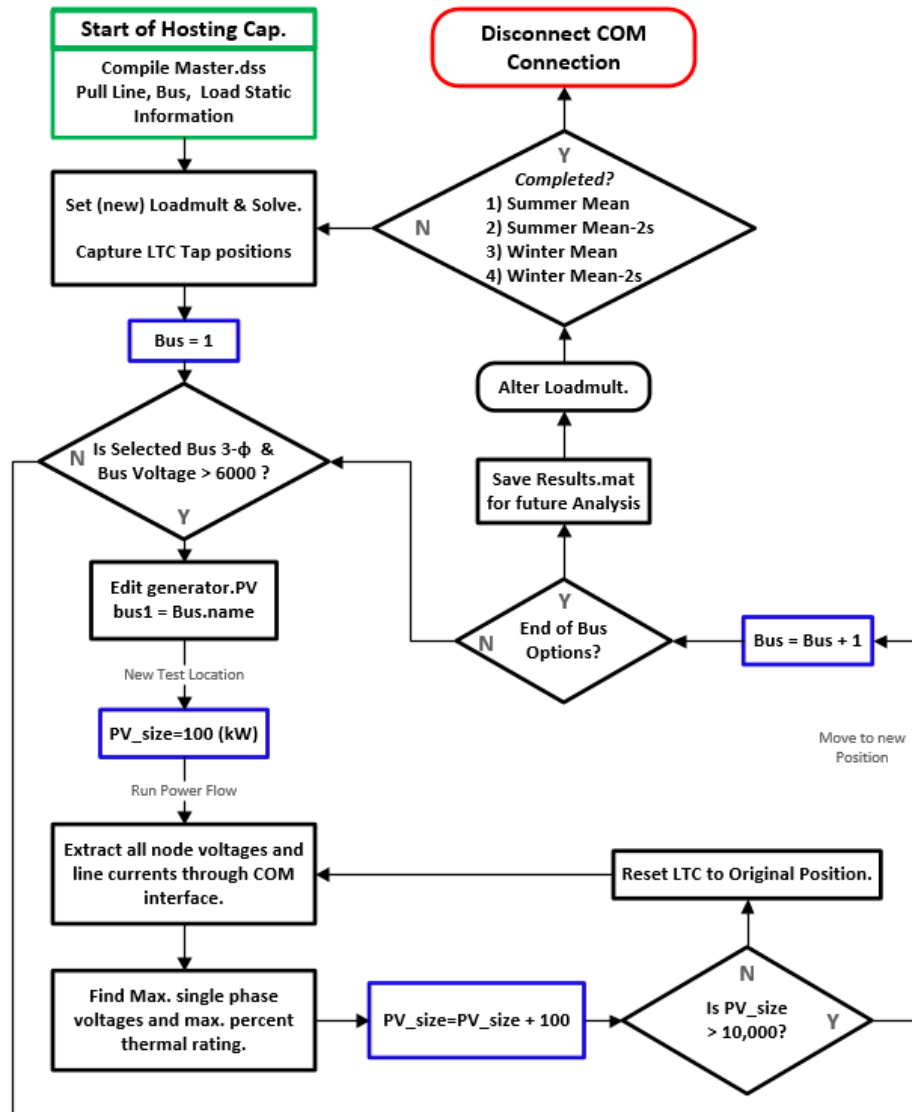


Figure 3.15: Detailed Hosting Capacity Flow Chart

As an example, all locations which fulfilled the POI criteria are shown as light blue circles in Figure 3.16. At each location, a generator is connected and OpenDSS is initiated to run unbalanced power flow 100 times, controlled by a 100kW iteration of generation capacity until reaching 10MW. A worst case scenario was assumed with the generator outputting at 100% of its rating and all switch capacitors energized to introduce a higher voltage profile. At each 100kW interval, the power flow solution was extracted through the COM interface to the MATLAB workspace where the maximum per-unit (p.u.) three-phase voltage and maximum percent line loading was determined and recorded for future analysis. Before testing the next scenario, the LTC tap position was reset to the original position along with any VREGs if present.

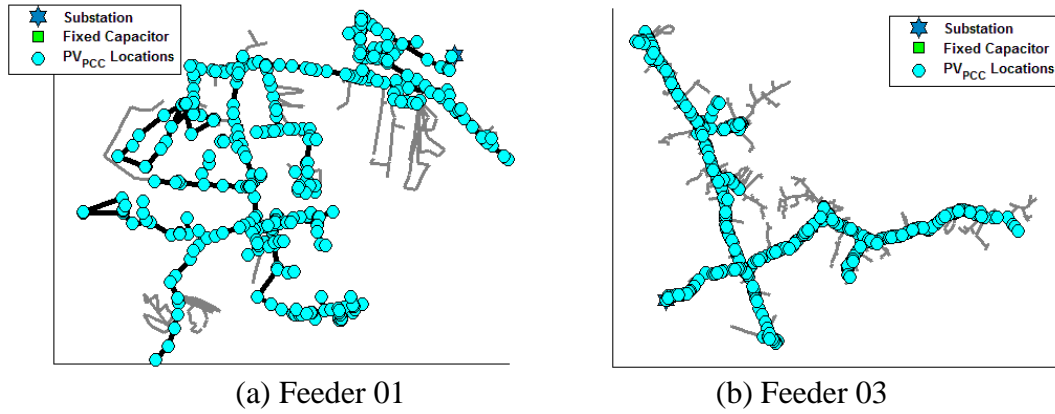


Figure 3.16: Permissible POI Locations

Referencing Table 3.3, four feeder load levels were selected which captured the seasonal average loading conditions and two standard deviations away from the mean during the peak solar time interval. Selected these specific load levels enclosed the vast majority of worst case scenerios when load levels could possibly be low while solar generation is high. Therefore, this forced concluded locational hosting capacity to be

more conservative in nature. Individual customer load information can be captured from Advanced Metering Infrastructure (AMI) which provides hourly demand measurements for every meter fed from a distribution transformer (DT). Unfortunately, these feeders do not have AMI implemented. Therefore, feeder load allocation was based on the DT capacities or commonly known as connected kVA. Load allocation based on connected kVA is not very accurate because it assumes an even distribution of load between customers. Also, it is not uncommon for a utility to use only a few sizes of DTs. By using connected kVA, customer load can be overestimated [26].

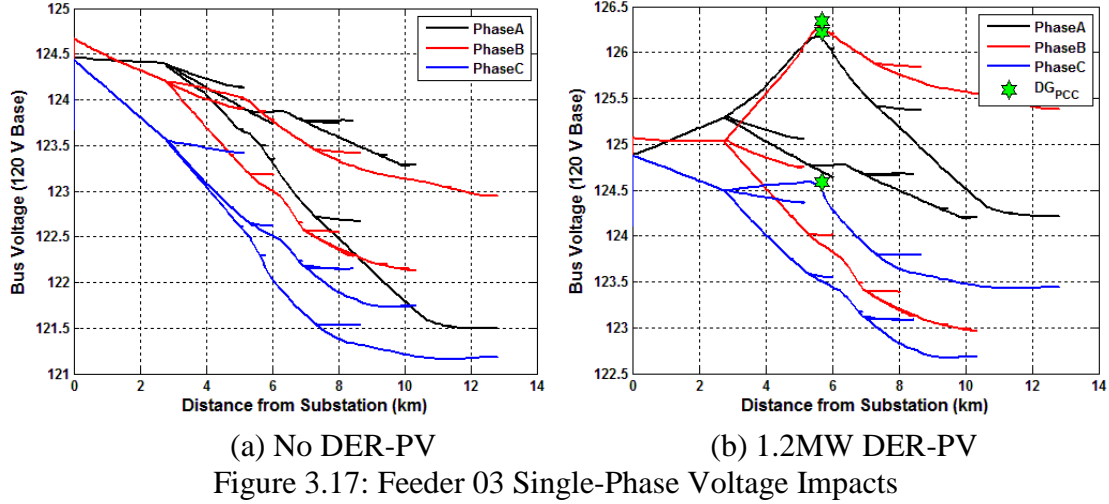
In total, the hosting capacity analysis of six feeders consisted of almost 700,000 scenarios taking approximately 103 hours to complete. Individual feeder simulation performance details are located in Table 3.4. Note that even though some feeders have less test buses, the simulation time is greater due to the size of the circuit line dataset being transferred over the COM interface. This data extraction was necessary each iteration to capture line current and power flow results and was the limiting factor.

Table 3.4: Summary of Hosting Capacity Algorithm Performance

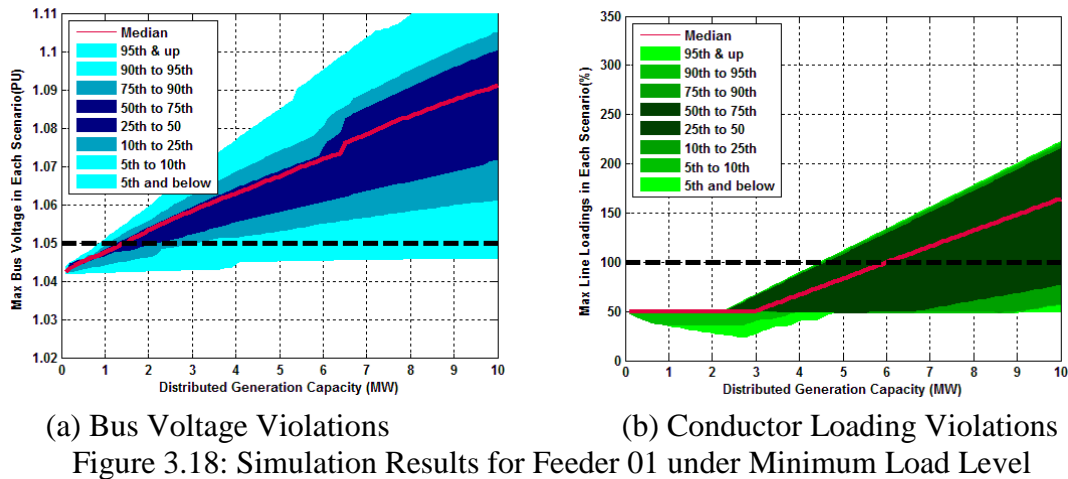
Feeder #:	1	2	3	4	5	6
Number of buses tested	389	208	344	428	261	113
Total number of scenarios	155,600	83,200	137,600	171,200	104,400	45,200
Total Sim. Time (hrs)	13.7	12.7	19.2	30.2	26.7	0.83

To illustrate how a utility-scale DER-PV facility can increase the feeder voltage above the ANSI C84.1 standard, a 1.2MW DER-PV was placed 5.7km away from the substation on Feeder 03 under its mean summer load. The three-phase voltage profile before and after the interconnection is portrayed in Figure 3.17. Because the maximum

voltage observed was 126.25V or 1.052 p.u., this 1.2MW facility will introduce new voltage violations if connected.



To understand the vast detail of the captured results, Figure 3.18 provides an example on the spread of maximum p.u. voltages and percent line loadings by illustrating the median and key percentiles. The interquartile range is depicted as the dark blue and dark green regions, representing 50% of the population. Selecting the results of Feeder 01 at average summer load, voltage violations did not occur until DER-PV capacity was 2.3MW while maximum line current did not surpass amperage ratings until 4.5MW.

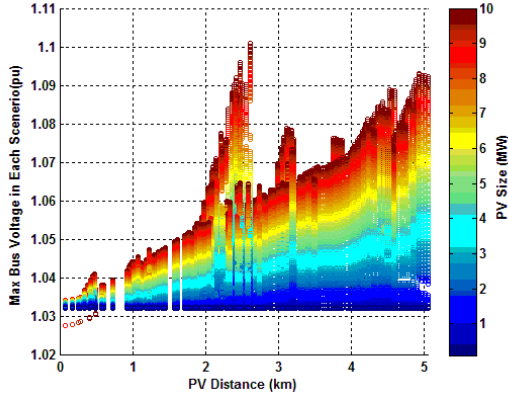


Assume a customer requests an interconnection for a 4.0MW PV facility. Referencing the median of the max voltage, 50% of possible locations on Feeder 01 will result in voltage over the ANSI standard while none of the possible locations will result in a conductor surpassing its thermal ampacity limit.

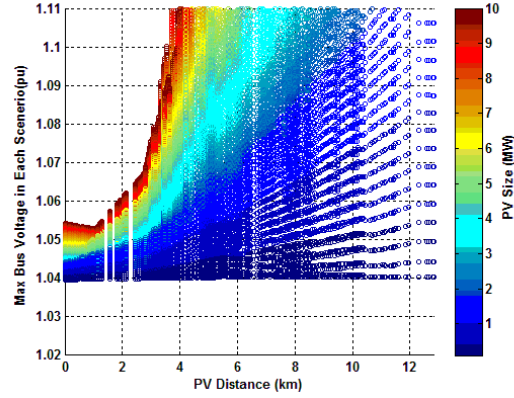
3.5: Distribution System Characteristics Impact to DER-PV H.C.

How a generator impacts the voltage profile or power flow direction is greatly dependent on the physical layout of the feeder. This includes the length of the backbone and connected load density. Due to the fact that a utility-scale solar farm requires an average of 7.6 acres of total land to install 1MW of PV arrays [27], utilities are receiving interconnect requests located on long, rural distribution feeders. These locations are ideal for the PV farm developer but not for the utility. This is because the voltage sensitivity is extremely high on the distribution feeders that support these geographic areas due to light load densities and long conductor spans.

To verify that voltage sensitivity is a function of feeder length, the maximum captured bus voltage per DER-PV location to the corresponding capacity [25] is presented in Figures 3.19 (a) and (b). Feeders 02 and 03 were selected to show a contrast in total end distance, with Feeder 02 being half the length of the 8 mile long Feeder 03. From inspection, the range of observed maximum bus voltages increases as the POI becomes further away from the substation. Feeder 03 experienced voltages above 1.05 even right next to the substation while it took until a 5MW DER-PV to be almost 4 km (2.5 miles) away from the substation before voltage violations were observed.



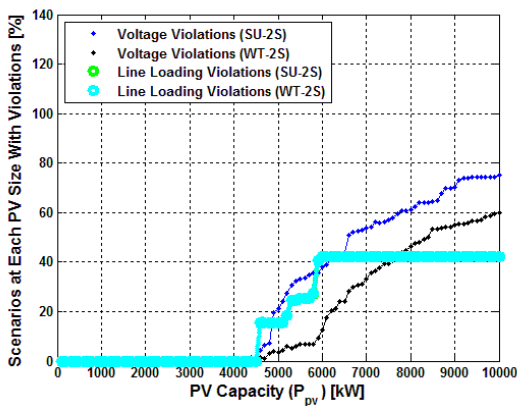
(a) Feeder 02



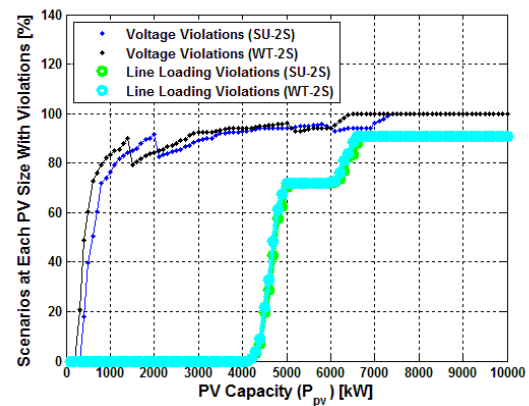
(b) Feeder 03

Figure 3.19: Captured Max Bus Voltage at Each Iteration

The percentage of test locations in which either an ANSI C84.1 or conductor ampacity violation occurred was found for a more simplified approach. Again, the results from Feeders 02 or 03 under minimum seasonal loading conditions are provided in Figures 3.20 (a) and (b) respectively. Supporting the inferences made from Figure 3.19, the percent of the voltage violations shot up at 0.4MW on Feeder 03 while not occurring until 4.6MW on Feeder 02. Such a drastic difference between feeders with the same LTC settings proves that feeder length and load density greatly impact voltage sensitivity.



(a) Feeder 02



(b) Feeder 03

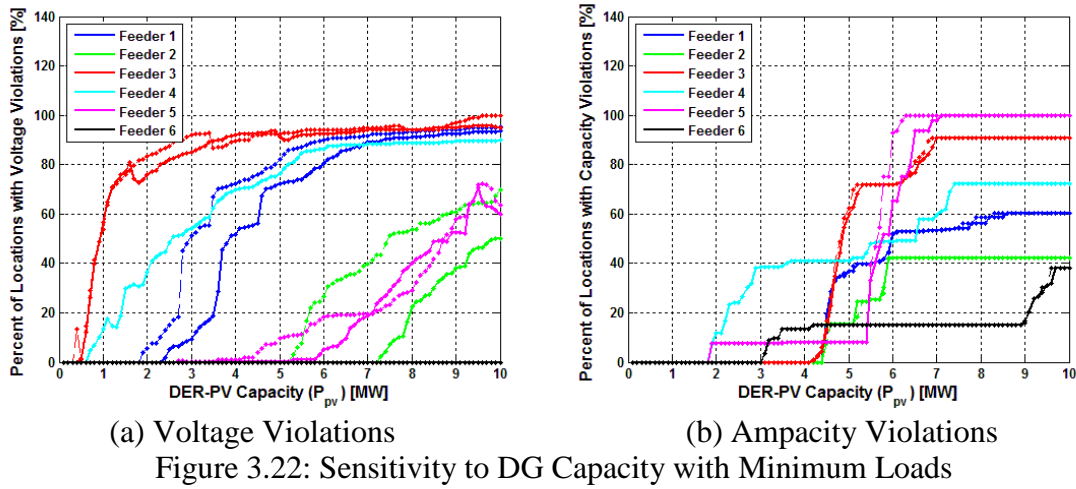
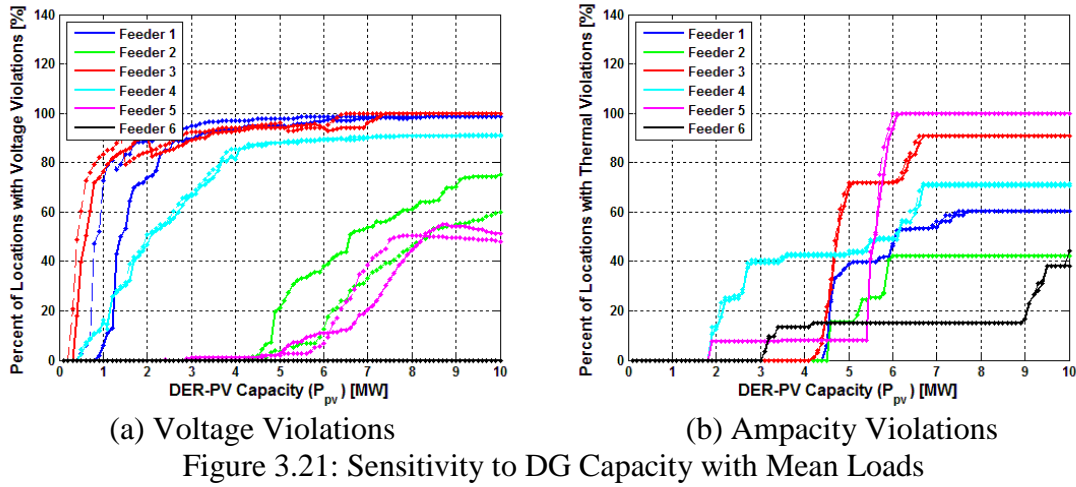
Figure 3.20: Percent of Locations with Violations

On both feeders, notice how normal conductor ampacity violations started to occur at 4.5MW. This was not surprising because both operate at a nominal 12.47kV with almost 60% in total reach of total three-phase lines having continuous ampacities of less than 300A. Because distribution systems generally have only a select number of cable sizes, sudden jumps in line violations occur [25]. Distribution feeders with a larger proportion of installed conductor with higher ampacity will experience line violations at a higher installed DER-PV capacity.

In order to make inferences of possible independent variables which contribute to limitations on minimum DG hosting capacity, the percent of locations introducing either violation are compiled and presented in Figure 3.21 and 3.22. Comparing voltage violations, Feeder 03 was the most sensitive while Feeder 05 was the least. Regarding the feeder characteristics, Feeder 03 operates at 12.47kV and has an end distance of ~8 miles. On the other hand, Feeder 5 operates at 22.9kV and a much shorter end distance of ~5 miles. Confirmed with Figure 3.19, interconnections toward the end of the feeder exhibit a wider range of maximum voltages. Therefore, the feeder's length is responsible for the strength of response to facility size [25].

The types of conductor installed on these feeders will later be proven correlated to the voltage and line loading sensitivity. After observing when line loading violations start to occur, Feeder 02 does not experience loading violations until introducing a 4.5MW DER-PV facility and then jumping to over 70% of locations observing a violation. Feeder 05 begins to experience violations at 1.8MW with 8% of locations and does not observe ampacity violations until installing a 5.4MW facility. When comparing the types of

conductors installed on these two feeders, 02 has 58% of total conductor reach with under 400A ratings, suggesting why there is a sudden jump at 4.5MW. Feeder 05 on the other hand only has 11.6% of conductor reach under 400A with the vast majority (60%) having ampacity ratings over 600A. Due to this fact, the step increase in percentage of line loading violations on Feeder 05 occurred 1MW after Feeder 02.



The detailed hosting capacity analysis was performed at load levels two standard deviations away from the seasonal means during the peak solar interval. The compiled violation results are presented in Figure 3.22, showing overall trajectories on the percent

of locations for both voltage and line loading violations were not significantly impacted as expected. The voltage violations only noticeably shifted past a DER-PV capacity of 5MW. Feeder 01 was unique from the group because it resulted in the largest increase of voltage violations during light loading conditions. Figures 23 (a) & (b) provide a closer look at this feeder's seasonal impact to voltage and line loading violations. With the average summer load at 70% of peak load and the two standard deviations away from the average load level of 48% suggests this feeder has a large spread in annual system load. The load level drastically effects the voltage profile of a feeder because with low loading conditions, the voltage profile is abnormally high. On the other hand, line loading violations did not deviate away from the average loading condition results due to the fact that there is less line current during light loading. Therefore, it can be concluded that showing the seasonal dependence on DER-PV hosting capacity is important to capture nature of variable local load and its impact on voltage violations.

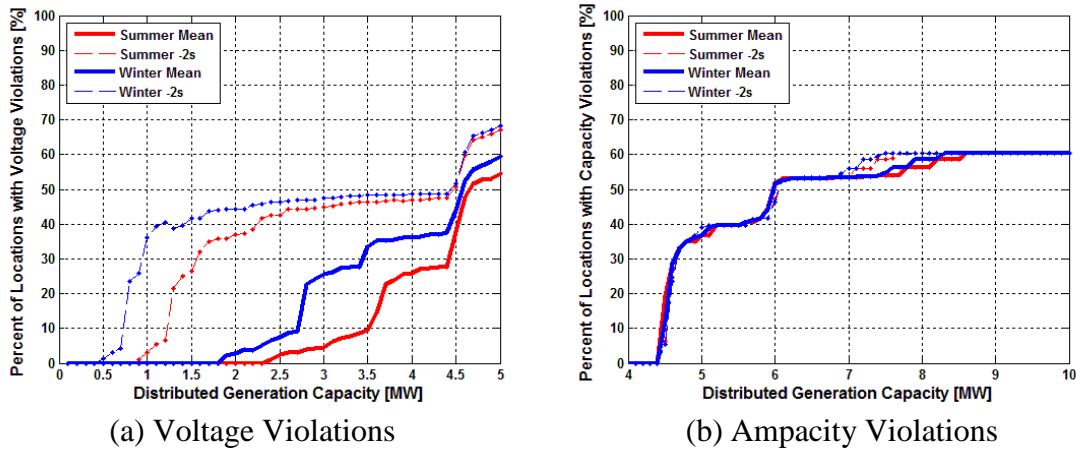


Figure 3.23: Seasonal Shift in the DG Hosting Capacity on Feeder 01

Now that the injection level at which voltage and ampacity violations occur have been identified at all permissible POI locations along each of the six feeders, the

minimum hosting capacity (MHC) per location before a violation would continuously be observed were compiled. On top of MHC, key distribution system design characteristics associated with each location included distance from substation, short circuit resistance (R_{SC}) and reactance (X_{SC}) to the substation, ampacity of immediate upstream conductor (C_r), and total feeder load ($P_{3\phi}$). The resulting locational MHCs at each loading condition on Feeder 02 and 03 are presented in Figures 3.24 (a) & (b) respectively. Previously, it was observed that Feeder 03 had severe voltage sensitivity. The MHC reflected this by drastically decaying as upstream short-circuit impedance increased. Feeder 02 is relatively short with the maximum POI upstream impedance of 2.9Ω , 27% the magnitude of Feeder 03's maximum Z_{SC} . Therefore, Feeder 02 resulted in drastically higher hosting capacities but with more dependability on the loading condition.

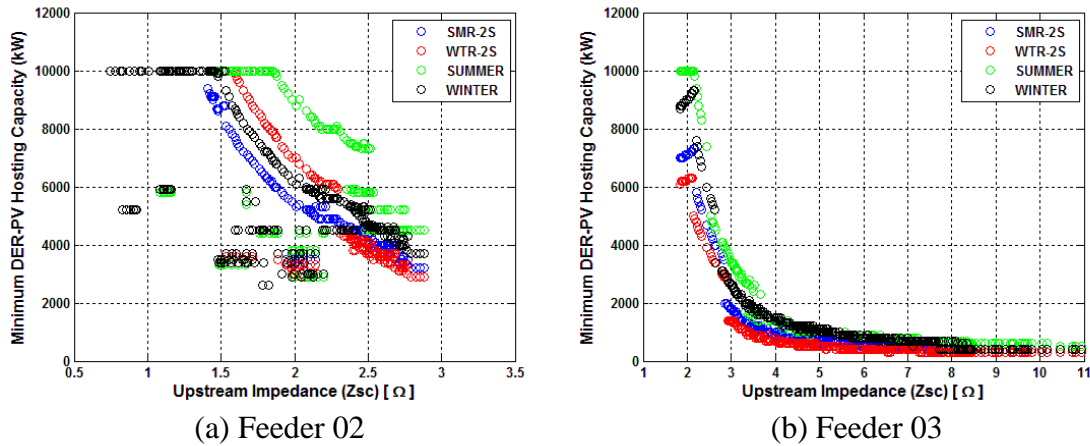


Figure 3.24: The Minimum DER-PV Capacity Dependency on Distance from Sub.

To investigate what key locational aspects impact DG hosting capacity, a linear model was built by setting local distribution network characteristics as the independent variables and MHC as the dependent variable. Because distance from substation and upstream impedance are directly correlated to one another, these two independent

variables would introduce multicollinearity if both were included in the statistical prediction model. The linear model prediction will be negatively impacted if multicollinearity between independent variables exist [24]. Therefore, distance from substation was excluded from the proposed second order linear regression model presented as Eq. (3.3). The first variable (X_1) was set to the inverse of the POI's upstream impedance while the second variable (X_2) was the square of this.

$$MHC = \hat{\beta}_0 + \hat{\beta}_1 \cdot x_1 + \hat{\beta}_2 \cdot x_2 + \hat{\beta}_3 \cdot x_3 + \hat{\beta}_4 \cdot x_1 x_3 + \hat{\beta}_5 \cdot x_2 x_3 + \hat{\beta}_6 \cdot x_4 + \hat{\beta}_7 \cdot x_1 x_4 + \hat{\beta}_8 \cdot x_2 x_4 \quad (3.3)$$

$$\text{Where} \quad X_1 = \frac{1}{\sqrt{R_{SC(1)}^2 + X_{SC(1)}^2}} = \frac{1}{Z_{SC(1)}} \quad X_2 = X_1^2 \quad X_3 = P_{3\phi} \quad X_4 = C_r$$

Interaction terms were constructed by multiplying these inverse impedance variables to either total feeder load or the immediate upstream conductor's ampacity. MHC and associated POI variables of Feeder 01 & 03 at two different load levels were imported into the statistical software package R where Eq. (3.3) was constructed. A least squares regression analysis was initiated and the model coefficients resulting in the minimum sum of squared errors were concluded and provided in Table 3.5. The p-values originated from t-tests performed on each individual independent variable. This was done to confirm if each term was significantly correlated to MHC. Enforcing a standard level of significance of 0.05, only $\hat{\beta}_8$ in Feeder 01 violated this threshold. Additional metrics of the overall prediction model's performance were provided in Table 3.5 including standard error (SE) and the coefficient of determination (R^2). The two MHC prediction models applied to Feeders 01 and 02 resulted in R^2 values greater than 0.9 with reasonable standard errors. Therefore, these models were able to sufficiently predict the

minimum hosting capacity at each available interconnection point solely on static independent variables that can be obtained without a power flow solution.

Table 3.5: Results of Least Squares Regression

Coefficients:	Feeder 01 Results	Feeder 01 P-Values	Feeder 03 Results	Feeder 03 P-Values
$\hat{\beta}_0$	5,916	2e-16	3,064	<2e-16
$\hat{\beta}_1$	-35,513	2e-16	-20,829	1.4e-14
$\hat{\beta}_2$	24,534	2e-16	27,258	5.06e-7
$\hat{\beta}_3$	-0.9266	2e-16	0.2184	0.005
$\hat{\beta}_4$	7.344	2e-16	-1.816	0.003
$\hat{\beta}_5$	-4.81	2e-16	12.465	<2e-16
$\hat{\beta}_6$	1.253	0.0018	-11.917	<2e-16
$\hat{\beta}_7$	-11.472	0.0199	73.499	<2e-16
$\hat{\beta}_8$	22.126	0.8833	-82.396	8.1e-14
R2	0.929	-	0.976	-
SE	606.1	kW	287.8	kW

To illustrate the prediction model results, the two remaining load levels not used when constructing the model were inputted into $P_{3\phi}$. Figure 3.25 provides the estimate line with the MHCs determined by the hosting capacity algorithm for both Feeders 01 and 02. From inspection, the proposed second order model was able to sufficient predict MHC.

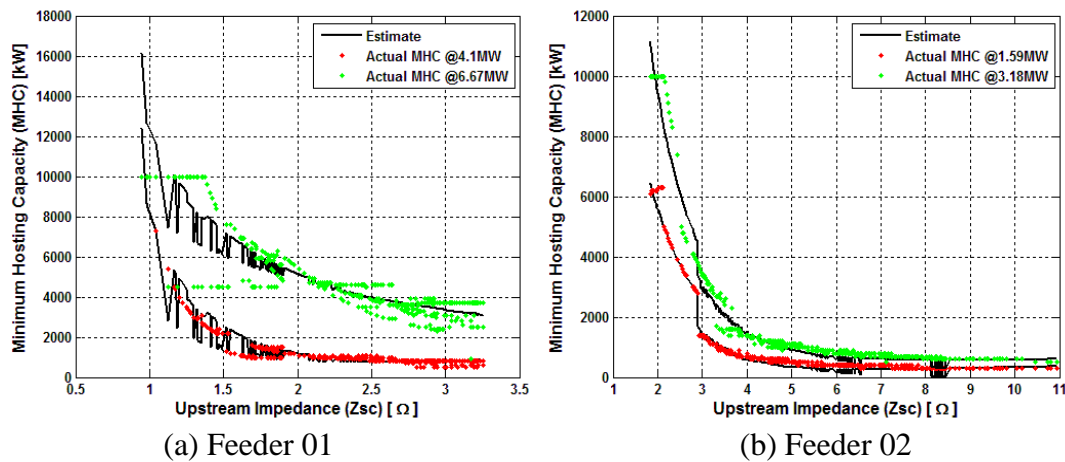


Figure 3.25: Second Order Model Prediction Results

To demonstrate the dependence on individual POI's DER-PV hosting capacities to location, Figure 2.26 provides the topology of Feeders 02 & 03 with a symbol at each test location representing the size of concluded capacity. Observe how Feeder 02 has red symbols at all locations along its backbone while Feeder 03 has blue symbols representing capacity sizes less than 3MW. What is interesting is that there are key locations along Feeder 03 that very large DER-PV facilities with capacity greater than 6MW can be connected even though close proximately POI locations have maximum capacities less than 3MW. Investigating further in why this occurred, these locations had comparatively low short-circuit impedances and at low enough points in the feeder's voltage profile to not cause a high voltage violation.

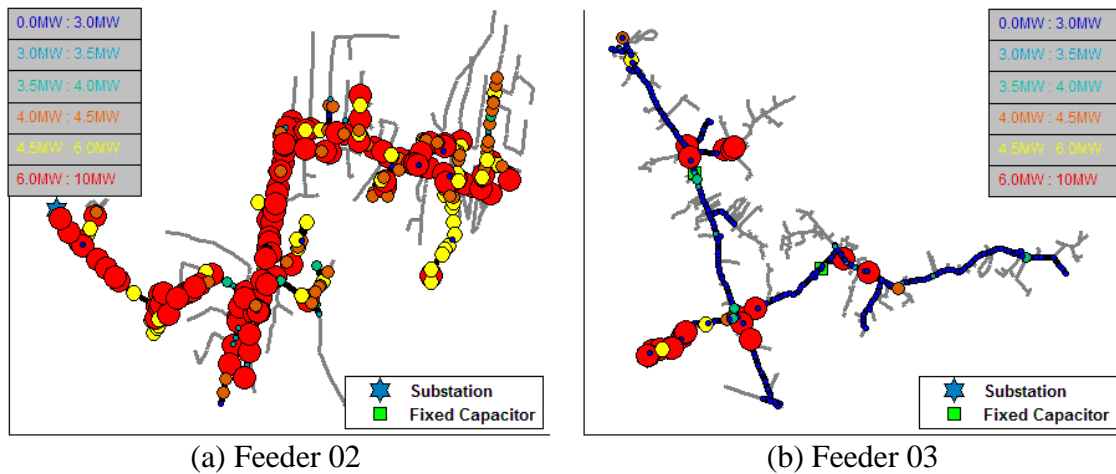


Figure 3.26: Maximum Allowed DER-PV Size under Average Summer Load

In conclusion, four key DER-PV minimum hosting capacity levels were analyzed on each of the six feeders under investigation. A bar chart, provided as Figure 3.27, was constructed for distribution planners to easily tell if an interconnection request will require further detailed investigation. The first level is when both voltage violations (VV) and line loading violations (LLV) will not occur no matter where the facility is placed on

the circuit. The second level provides the range in capacity VV will not occur depending on the seasonal load as shown in light green. This region sheds light into the magnitude of variability in daytime load. Next, the third level provides when VV will occur at a select number of locations as shown in yellow. This region signals the distribution planner that further investigation needs to take place to verify if the interconnection location is in a spot that will not cause high voltage on the distribution network. The last region is unique because it identifies when at least 30% of possible three-phase locations will result in a line loading violation. This is especially important due to the destructive nature of when electrical components fail from overloading and heat stress. On top of this new risk, voltage violations can still occur with continued dependency on location.

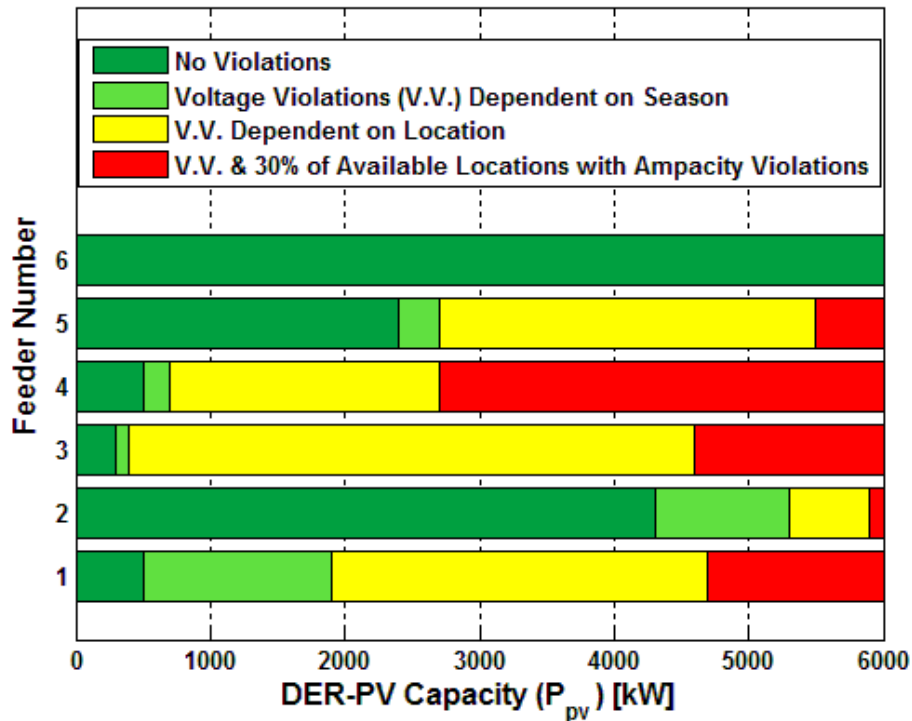


Figure 3.27: Compilation of Critical Levels of DER-PV Hosting Capacity

Overall, Feeder 06 could support the largest capacity of DER-PV while Feeder 03 could support the least without any risk of violations. Feeder 06 is located in a heavily urbanized area so unfortunately the probability of the DNO receiving an interconnection request is extremely low. Feeders 02 and 05 both support areas that are less urbanized and fortunately have large hosting capacities ($>2\text{MW}$) guaranteed to not introduce any voltage violations. Both distribution feeders can support the North Carolina's fast-track DER-PV nameplate capacity of 5MW only after verification that the interconnection location will not cause any high voltage violations during light loading conditions.

Utilizing the COM interface of OpenDSS to conduct iterative actions on distribution feeder models made it possible to test all possible locations and capacity sizes of future DER-PV facilities. As presented, the detailed hosting capacity algorithm is very computational intensive but provides a very clear picture on how an individual distribution feeder can support distributed generation. After compilation of results, it is evident that the distance from the substation along with the seasonal variability of system load has a drastic impact on allowable DER size. This analysis was limited to only static power flow results taken at worst-case scenarios with extreme levels of generation and load. The maximum DER capacity sizes were concluded not taking into account the highly variable nature of solar energy and its impact to operations on voltage regulation equipment like substation load tap changers or distribution capacitors. Therefore, further investigation is required to test if these maximum DER-PV capacities will not degrade regulation equipment when attempting to correct highly variable voltage flicker.

CHAPTER FOUR

CAPTURING DER-PV IMPACTS TO VOLTAGE REGULATION MECHANISMS

4.1: Distribution System Volt/VAR Control Schemes

The major challenge in the integration of high penetrations of photovoltaic (PV) generation to distribution systems is the inherent variability of solar energy. Severe variability in the generation of substantial DER-PV facilities can lead to extreme voltage changes and deterioration of power quality [28]. One major concern that cannot be captured with commercially available static power flow software like CYME is the increase in voltage regulation device (VRD) operations. This in turn will decrease the effectiveness of traditional control strategies and settings [29] and cause concern to Distribution Network Operators (DNOs). The DNOs depend on the VRDs to maintain customer service voltage within ANSI standards and the novel highly variable power injection can force the devices to operate excessively. Automatic voltage regulation can be provided by bus regulation at the substation with on-load tap changers (OLTCs), individual feeder regulation at the substation with step voltage regulators (SVRs), and supplementary regulation along the backbone by smaller SVRs mounted on poles [16]. Shunt capacitors are also installed within the substation or at optimum locations along the feeder backbone to help with reactive power compensation and maintain an economic power factor (PF) to reduce losses.

Typically, voltage regulators are autotransformers which have a winding on a core with a tap off the winding to provide voltage boost or buck capability. This can conceptually be thought of as a transformer with one winding in series with another [15].

Autotransformers are used because they are more cost effective compared to standard power transformers from their ability to let the majority of the current pass through the lower-voltage series winding (I_2). Therefore, only a small proportion of current flows through the shunt winding as shown below in Figure 4.1.

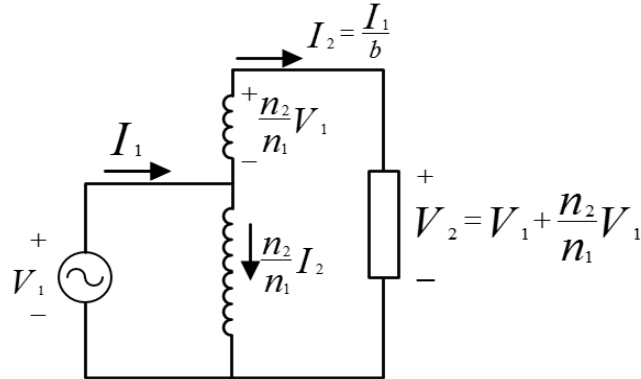


Figure 4.1: Autotransformer Equivalent Circuit

This design inherently transfers much of the power through a direct wire connection and not through a core. Therefore, the required rating (S) of an autotransformer is dependent on the desired voltage change in per-unit (b) between the primary and secondary. The autotransformer rating is established as a percentage of peak load using Eq. (4.1) [16]. As an example, the typical maximum voltage change of 10% ($b=1.1$) on most SVRs will require a rating of 9% of peak load kVA while standard transformers are rated to support full peak load [16].

$$S = \frac{b-1}{b} \text{ where } b = \frac{n_1+n_2}{n_1} \quad (4.1)$$

Active monitoring and reaction to varying load is required for voltage regulators to maintain an acceptable voltage throughout an entire feeder [30]. A change in the turns-ratio of an autotransformer is accomplished from a tap position altering which will in turn

directly impact the entire feeder voltage profile. In order for the initiation and actuation of a tap change to occur, control and tap-changing mechanisms are incorporated into the autotransformer design. The control mechanism is a voltage regulating relay (VRR), which accepts local signals of bus voltage measurements obtained through the use of a Potential Transformer (PT). A PT steps the voltage down from a medium voltage level to a manageable level, typically a nominal 120V. For instance, 12.47kV and 22.9kV service voltage levels have PT turns ratios of 60 and 110 respectively to drop the line-to-neutral voltage to a 120V base. The VRR determines a tap change from three basic settings: the set voltage (V_{SET}), bandwidth (BW), and time delay (TD). The set voltage is the desired voltage of the SVR and is the BW center. When the difference between the monitored voltage and V_{SET} surpasses one-half of the BW, the VRR will initiate a timer (SVR_TMR) to either move the tap position up or down (boost or buck) in-order to change the secondary voltage to be within the BW. The TD, which is the waiting time between when a violation occurs and when the tap change actuates, is typically between 10 to 120 seconds and can be tuned to reduce the number of tap changes.

When a tap change is initiated, a holding switch energizes a permanent magnet motor through an auxiliary low voltage circuit. The motor shaft is coupled to a drive gear which rotates the main autotransformer contact assembly. Because the moving contacts are assembled directly to the main autotransformer's contact assembly, the tap change can occur under load [31]. Three-phase autotransformers operate a tap change in unison; therefore each phase voltage is altered. Typically, the measured voltage originates from a PT connected to the heaviest loaded phase.

In OpenDSS, a SVR is modeled as a three-phase transformer with a PT connected to only one of the secondary side phase windings. These transformers were set to have a minimum and maximum tap position of 0.9 and 1.1 respectively. This enforces the typically ability of SVRs to change the voltage $\pm 10\%$. Because the DNO uses SVRs with 33 tap positions, the autotransformer has the ability to move ± 16 steps as well as a neutral position. Therefore the tap size ($|\Delta n_i|$) is 0.00625, or $(20\%)/32$.

In addition to SVRs deployed for automatic voltage control, distribution system planners install two kinds of shunt capacitor banks: fixed and automatic switch capacitors (SC). Fixed capacitor banks are sized to cover light loading conditions' reactive power and are continuously energized. SCs or commonly referred to as distribution capacitors, are sized and installed to cover heavy loading conditions. They also have the ability to trip offline during light loading periods in order to avoid an excess leading PF. The decision criteria to energize or de-energize can be based off of measured bus voltage, time, time-biased voltage, VAR levels, PF, and other aspects as mentioned in [18].

In order to accurately capture the effect of introducing intermittent DER-PV generation to the operational aspects of distribution systems, the Quasi-Static Time Series (QSTS) function of OpenDSS was utilized. QSTS simulation produces sequential steady state power flow solutions by referencing the converged state of the previous iteration as the beginning state of the next [30]. This enables a proper assessment of time dependency issues that would not be captured when solely using snapshot power flow software like CYME. The main advantage of QSTS simulation is that now daily changes in load and DER-PV generation can be captured along with the associated variance in node voltages

and VRD operational states. Post analysis of the results can enable the conclusion of the magnitude and frequency of operational impacts to equipment [29].

The severity of operational impacts can only be observed through lengthy time series simulations, making this process require a vast amount of input data to construct real and reactive power daily load shapes. Fortunately, the DNO provided CAPER with historical load measurements of each test feeder as discussed in Chapter 3, Section 3. Data quality algorithms were built to linearize missing data gaps and restructure the raw data into one-minute intervals. The peak annual load was found per phase and used to normalize the single phase peak KW and KVAR settings of individual spot loads.

Simulation architecture was constructed in MATLAB to select the daily historical load and create single phase load shapes with P_{MULT} and Q_{MULT} vectors. These controlled the consumption of all single phase spot loads with respect to time. Figure 4.2 presents this simulation architecture simply compiling the desired OpenDSS circuit and incremented the simulation number at a one second interval after calling custom VRD controls. A 1-second step size was selected so that the time delay counters used in the custom MATLAB VRD controls were guaranteed to work properly.

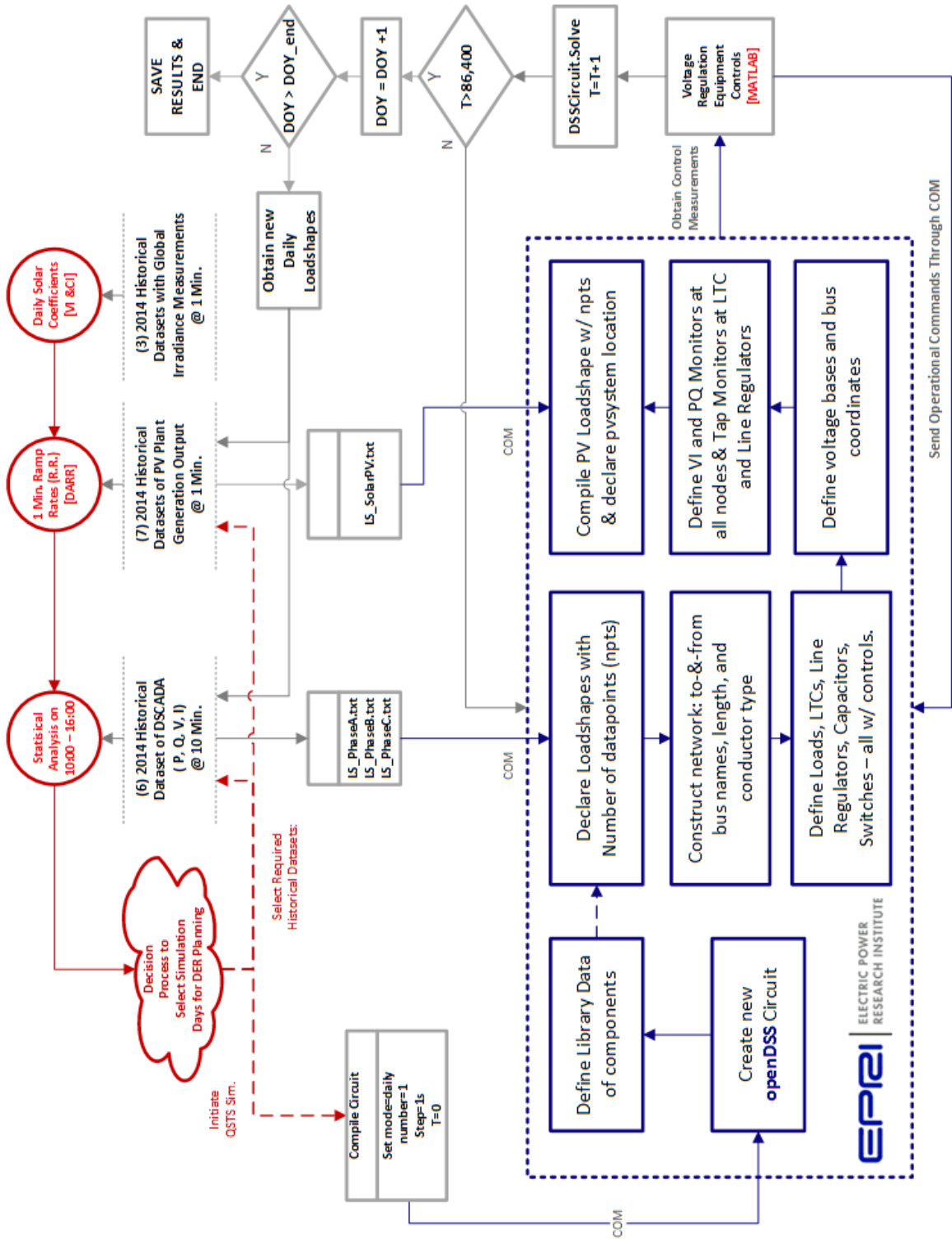


Figure 4.2: Annual Simulation Algorithm Flowchart

To verify this simulation architecture, Feeder 03 was selected due to a 600kVAR fixed capacitor bank and a 450kVAR distribution capacitor connected downstream. Because capacitors are installed on this feeder, the actual reactive power being consumed by the connected load needs to be derived from head of feeder measurements. This is accomplished by accounting the contribution from the fixed capacitor and when energized - the switched capacitor (SC). In order to estimate the state of Feeder 03's SC, an automated process was built to interpret the change in Q (ΔQ) on a per minute basis and flag a change of state if the ΔQ surpassed a certain threshold. This threshold was decided to be 45% of 450kVAR to guarantee that all operations were identified. An example of this process is provided below with Figure 4.3 showing the calculated ΔP and ΔQ and Figure 4.4 showing the previous DSCADA measurements, the derived reactive power to be used in QSTS analysis, and the single phase reactive power of the switched capacitor. The ΔP was included because more advanced logic was incorporated to exclude any temporary outages when there was a drop in both P and Q.

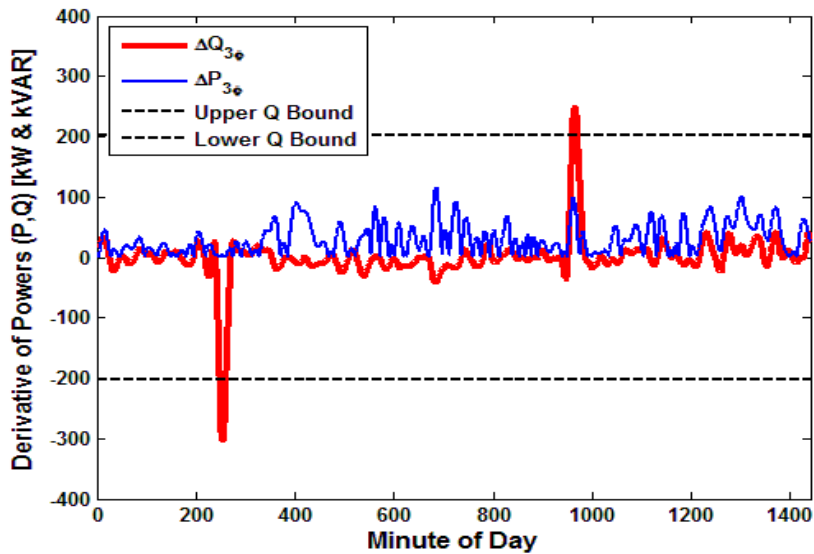


Figure 4.3: One Minute Real and Reactive Power Derivative

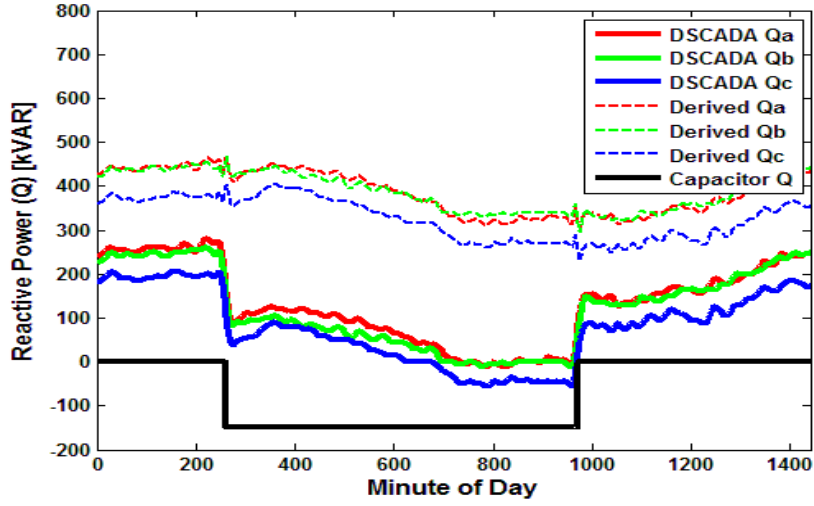


Figure 4.4: Reactive Power of DSCADA, Switch Capacitor, and Derived

After this process analyzed the 2014 dataset, the annual distribution of the derived 450kVAR SC's state of operation was constructed and presented in Figure 4.5. With a 0 and 1 signifying the SC being open and closed respectively, it was observed that the capacitor bank was utilized mainly during the summer months when there was a higher reactive load due to residential air-condition units in operation. To verify this derived reactive power dataset, an annual QSTS simulation was conducted utilizing the architecture presented in Figure 4.2. In order for the switched capacitor to follow the derived state, MATLAB was used to control the state of the capacitor exploiting the COM interface to push commands.

$$e_{p-1\phi} = \frac{\sum_{t=1}^{1440} |P_{1\phi,DSCADA} - P_{1\phi,DSS}|}{1440} \quad (4.2)$$

To quantify the accuracy of this method, the P and Q single phase daily average errors were calculated using Eq. (4.2) and presented in Figure 4.6. From inspection, the

errors were reasonable and it was concluded that this discussed process to construct the reactive power load was suitable for conducting future QSTS simulations.

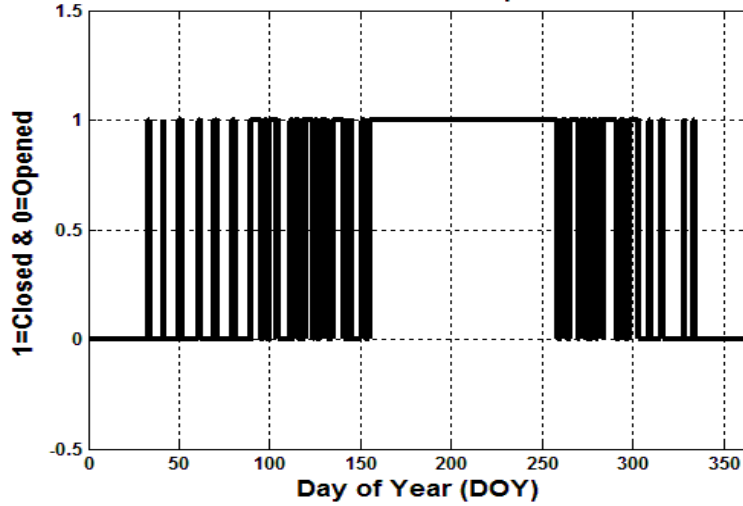


Figure 4.5: Derived Historical Switch Capacitor Operations on Feeder 03

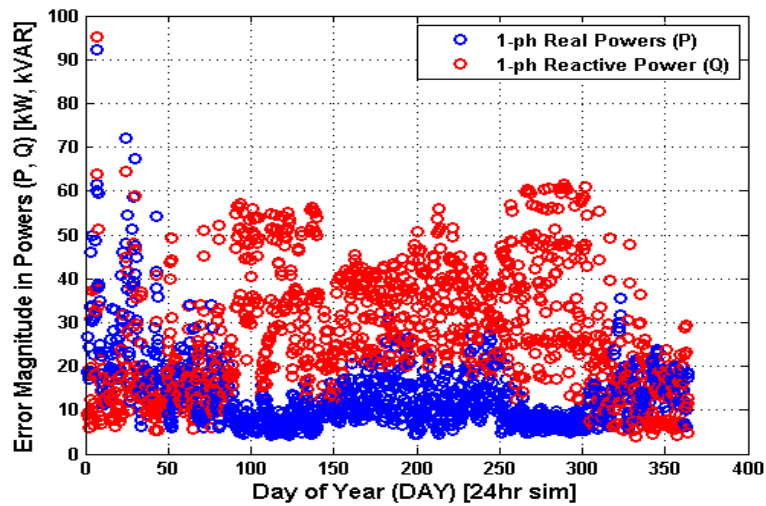


Figure 4.6: Annual QSTS Daily Average Single Phase P & Q Errors

From consulting the DNO engineers, the SCs connected to Feeders 02 & 03 are actually designed to operate under a VAR control strategy where a PF of 98.5% is maintained on the distribution substation un-regulated bus (primary side of the feeder SVRs/OLTCs) during the substation's peak loading period. Therefore, the combined

impact of all SCs connected to the substation determines the PF on the un-regulated bus. Because CAPER was provided six independent feeders, this exact control scheme could not be replicated. Now that the derived real and reactive power load shapes were verified, another style of reactive power control is enforced for future simulations where the SC references only the reactive power at the head-of-feeder and energizes if the total kVAR surpasses 1.1 times its capacity. During a leading PF condition, the capacitor will trip off-line if the measured reactive power is greater than 0.8 times its capacity.

When previously verifying the QSTS simulation on Feeder 03, default OpenDSS tap controls were used. According to [29], these controls have very basic functionality and do not accurately model the performance of how most modern tap changer controls work. The common control mode typically found as the default setting on most SVRs when provided by vendors is called sequential control [31]. The difference between these two is that after a voltage violation occurs, the default DSS control disregards the measured voltage until the timer expires and then checks it right before actuating a tap change. On the other hand, a sequential controller continuously monitors the voltage and resets the timer if the voltage falls within the BW again [29]. Figure 4.7 shows the logic built in MATLAB to implement this sequential controller and its interaction between the OpenDSS feeder model. The only different between the OpenDSS default and sequential equivalent voltage regulator relay (VRR) controls is the red logic unit checking for a violation at each time increment when the SVR timer is initiated.

After this customized voltage regulator control was implemented and successfully tested, two other available methods are investigated: time-integrating mode and voltage averaging mode. Both are offered on a CL-7 Regulator made by Cooper Power Systems [31]. Time-integrating mode is similar to sequential mode other than that when the control voltage goes within the bandwidth again; the timer is decremented by an acceleration factor (such as 1.1sec) instead of resetting [29]. This method will operate identical to sequential mode if the voltage remains continuously outside of the bandwidth. This mode was again built in MATLAB with the logic presented below.

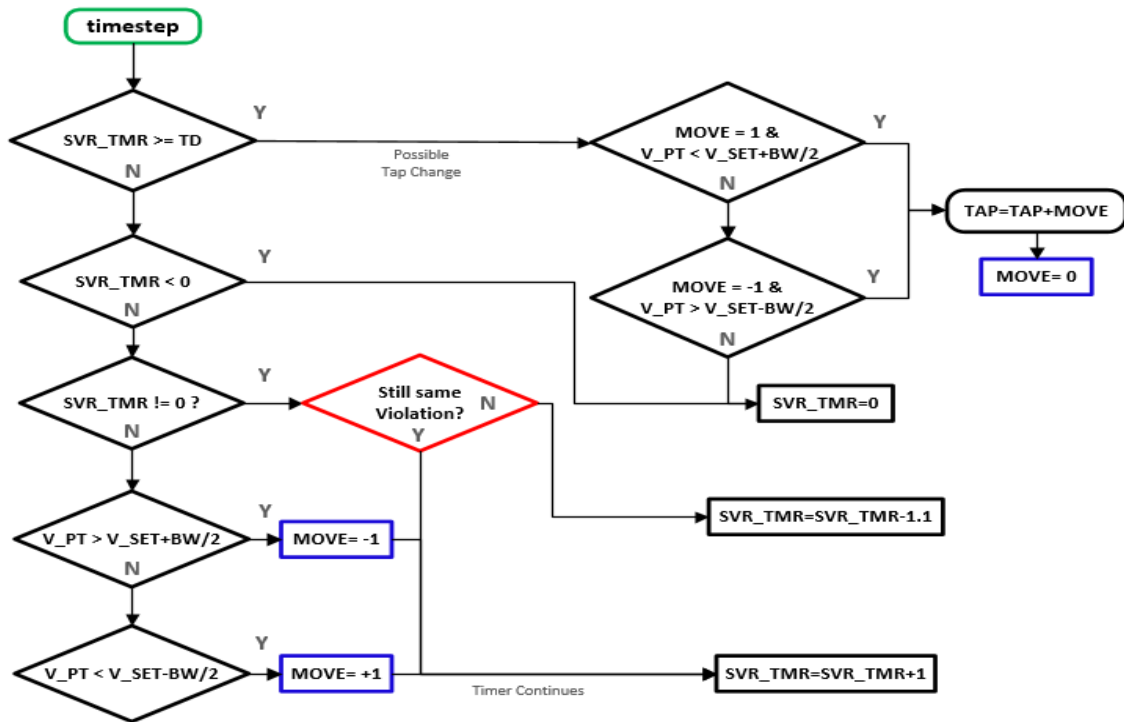


Figure 4.8: Time-Integrating VRR Control Mode

When a violation occurs in voltage averaging mode, the measured control voltages are monitored and an average is calculated over the duration of the TD. If this average is outside the control bandwidth, then the required number of taps needed to

bring the average value back to the voltage set point is calculated and instantly executed, limited to a maximum of five taps [31]. A flow chart displaying the logic behind this control mode is presented below in Figure 4.9. Note that this amount of computation requires a microprocessor being on-board of the voltage regulator relay (VRR).

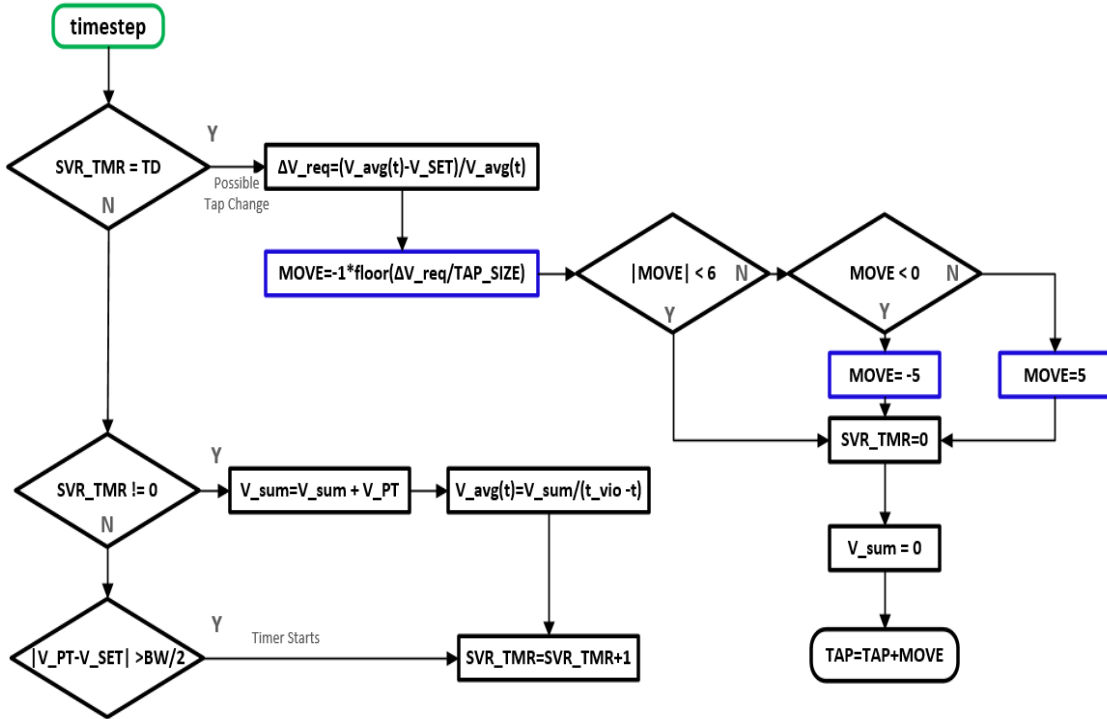


Figure 4.9: Voltage Averaging VRR Control Mode

The DNOs which provided the test feeders used in Chapter 3 have a company standard that on all 12.47kV and most 22.9kV/23.9kV distribution feeders, OLTCs at the feeder-heads with a $V_{SET} = 124V$; a BW of 1V, 2V, or 3V; and a TD of 30 to 45 seconds. To show the importance of properly modeling the control logic of these feeder OLTCs, QSTS annual simulations were conducted on Feeder 03 under each of the control modes previously described: OpenDSS Default, Sequential, Time-Integrating, and Voltage Averaging. Figure 4.10 provides the control winding voltage movements throughout an

entire year. Notice how the voltage is much more variable during the summer months even without DER-PV facilities connected.

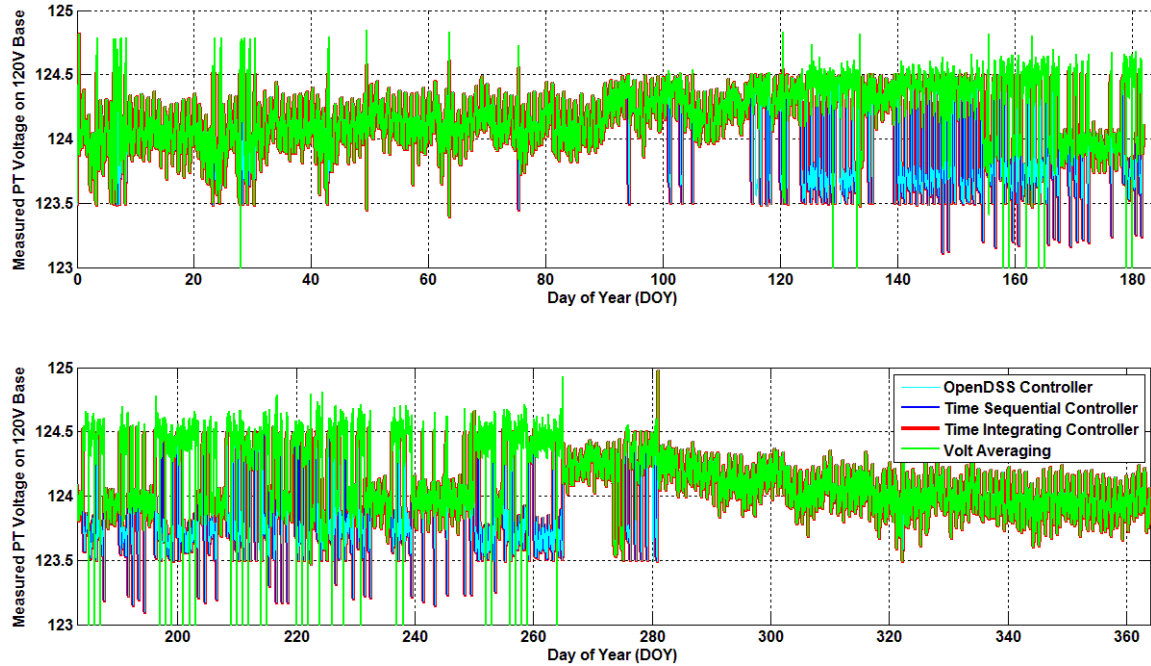


Figure 4.10: Annual Distribution of OLTC Control Voltage on Feeder 03

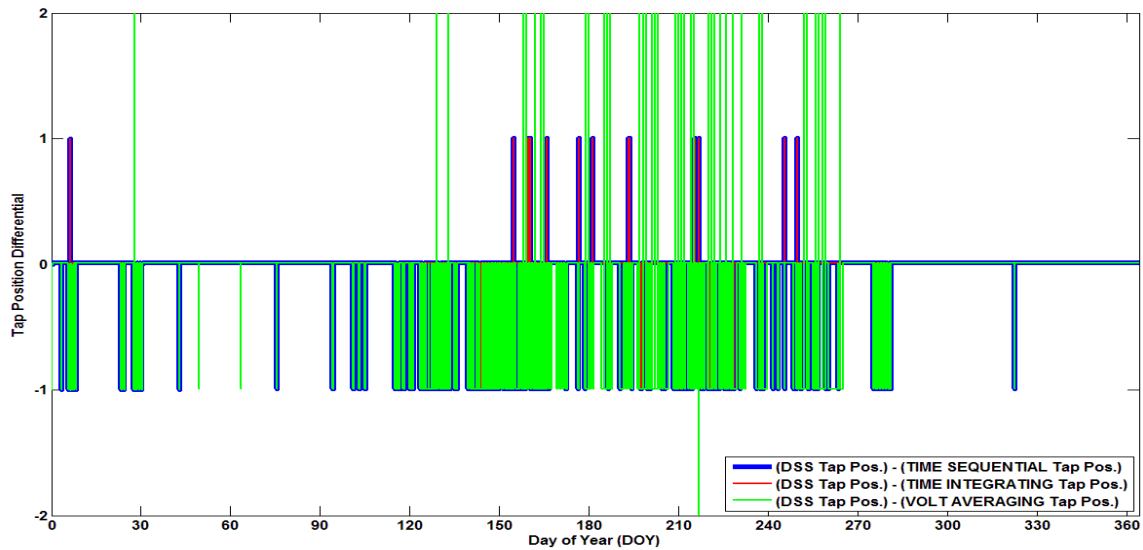


Figure 4.11: Annual OLTC Tap Position Differential per Control Scheme

In order to compare the OpenDSS Default OLTC controller to the other control modes, the difference in tap position at each time increment was calculated and presented in Figure 4.11. From inspection, it is obvious that the time sequential and integrating controllers behave differently than the OpenDSS default controller. On the other hand, the voltage averaging control mode was much more conservative in initiating a tap change therefore it followed a unique tap changing operation.

To further visualize the difference in OLTC control modes, the control voltage and tap position throughout day of year 213 is depicted in Figure 4.12. In this situation, the OpenDSS controller initiated a tap change near 16:00 while the sequential and time-integrating controllers help the tap position. Also, the voltage averaging controller did not initiate a tap change (shown in purple) because the voltage violation was not severe enough to justify a tap change. Thus, this visualizes the importance of properly modeling OLTC control modes in order to capture the actual OLTC responses to variable voltage.

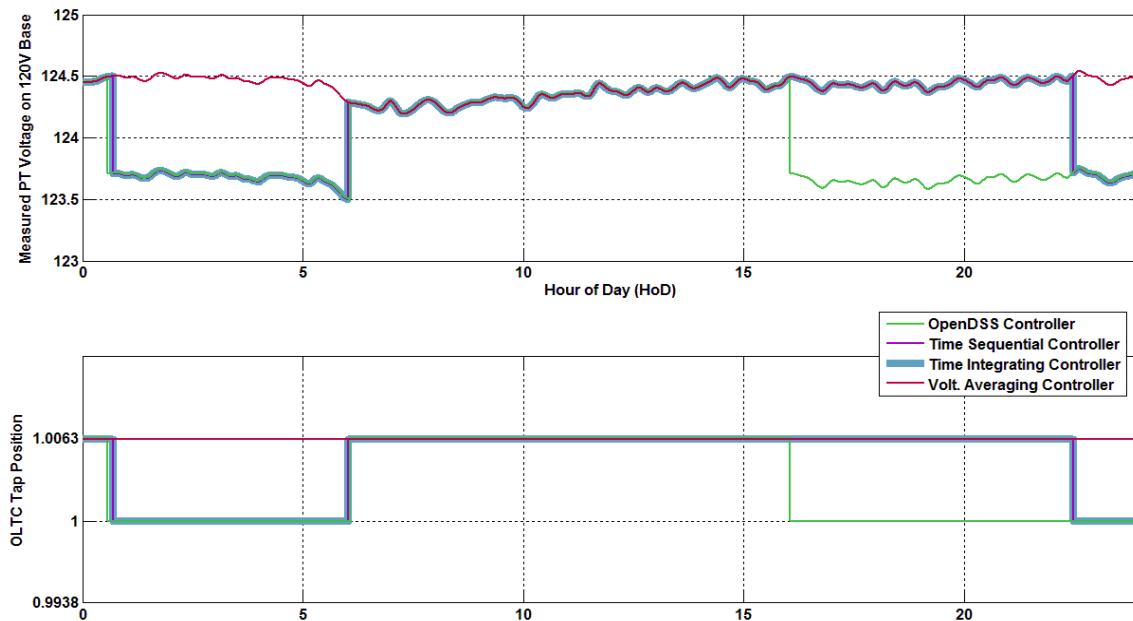


Figure 4.12: Difference in OLTC Controller Responses

4.2: Centralized Integrated Volt-VAR Control

Traditional voltage regulation schemes have the installed devices operate autonomously in a non-coordinated manner. The presence of DER-PV generation operating at unity power factor under this traditional voltage control scheme leads to a decrease in current flow and therefore an increase in system voltage. With renewable generation being very intermittent causes severe short-term voltage deviations on top of an overall long-term voltage rise. Additional wear and tear can occur on OLTCs and SVRs, potentially increasing operational costs that the local DNO is responsible for [32]. There is also a drastic increase in the risk of having a SVR fail to control the voltage of the regulated bus because the tap reaches its highest or lowest position. This condition has been observed during extreme reverse power flow situations and is commonly referred to as “reverse power tap changer runaway” [33].

In the 2000s, utilities were starting to move away from local autonomous control to adopting a more effective control strategy where communication channels to the VRDs were added. This enabled DNOs to remotely dispatch, on an hourly basis, the voltage set points and tap position of OLTC/SVRs and the state of SCs [34]. Most recently with smart grid initiatives, a new voltage control strategy has emerged utilizing two-way communication and assessing real time (RT) streams of system information from Advanced Metering Infrastructure (AMI) to optimize the operations of all VRDs connected to a network. Utilizing a TCP/IP based wide area network, a distribution substation status and performance can be assessed from the use of a Distribution Management System (DMS). Any DMS offers two sets of application functions: RT and

analytical. RT applications are designed to assist the operator in keeping the system balanced and help ensure the delivery of uninterrupted power to customers [22].

The ideal operation of a distribution feeder occurs when losses are minimized, feeder PF is maximized, and a flat voltage profile is maintained during all loading conditions. These objectives can be divided into two groups, VAR Optimization-Power Factor Correction and Conservative Voltage Reduction (CVR). Coordinated switched capacitor bank controls can reduce electrical losses by lowering the required line current and reduce the energy supplied to loads [22]. CVR is the coordination of OLTC/SVR controls to reduce feeder voltage levels in order to observe a load reduction. A 1% change in voltage results in a 0.2% to 1.5% change in real power and a 2% to 6% change in reactive power [35]. A DMS application function called Integrated Volt-VAR Control (IVVC) incorporates both VAR Optimization-PF Correction and CVR by coordinating all VRD controls to achieve an optimal VAR and voltage profile [35]. A communication infrastructure is designed to send remote control signals to alter SCs on/off position, adjust feeder SVRs/OLTCs tap position, and even adjust the SVRs/OLTCs set points.

In order for the optimization application behind IVVC to work properly, RT feeder voltage and current flow from regulators, capacitors, and additional monitoring points (customer AMI meters or MV sensors) need to be continuously analyzed. From these RT measurements, the application can determine which SC bank and SVR to operator in order to achieve an optimum performance of the distribution system. This is commonly referred as an Optimum Power Flow (OPF) problem, and the optimization application that solves this OPF is usually an advanced Artificial Intelligence algorithm

which can adapt to any loading scenario [34]. The cost of additional communication lines and sensors is offset by two main drivers; regulation and stimulus programs. Government agencies are imposing regulation requiring DNOs to reduce energy consumption and peak demand. Stimulus programs such as energy efficiency projects, offer capacity (MW) releases when reducing losses and can normally be a very sizable benefit [35]. IVVC can easily achieve these goals and thus the DNO will be rewarded more than just the immediate energy purchase savings.

The IVVC functionality of minimizing losses and attempting to maintain a flat voltage profile (2 volt bandwidth) is in reality an ancillary function during non-peak operation of another program implemented by the DNO of Feeder 04 known as Distribution System Demand Response (DSDR) [19]. The primary function of DSDR is to perform demand reduction at peak loading conditions by dropping OLTC and feeder SVR voltage set points system wide. As of date, the DSDR program currently supports over 1,000 MW of peak shaving, avoiding the need for this utility to build more expensive peaking generation facilities [19]. When this program was initiated back in 2007, the operational impacts of DER-PV to feeders were not accounted for in the fundamental design. Introducing generation on the feeder far away from the substation will greatly impact real power flow direction and thus resulting in an unexpected inverse voltage profile. This forces the ancillary function of DSDR to actuate more frequently to maintain the desired bandwidth. Currently with a significant capacity of connected utility-scale PV generation throughout this DNO's service territory, distribution planners are now forced to rethink traditional voltage drop mitigation strategies.

To present an example of how DSDR can be modeled in OpenDSS using QSTS, Feeder 04's model used in Chapter 03 was utilized with daily load shapes being associated to all spot loads. This distribution feeder can be considered an outlier to the group of test feeders because it has five SVRs positioned throughout the main and large lateral conductors with specifications of each presented below in Table 4.1. Notice how only two SVRs had singular phase control while others operated the phases separately.

Table 4.1: Voltage Regulation Device Settings

VREG #	OLTC	SVR1	SVR2	SVR3	SVR4	SVR5
Control Phase(s)	B	A,B,C	A	A	B	A
Conn. Phases(s)	A,B,C	A,B,C	A,B,C	A,B,C	A,B	A
V-Set (V)	124	124	125	125	125	125
B.W. (V)	2	2	2	2	2	2

On top of this, three 1,200kVAR switched capacitor (SC) banks are connected at optimal locations presented in Figure 4.13. Because of legacy initiatives, two-way communication lines were installed and integrated with all SVR and SC controllers [19].

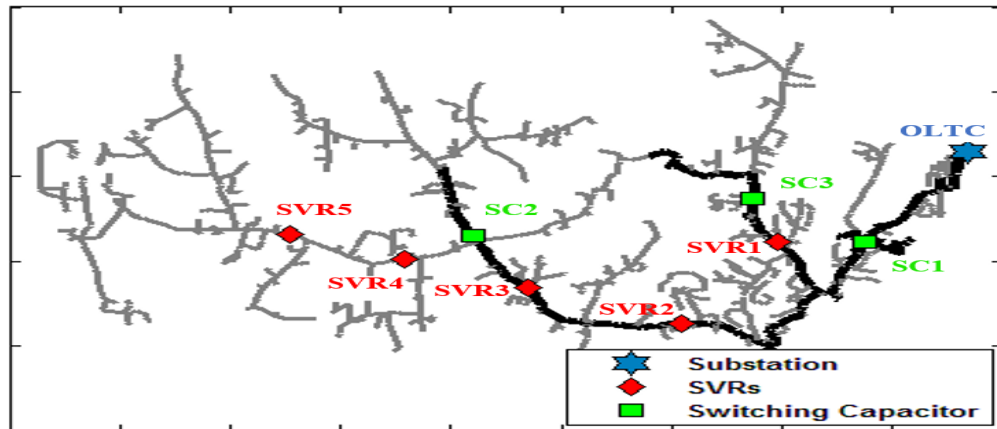


Figure 4.13: Location of Voltage Regulation Equipment on Feeder 04

Fortunately the DNO was able to provide CAPER with an annual report of all historical SC operations from a SCADA historian database with the capacitor bank states

presented below in Fig. 4.14. The states were stacked on top of one another for easy visualization with the higher number out of each pair representing the “on” state.

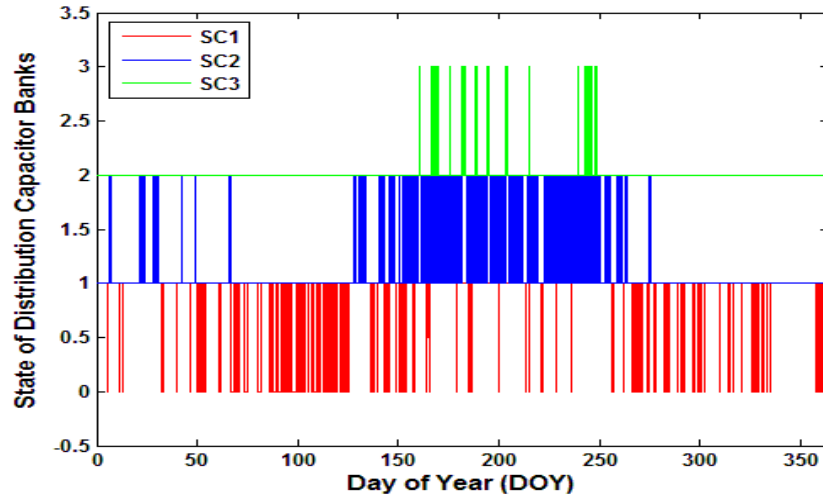


Figure 4.14: Annual Switch Capacitors Historical Operations on Feeder 04

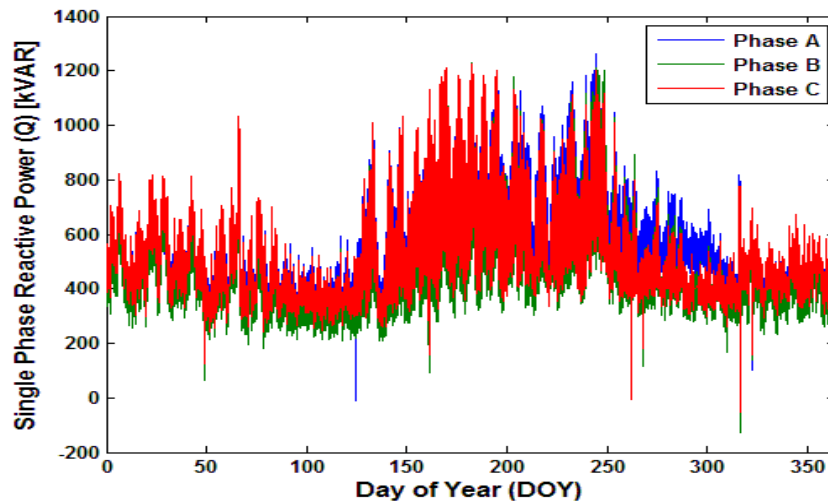


Figure 4.15: Annual Derived Reactive Power Demand on Feeder 04

A process similar to the one previously described was conducted where historical head-of-feeder measurements and historical capacitor states were used to construct the actual reactive power consumed by the connected load. The derived Q is shown in Figure

4.15 and indicates that a higher reactive power is consumed during the summer months while being stable during the rest of the year.

To observe how the DSDR program decides which switched capacitor bank to energize when the reactive power limit is exceeded, a one week run between DOY 164 to 171 was selected for QSTS simulation because SC3 was required at times. The real and reactive single phase DSS simulation results are presented below in Figure 4.16 with the associated error between DSS results and actual DSCADA field measurements are presented in Figure 4.17. Notice how the real power error was consistently less than 100kW per phase. On the other hand, the reactive power error had a broader range, sometimes spiking when a S.C. bank was energized or de-energized at an incorrect time. Spikes in the single phase reactive power originate from certain capacitors being switched at the incorrect times in a range less than 15 minutes. For demonstration purposes, this model was deemed accurate enough to expose the complexity of DSDR.

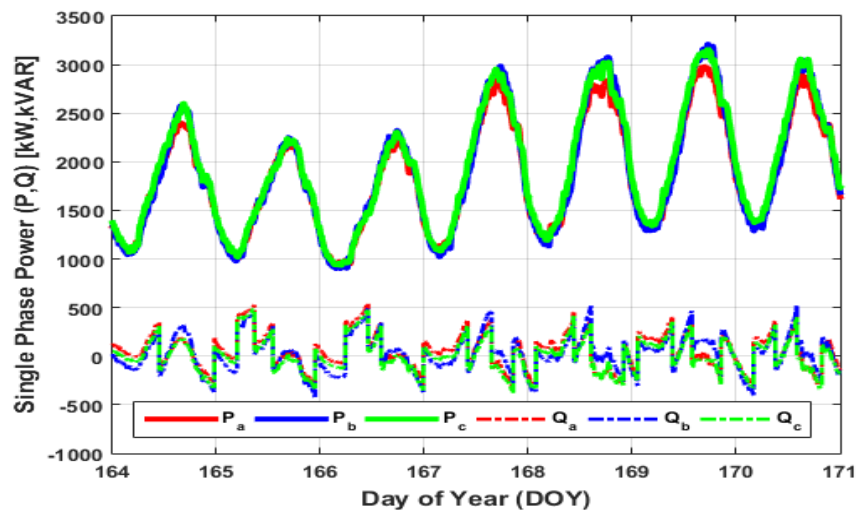


Figure 4.16: P & Q 1-Phase Power on Feeder 04 during a Summer Week

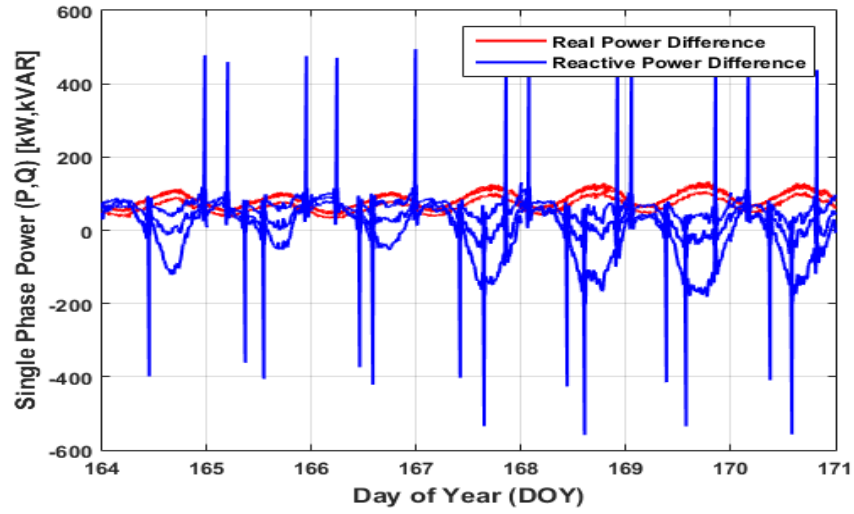


Figure 4.17: Error of Powers between DSCADA and OpenDSS on Feeder 04

The exact locations of these three S.C. banks are shown as green symbols in Figure 4.15. The operating conditions that force these three SCs to switch from on/off were discovered after overlaying the three phase reactive powers of each bank on top of one another. From observation of Figure 4.18, it was concluded the DSDR program enforces a priority system in which the order goes SC1, SC2, and then SC3.

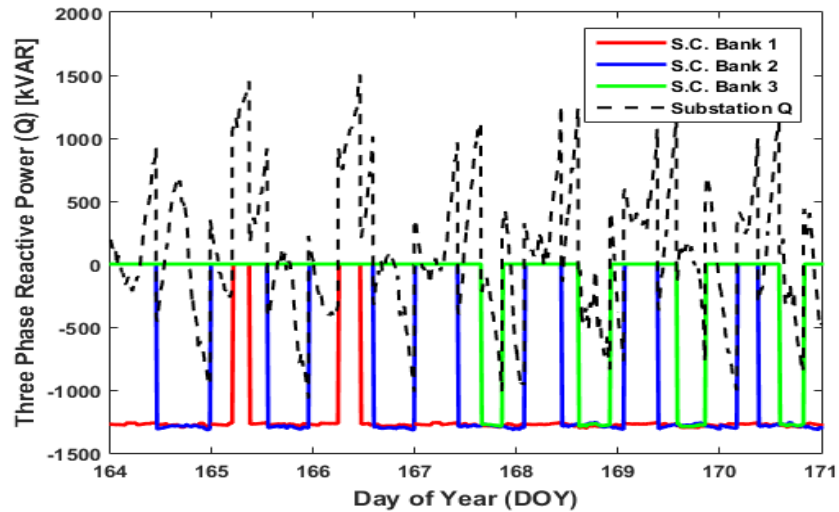


Figure 4.18: Reactive Power of Feeder 04 and Switch Capacitors during a Summer Week

This translates into if the DSDR system observes a reactive power level greater than the defined threshold and only SC1 is energized, SC2 would be commanded to trip on-line for PF correction. This therefore flattens the voltage profile and decreasing losses.

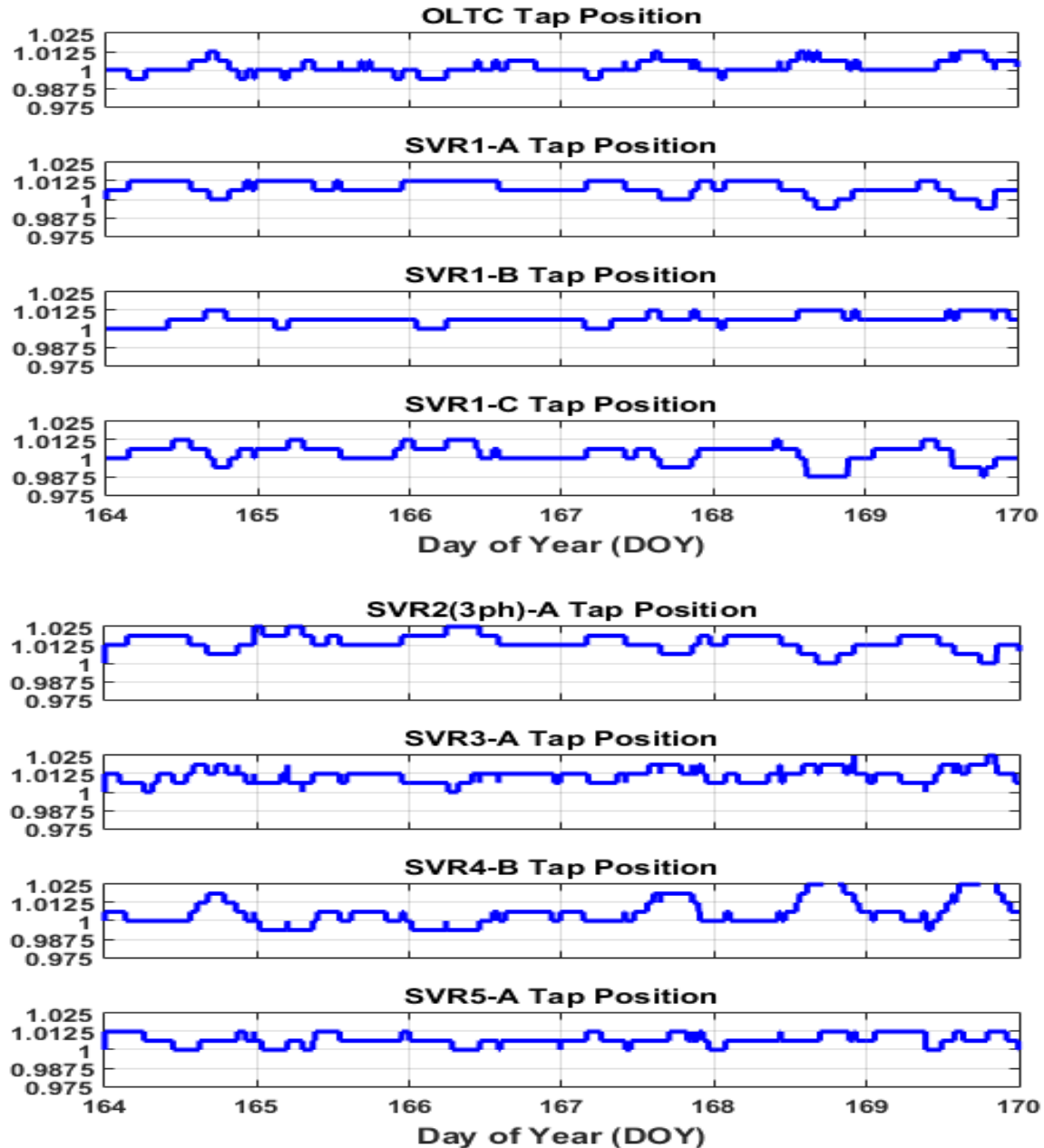


Figure 4.19: OLTC/SVRs Tap Positions on Feeder 04

The settings presented in Table 4.1 were enforced on all SVRs and the OLTC during the one week simulation and the resulting tap positions to keep the control voltages within the set BWs is shown in Figure 4.19. The SVRs connected further away from the substation acted more often and used a larger range of tap positions. These sections had light power flow and therefore more prone to substantial voltage deviations throughout the time shift of consumed power.

The voltage regulation scheme of DSDR on Feeder 04 heavily depends on local bus measurements and communication interfaces to all pieces of equipment. This example highlights that complex volt/VAR programs have already been implemented by Utilities because the capital investment of additional voltage regulation equipment is less than the cost of adding new peak-shaving generation. Each SVR connection to a distribution system introduces an additional layer of complexity and is amplified when a customer connects a DER-PV facility. The DSDR's primary objective to lower the voltage profile in-order to minimize power consumption will continuously fight against the inevitable voltage rise associated with distributed generation, noticeably increasing SVR operations. Therefore, feeders with DSDR implemented cannot support high levels of DER-PV. The original philosophy behind DSDR requires a fundamental revision to allow customers to connect DER-PV facilities downstream of a SVR.

4.3 – Quantifying the Level of Variability in Solar PV Generation

Through CAPER, a local DNO provided seven DER-PV facility's complete annual datasets of historical measurements. The location of each facility is illustrated in Figure 4.20 with three of the sites (shown in red) having solar irradiance measurements

available along with the associated real and reactive power output. The four other DER-PV facilities, as shown in green, only had 1-minute power output measurements available but provided insight into how larger DER-PV facilities performed.

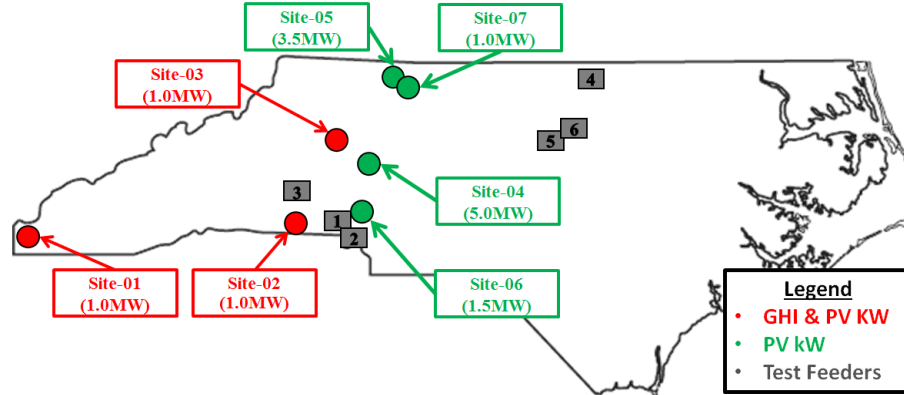


Figure 4.20: PV Plant Locations of Annual Measurements

For future QSTS simulations to execute successfully, it was essential that these DER-PV raw datasets were checked for completeness and accuracy. Therefore, data quality algorithms similar to the ones used on the DSCADA historical datasets were applied to re-structure and linearize any missing data points.

When planning for potential excessive VRD operations, [36] presented a novel metric called the “Variability Index” (VI) to successfully quantify solar irradiance variability over a certain time interval. This metric compared the deviations in measured global horizontal irradiance (GHI) and calculated clear-sky irradiance (CSI) over a defined time step. With VI, the quality of measured solar irradiance can be compared between days and locations. One disadvantage of strictly using VI to classify days is that extremely overcast/rainy conditions will present themselves as low VI values. Therefore, another coefficient called the Clear Sky Index (CI) is used to measure the available solar

energy throughout a given day. CI uses Direct Beam radiation ($B_n(t)$) measurements to compare measured energy against available extraterrestrial solar energy densities [37].

To begin the derivation for concluding the available CSI during each day at Sites #1 - #3, the amount of available radiation at the outer part of the Earth's atmosphere was found. Commonly referred as the extraterrestrial radiation, it can be estimated using Eq. (4.3) [37]. The amount of radiation that reaches the Earth's surface is dependent on the Air Mass (AM), Eq. (4.4), shifting to account for the Earth's orbit around the sun [38].

$$I_0 = 1367.7 \cdot \left(1 + 0.033 \cos \left(\frac{2\pi}{365} \cdot DOY \right) \right) \quad (4.3)$$

$$AM(t) = (\sin \beta)^{-1} \quad (4.4)$$

The Kasten model, Eq.'s (4.5 & 4.6), was used in determining the CSI and the inputs to this simple model include I_0 , AM, the adjusted turbidity coefficient (T_{LI}), the solar altitude angle (β), and the site altitude in meters (h) [38]. The solar altitude angles were calculated on a minute basis using a model developed by NOAA [23].

$$CSI = a_1 \cdot I_0 \cdot \sin(\beta) \cdot \exp(-a_2 \cdot AM(t) \cdot f_{h1} + f_{h2} (T_{LI}(t) - 1)) \quad (4.5)$$

$$\text{Where:} \quad f_{h1} = \exp\left(-\frac{h}{8000}\right) \quad \& \quad f_{h2} = \exp\left(-\frac{h}{1250}\right) \quad (4.6)$$

$$a_1 = (5.09 \cdot 10^{-5}) \cdot h + 0.868 \quad \& \quad a_2 = (3.92 \cdot 10^{-5}) \cdot h + 0.0387 \quad (4.7)$$

Ineichen and Perez [38] incorporated additional correction coefficients (a_1 & a_2) which were also dependent on the solar elevation angle as shown in Eq. (4.7). It was proven that these coefficients drastically increased the accuracy of the Kasten model. They also derived an adjusted turbidity coefficient (T_{LI}) by first calculating the direct

beam irradiance $B_{ncl}(t)$ with Eq. (4.8) using a Linke Turbidity coefficient (T_L) equal to 3. Then, Eq. (4.8) was inverted to extract the turbidity factor (T_{LI}) as shown in Eq. (4.9). This was completed to increase the stability of the turbidity factor during the day and was proved to be much more stable than the original Linke Turbidity coefficient in [38].

$$B_{ncl}(t) = (0.664 + 0.163 / f_{hl}) \cdot I_0 \cdot \exp(-0.09 \cdot AM(t) \cdot (T_L - 1)) \quad (4.8)$$

$$T_{LI}(t) = 11.1 \cdot \ln \left(\frac{(0.664 + 0.163 / f_{hl}) \cdot I_0}{B_{ncl}(t)} \right) \cdot \frac{1}{AM(t)} + 1 \quad (4.9)$$

Equations 4.3 – 4.9 were applied at each minute interval throughout the 2014 year at the first three sites. To illustrate how the CSI and B_{ncl} paths vary throughout the year, Figure 4.21 presents the profiles of two days, 1/1 and 6/1. From observation, it is clear that there is more available solar energy during the summer days because the CSI and B_{ncl} have greater peaks and durations on 6/1 compared to 1/1.

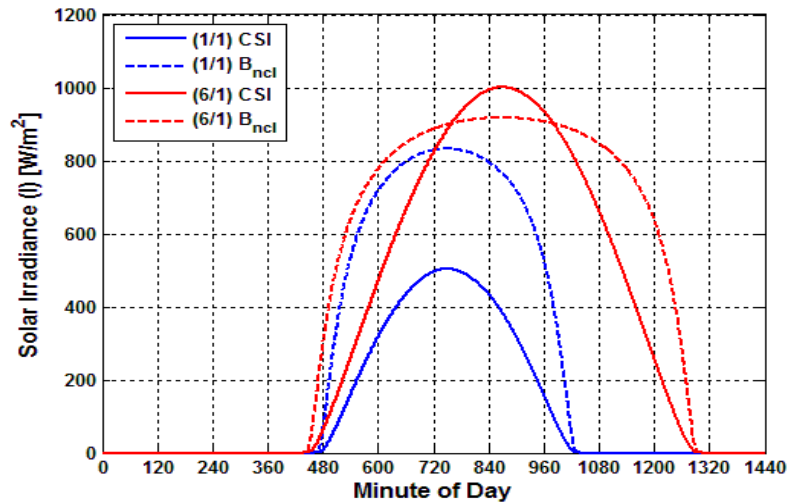


Figure 4.21: CSI and B_{ncl} Profiles on Sample Days

From the constructed CSI profiles, the Variability Index (VI) was established by applying Eq. (4.10) [36]. The VI can be thought of as the ratio of “length” measured GHI against time to the “length” of (CSI) against time. Clear-sky days have a VI near 1 and increased as the GHI path varied away from the calculated CSI profile. To establish the daily Clear sky Index (CI) from historical measurements, the results from Eq. (4.8) were used to find the ratio of aggregated measured direct beam irradiance to the summation of the derived $B_{ncl}(t)$, as shown in Eq. (4.11). Now, a day with VI less than 2 can be classified as either “clear” or “overcast” by observing if the CI is greater or less than 0.5.

$$VI = \frac{\sum_{t=2}^n \sqrt{(GHI(t) - GHI(t-1))^2 + \Delta t^2}}{\sum_{t=2}^n \sqrt{(CSI(t) - CSI(t-1))^2 + \Delta t^2}} \quad (4.10)$$

$$CI = \frac{\sum_{t=1}^{1440} B_n(t)}{\sum_{t=1}^{1440} B_{ncl}(t)} \quad (4.11)$$

To demonstrate that the increase in solar irradiance variability will result in a higher VI quantity, days were sampled from Site #3 with the closest integer VI levels from 1 to 20. The associated GHI and CSI profiles are presented in Figure 4.22 in blue and red respectively. Notice how the quality of the profile decreases as the VI increases visually proving that this metric can quantify variability.

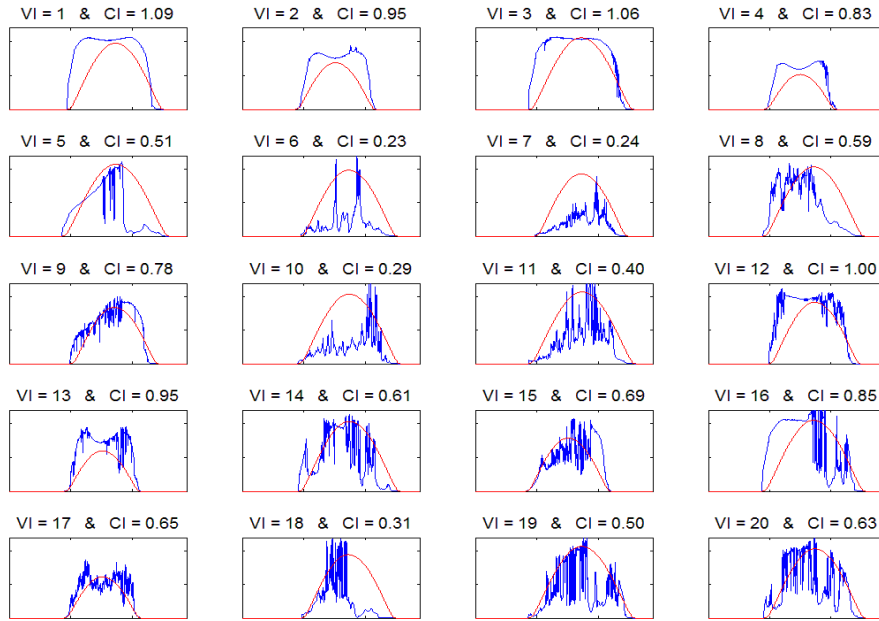


Figure 4.22: Sampled Days of Increasing VI at Site 03

The VI and CI solar coefficients observed to follow an “arrow” like relationship after inspecting Figure 4.23 with larger VI values typically resulting in less observed total solar energy. Utilizing this relationship, Sandia National Laboratory devised a solar day classification scheme of which each solar profile can be considered one of five days: overcast, clear, mild, moderate, and high variability [18]. The red lines overlaid on the figure represent the partition between these five solar day categories.

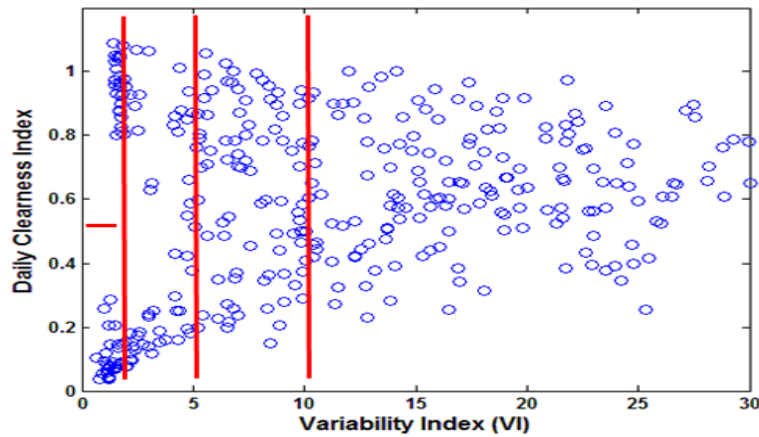


Figure 4.23: Relationship between VI & CI at Site 03

As an example, the solar profiles from Site #3 were sorted into one of these five categories. A single day's historical GHI measurements (blue) and associated CSI profiles (red) were selected and provided in Figure 4.24.

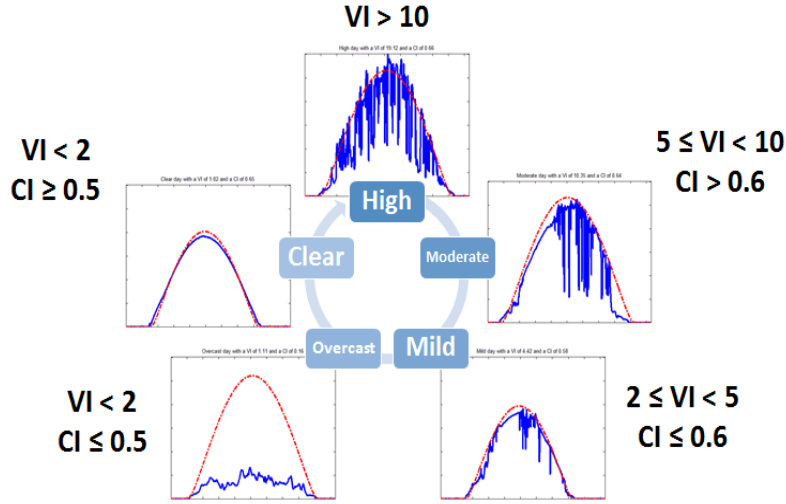


Figure 4.24: SNL Solar Day Classification Scheme

Because four of the sites did not have coincident historical GHI measurements available another metric presented in [28] called the Daily Aggregate Ramp Rate (DARR) was applied to all seven sites. DARR is found by the summation of per-unit real power ramp rates as shown in Eq. (4.12). This coefficient is a function of the magnitude of the observed ramp rates and therefore accounts for the impact of cloud coverage and movement. Using only DARR, it is now possible to compare the quality of generated power from DER-PV facilities of various configurations and locations.

$$DARR = \sum_{t=2}^{1440} \frac{|P(t) - P(t-1)|}{P_{rated}} \quad (4.12)$$

On a perfectly clear sky day, the expected DARR is approximately 2 p.u. with a generation profile peaking at rated output before diminishing in the evening [28]. The

most extreme variable days resulted in a DARR of 70-80p.u. The resulting site DARRs can also be placed into five categories like VI, ranging from very stable to highly variable days [28]. With the annual distributions presented in Table 4.2, notice how the larger sized DER-PV facilities result in significantly more Category 5 days. This is due to the fact that this coefficient is highly influenced on the plant's size, shape, and per unit base.

Table 4.2: Daily PV Plant Generation Categorized by DARR

Site	Cat. 1-OC Total Days: (overcast)	Cat. 1 Total Days: $DARR < 3$	Cat. 2 Total Days: $3 \leq DARR < 13$	Cat. 3 Total Days: $13 \leq DARR < 23$	Cat. 4 Total Days: $23 \leq DARR < 33$	Cat. 5 Total Days: $33 \leq DARR$
1 _(1MW)	20	26	100	66	59	86
2 _(1MW)	60	21	152	82	29	30
3 _(1MW)	27	32	91	67	47	101
4 _(5MW)	1	1	57	31	23	247
5 _(3.5MW)	2	1	73	28	40	216
6 _(1.5MW)	18	44	90	64	57	85
7 _(1MW)	28	44	118	86	58	23

VI and DARR should be closely correlated because both measure the variability of solar irradiance directly and indirectly. Figure 4.25 confirms this linear correlation after applying Eq. (4.10) on the measured GHI and Eq. (4.12) on Site 03's generation output. Since DARR takes an aggregate of normalized kW measurements, this coefficient will be impacted by the magnitude of energy production.

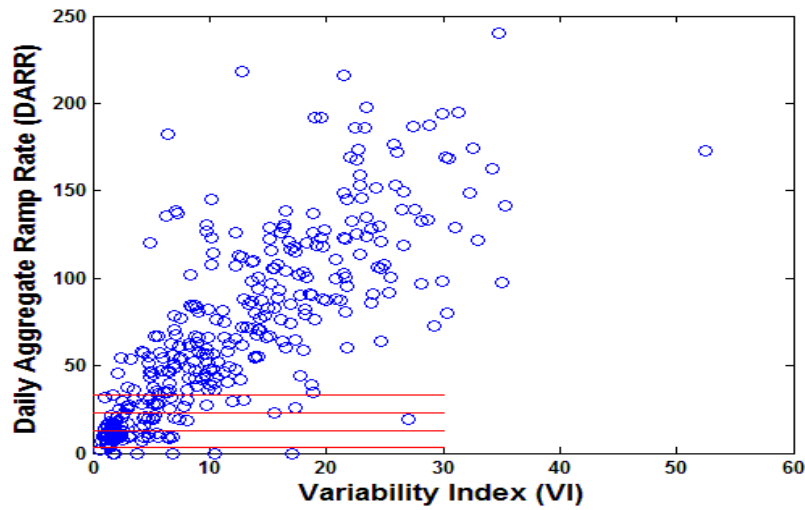


Figure 4.25: Relationship between Site 03 VI & Site 04 DARR

To show the effect that plant size has on observed extreme ramp rates, cumulative probabilities of observed plant 1 minute ramp rates were found in each DARR category. As an example, the uppermost observed 0.1% ramp rates of Site #4 (5MW DER-PV) are presented in Figure 4.26. Notice how the severity of the real power ramp rates increased as the DARR category increased.

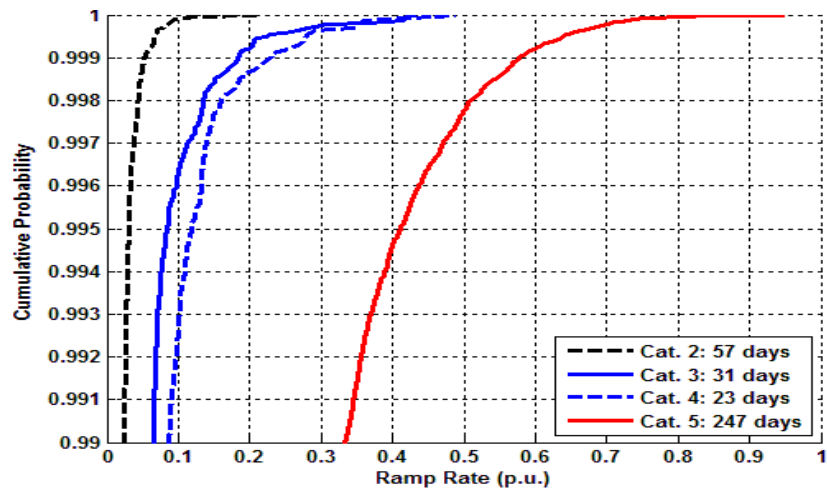


Figure 4.26: Cumulative Probability of Site 04's Ramp Rates

After applying Eq. (4.12) to each site's annual historical plant output, the cumulative probability curves of Category 5 days were selected and shown in the figure below. Because all of these DER-PV facilities are multi-megawatt and constructed with a uniform megawatt-array approach, it can be noted that extreme p.u. magnitudes decrease as the size of the facility increases [28]. This is due to geographic dispersion of solar irradiance where installing additional PVAs increases the total surface area. This will decrease the chances of travelling clouds casting a shadow over the entire facility and having all connected PV modules dropping in DC generation.

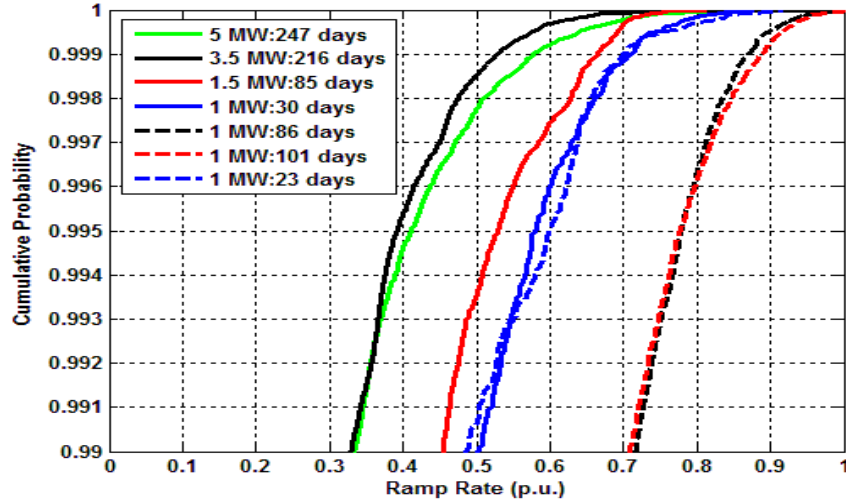


Figure 4.27: DARR Category 5 Days Ramp Rate Distribution per PV Site

With these three solar coefficients (VI, CI, and DARR), the daily historical DER-PV generation profiles can be effortlessly described. They can also be utilized to select critical days that will significantly impact voltage regulation equipment. Future forecasting models can be constructed to predict these coefficients and a potential application of this aspect will be presented in Chapter 5.

4.4 DER-PV Impact to Voltage Regulation Equipment Operations

Utilizing the same QSTS simulation architecture as described in Section 4.1, two of the test feeders, 02 and 03, were selected to have future DER-PV facilities introduced at various locations along each feeder. Two different Point of Interconnection (POI) locations were selected, as illustrated in the Figure 4.28. Facility nameplate ratings were selected based upon the static hosting capacity results introduced previously in Chapter 3. The POI's upstream impedances were also considered in the placement to observe the impact this aspect had on the additional operations of voltage regulation equipment.

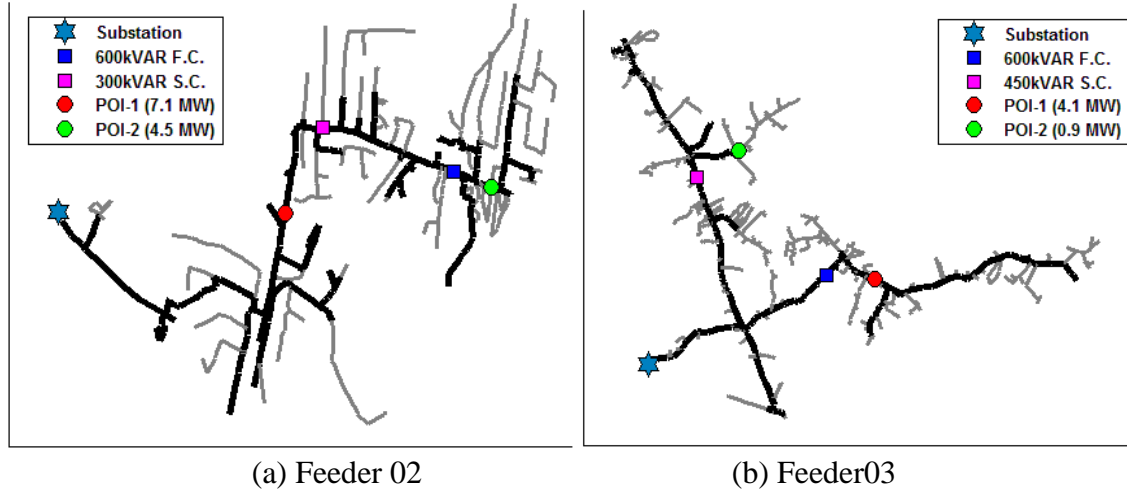


Figure 4.28: DER-PV Point of Interconnections Test Locations

The DER-PV plant outputs were driven from the historical power measurements from either Sites #1 or #4 with original capacities of 1MW and 5MW. To create the pseudo PV daily load shapes, the measurements were converted to per-unit before being multiplied by the new DER-PV capacity. Because annual QSTS simulations are time intensive, only a select period was initiated. Figure 4.29 was constructed to decide what time period to run. The solar coefficient, CI, which relates a numerical value to the total level of observed solar energy, was provided in red. Per each feeder, the 10AM to 4PM

average load was also provided in blue. From this time interval, monthly load levels were converted to per-unit with a base of respected peak load. To form a relationship between solar energy and load, the difference between per-unit values was found (black). From observation, it can be concluded that March, April, May, and October have the largest difference between load and solar energy. In other words, these months have a higher probability of long-term voltage rise and extreme reverse power flow events occurring.

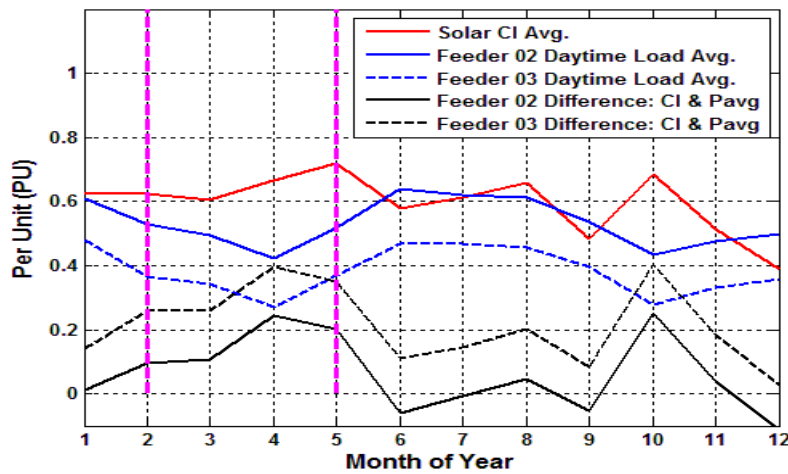


Figure 4.29: Observed Solar Energy and Daytime Load Metrics

Figure 4.30 presents the average VI from Site #3 and DARR from Site #4, chosen since they were in close proximity to each other as well as Feeders 02 & 03. As it turned out, the summer months had greater variability and both coefficients followed one another very closely. It was decided this was not a major concern because DER-PV generation will cover a smaller proportion of load during these months and therefore a smaller amplitude of the variability in voltage will be observed.

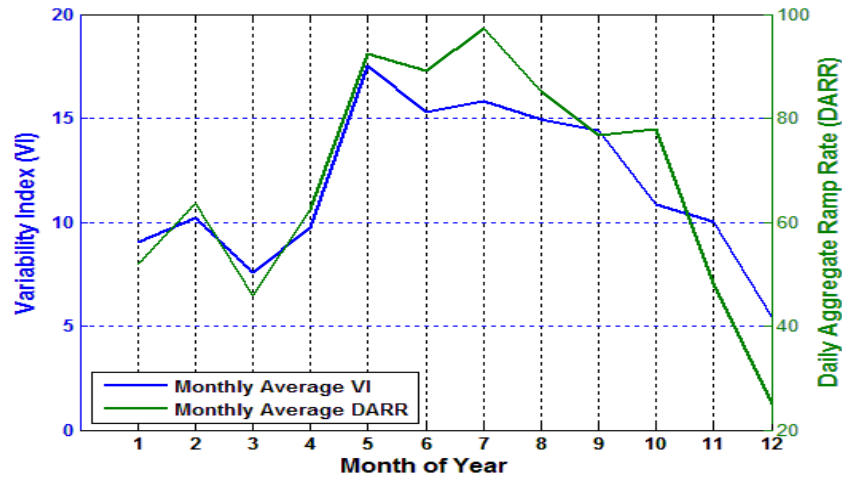


Figure 4.30: Monthly Observed Solar Variability Metrics

From this reasoning, QSTS simulations were conducted from 2/1 to 5/1 with two different DER-PV's POI locations on Feeders 02 and 03 taking approximately 10 to 12 hours of simulation to complete. The simulation time step was set to one second due to this being required for the MATLAB OLTC and SC controls to properly enforce their time delays. Many aspects on each distribution feeder were captured including all node voltages, power flow at the head-of-feeder, tap changes, switched capacitor reactive power/ position, and DER-PV output. Line currents and power flow were not captured throughout the selected period due to the immense dataset it would generate. As a work around, only key days were re-simulated if required to capture line power flow.

Initial post-analysis consisted of observing the cumulative number of tap changes on the OLTC per scenario. The results of these three month runs on Feeders 02 & 03 are provided in Figure 4.31. Observe that extreme voltage fluctuations did not alter on Feeder 02 even with much larger DER-PV capacities. This is due to the short distance this feeder spans and therefore high load density. Feeder 03 had some drastic increases in the number of tap changes especially at the POI-1 location. This was expected due to it being

observed in Chapter 3 that Feeder 03 had a very high voltage sensitivity of POIs located significantly further away from the substation.

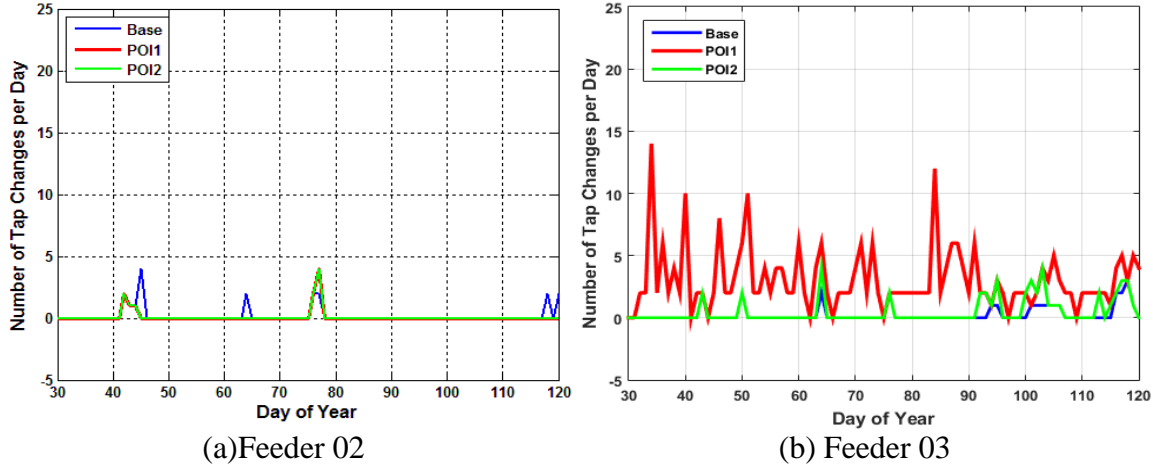


Figure 4.31: Cumulative Daily OLTC Tap Changes

Selecting the peak day of Feeder 03's OLTC operational impact (DOY=35), the OLTC control voltage and tap position are presented in Figure 4.32 (a) & (b). From this, it was obvious why there were 14 additional operations observed during the POI-1 case. This is a prime example of how solar energy can have very strong variability and wreak havoc to voltage regulation equipment. A sequential controller was implemented during these simulations, modeled as traditional localized control dependent solely on measurements taken from the secondary side of the distribution feeder's autotransformer. Additionally, to illustrate a unique circumstance that can occur when the larger DER-PV unit can be beneficial, DOY 101 was selected and the OLTC's VRR control voltage and tap position are provided in (c) & (d). Note how the voltage steadily increased from 8am until solar noon, actually forcing an additional operation in both DER-PV cases. Interestingly the 500kW DER-PV at POI-2 forced an additional boost operation during the peak loading period, approximately 6 p.m. This did not occur with the POI-1 case

because the generation was still able to cover enough load to prevent a system voltage drop that typically occurs during heavier loading periods. This nuance would not have been noticed without detailed time-series simulations.

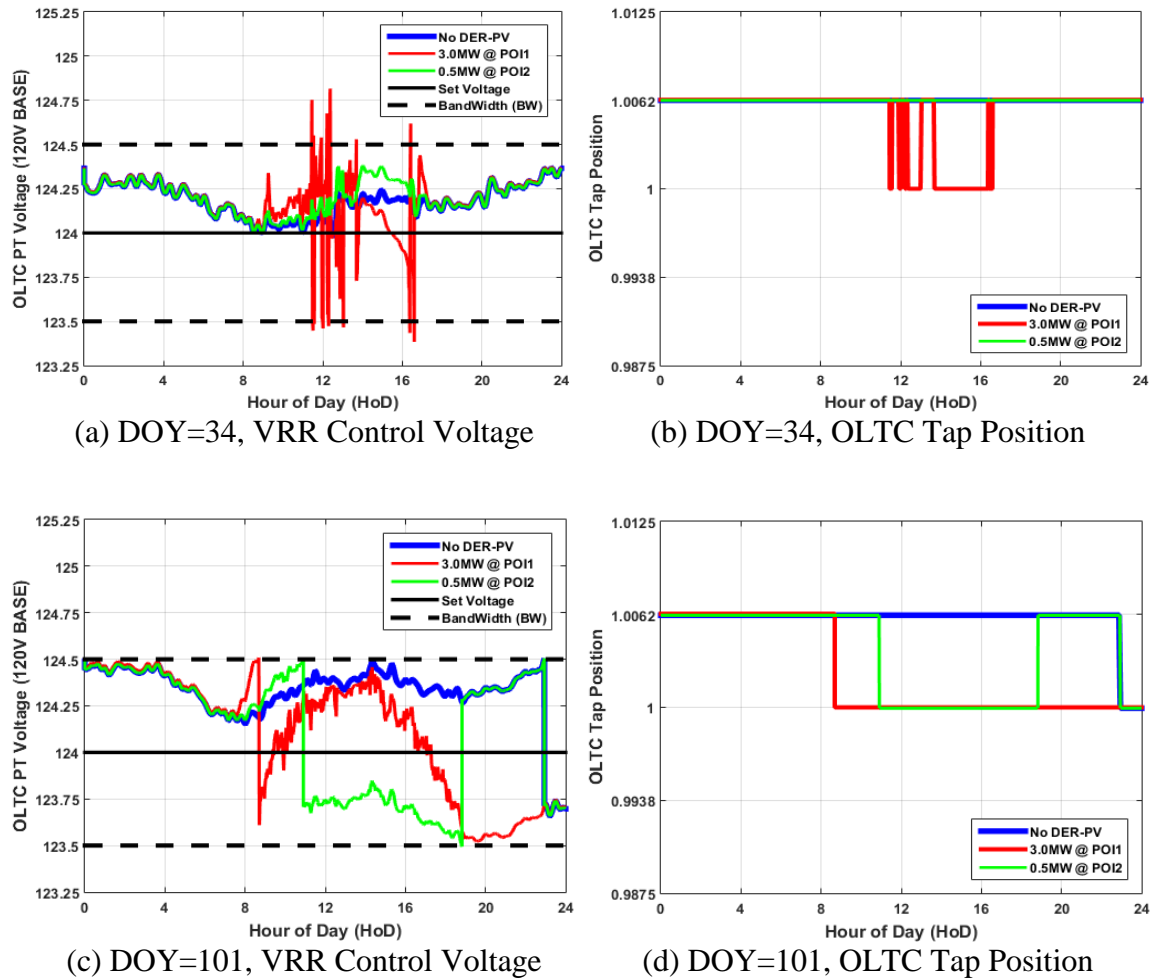


Figure 4.32: Voltage Deviations during Select Days on Feeder 03

To capture a more generalized idea on the impact of utility-scale DER-PV facilities, one week was selected with the lowest difference between load to generation. Referencing Figure 4.29, the week of 4/7 to 4/13 shows a significant chance of reverse power flow occurring and therefore extreme long term system voltage rise. The real power measured at the head of feeder is presented in Figure 4.33 of both DER-PV

penetration cases. Associated daily solar coefficients were included as reference especially when observing the magnitude of variability and energy of the reverse power flow profile. The observed minimum and maximum node voltages during the peak solar interval (PSI) of 10AM to 4PM were captured every 5 seconds and presented in Figure 4.34. Unfortunately long-term voltage violations did occur with the 3MW DER-PV in operation, concluding that this size is not acceptable at its POI without mitigation.

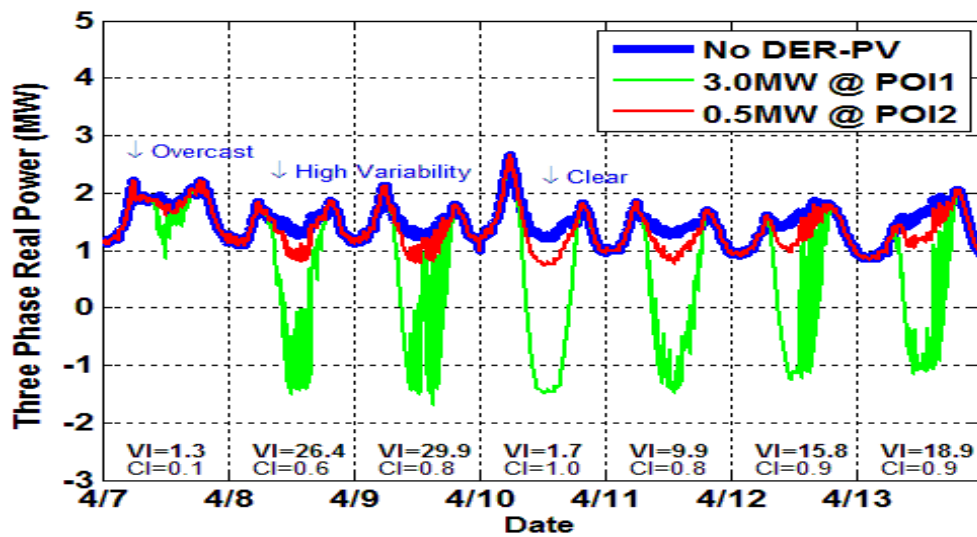


Figure 4.33: Impact of Connected DER-PV to Feeder 03 Load, One Week Span

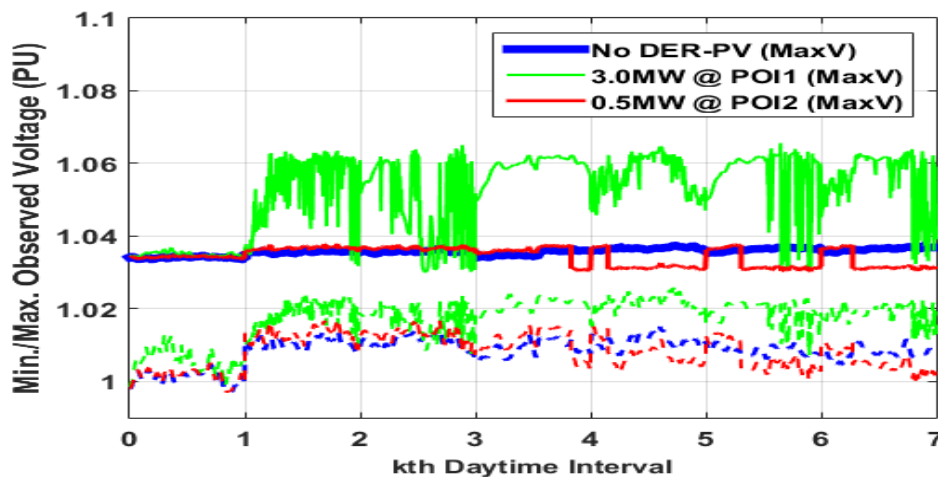
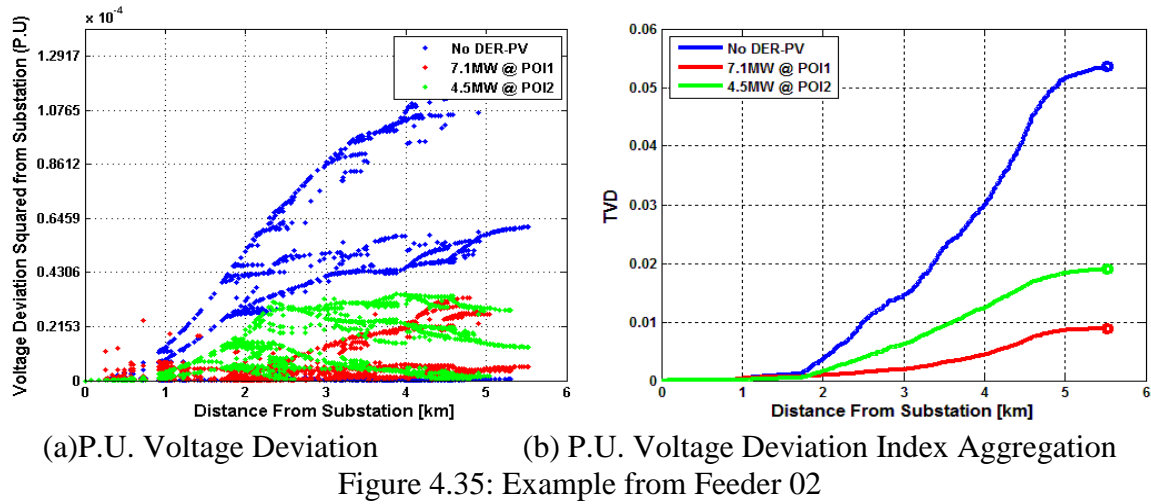


Figure 4.34: Feeder 03 Observed Voltage Range during Peak Solar Interval

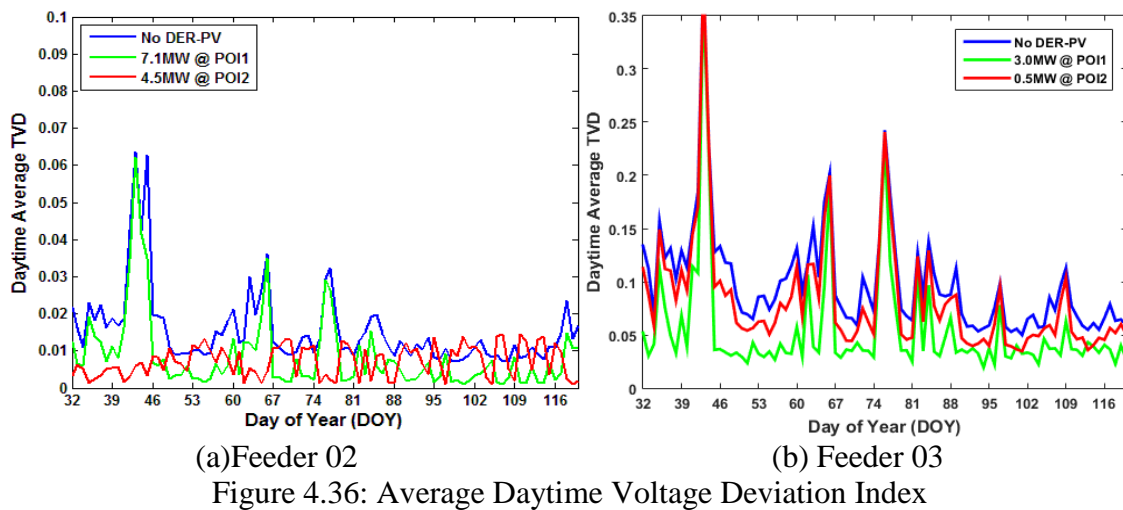
Instead of solely observing the complete feeder's voltage distribution, a metric presented in [39] was incorporated in this planning study called the voltage deviation index (TVD). This is the sum of the squared difference between the nominal voltage level considered to be the secondary side voltage on the OLTC autotransformers to all bus voltages. Using Eq. (4.14), TVD can be calculated on a time step basis. To understand how TVD can be interpreted, let us say there is significant voltage drop during peak load conditions. The TVD will increase in magnitude because the distribution network's voltage profile shifts downwards and therefore increase voltage headroom.

$$TVD(t) = \sum_{i=1}^N |V_n(t) - V_i(t)| \quad (4.14)$$

As an example to further illustrate the concept of TVD, a snapshot of Feeder 02's time series power flow was taken on DOY 110 at 11:23AM. The difference between the nominal voltage and all single phase node voltages, referred to as voltage deviation, was calculated per scenario and presented in Figure 4.35(a). Note how there is a positive correlation between voltage deviation and distance from substation, confirming that voltage drop is occurring. The results of a continuous aggregation of all node voltage deviations per phase and then averaging the three single phase values, the TVD per scenario is presented as the final open circle in Figure 4.35(b). Notice how the larger facility resulted in a lower TVD because the DER-PV raises the system-wide voltage due to current injection occurring downstream from the OLTC. This decrease in line current through the main conductor reduces the voltage drop. Therefore, the feeder voltage headroom is decreases as well as the TVD.



During the previous three month QSTS simulations, this voltage metric was calculated at every 5 second interval between 10AM to 4PM. Figure 3.36 was provided as a means to easily inspect the TVD of Feeder 02 and 03 by presenting the daytime average TVD per penetration scenario. Again, the TVD decreased with increasing DER-PV capacity. Certain days experienced drastic changes in TVD, especially from DOY 45 to 48 on Feeder 03. The cause of this was determined to be that solar irradiance had a high CI, low VI, and contributed a significant portion of feeder load.



As presented in Eq. (4.14), TVD is time dependent and changes throughout the course of the day. Therefore, load movements and extreme variability injected from connected DER-PV facilities will be captured in this metric. For demonstration purposes, the TVD profile on Feeder 03 of DOY 45 was selected due to it experiencing maximum impact to average daily TVD. This profile is presented in Figure 4.37(a) with the associated head-of-feeder power measurements provided in (b). During the peak solar interval, the DER-PV connected at POI-1 resulted in a continuous reverse power flow situation with fluctuation in generation only occurring between the hours of 15 to 16. From these results, it can be concluded that the TVD metric accurately captures the voltage profile impact caused by variable DER-PV generation.

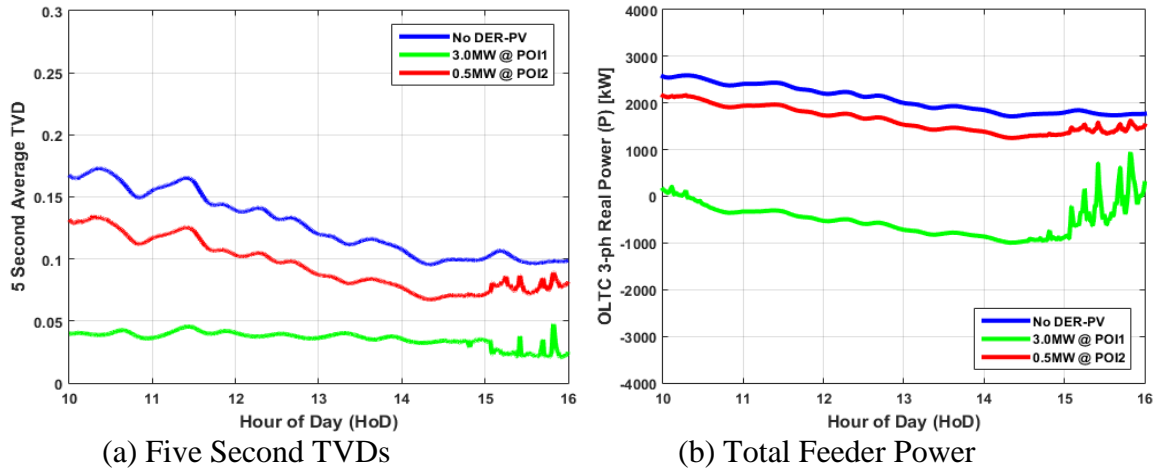


Figure 4.37: Maximum Impact to TVD on Feeder 03 (DOY=45)

To verify that the impact to TVD can be related to the magnitude and duration of solar generation, the Clear-sky Index (CI) and daily aggregate ramp rates (DARR) calculated from Site #4 historical measurements on a day basis throughout a year timespan were compared to the daily average TVDs on Feeder 03. The resulting TVD from the DER-PV deployments were subtracted from the TVD without DER generation

for easy interpretation. From referencing Figure 4.38(a), CI has a visible linear relationship with TVD difference when the generation did not cause reverse power flow (shown in red). On the other hand, the relationship between DARR and TVD difference was not significant, as depicted in Figure 3.38(b) in presenting a wide distribution spread.

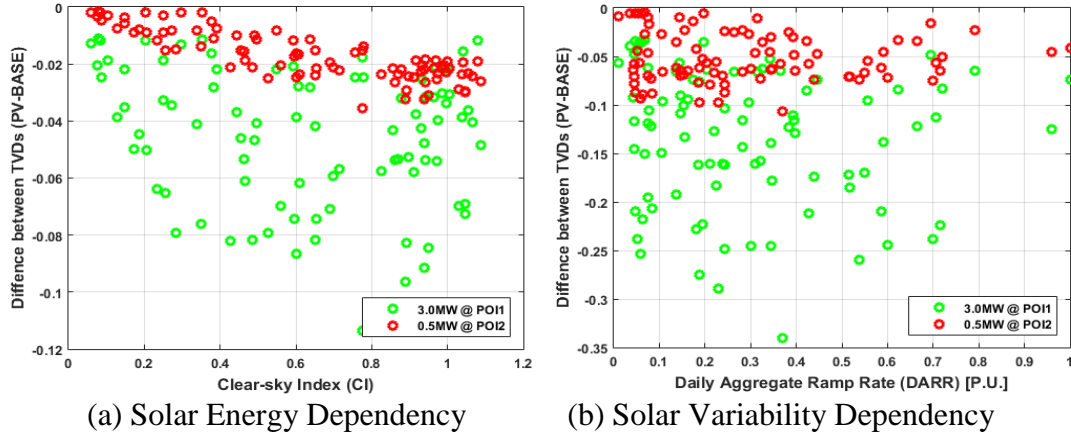


Figure 4.38: Feeder 03's Daily Average TVD Relationship CI & DARR

In conclusion, a simulation architecture utilizing OpenDSS was developed to provide an efficient and accurate method to model the highly variable DER-PV generation. An accurate representation of the voltage regulation relay was incorporated in this model to insure that the additional tap changes the feeder OLTC experience was accurate. Three month QSTS simulations were conducted on Feeder 02 and 03, with two unique deployments of centralized DER-PV facilities. To analyze the immense power flow results, metrics were introduced that can relate the solar irradiance profile (VI, CI, and DARR) to an overall impact to the feeder voltage profile (additional tap changes and TVD). With the pressing need to integrate renewable generation into distribution systems, DNOs will be required to utilize time series planning tools such as OpenDSS QSTS analysis to fully capture the impact to voltage regulation equipment operations.

CHAPTER FIVE

COORDINATED CONTROLLER BETWEEN VOLTAGE REGULATION DEVICES AND LARGE SCALE BESS ON UTILITY DISTRIBUTION SYSTEMS

5.1 The Need for a Distributed Energy Resource Management and Forecasting Controller

Today, fossil fuel is still the major source of energy in the world with electric utilities or independent system operators (ISOs) dispatching large, central power plants to balance system load via a transmission network. Due to the ever increasing world population and therefore demand for energy [40], a paradigm shift in human society's awareness of greenhouse gas emissions and climate change [41], and technological advancements in silicon voltage source converters (VSCs) [42]; renewable energy sources (RES) such as wind turbines and photovoltaic (PV) solar systems are predicted to become a significant proportion in the future electric power generation mix. In the United States, the California Independent System Operator (CAISO) experienced an exponential growth in RES capacity, especially in solar PV due to ideal climate conditions. With this, CAISO published a report in 2013 highlighting that if the increase in solar PV penetration continued its current trajectory, potential "overgeneration" can occur where RES generation exceeds more than what the system can handle, typically illustrated by the "duck chart" [43]. To avoid overgeneration, conventional dispatchable resources can be ramped down by the ISO to allowable levels. If this allowable minimum level is reached, the system will not have the ability to accommodate RES generation and the ISO will be forced to curtail renewable generation.

To avoid curtailment, a possible solution is to store excess generation at central power plants at key locations along the transmission system; and most advantageously, at various points throughout the distribution network [41]. Since utilities and ISOs do not have access to distributed energy resource solar PV (DER-PV) inverters, a plausible solution is to connect Battery Energy Storage Systems (BESS) along the distribution network. This will allow the operators to store excess energy production during the daylight hours and dispatch the stored energy at an ideal time. An example of a “duck chart” observed on a distribution feeder can be found in Figure 5.1. This illustrates the shift in load shape when the DER-PV penetration level increases on an individual distribution feeder. The overlaid BESS charge rate schedule illustrates how this solution if enacted on a substantial number of distribution feeders can help elevate the ISO’s system overgeneration risk in a distributed and controlled manner.

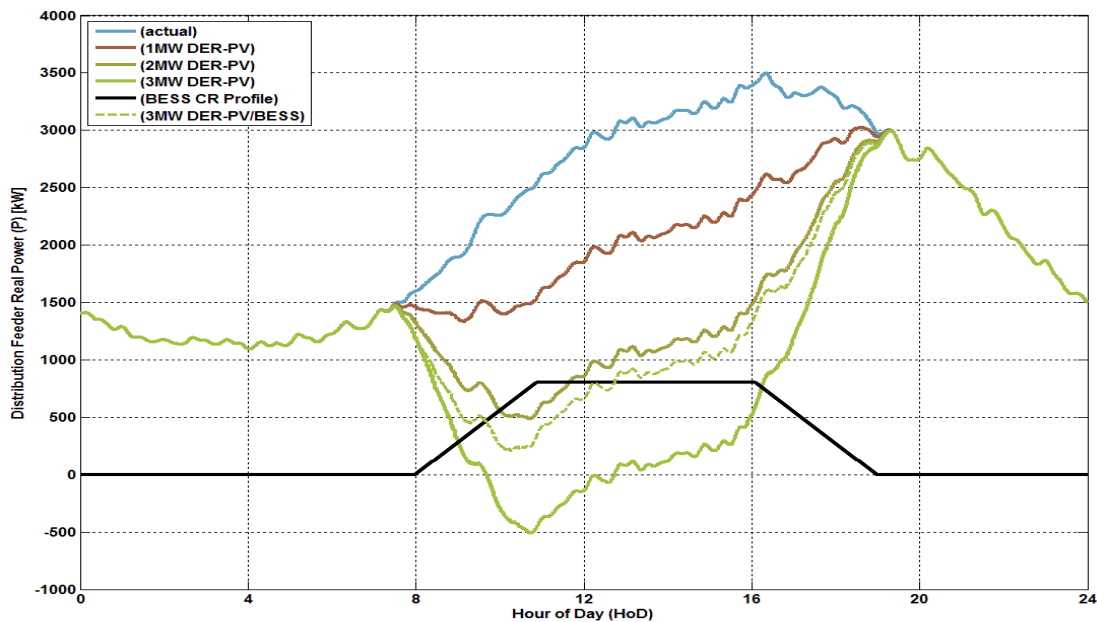


Figure 5.1: Duck Chart Example at the Distribution Feeder Level

Distribution Network Operator's (DNOs) standard practice for years was operating distribution systems with minimal monitoring and automation. Typically substation circuit breaker statuses are monitored at a high resolution (1-2seconds [22]) while substation analog measurements are monitored at a lower resolution (15seconds-15 minutes [22]). When a distribution system is strengthened with communication and control capabilities, it transitions to a smart grid [22]. Voltage regulation, mainly provided by transformer On-Load Tap Changers (OLTCs), line switch voltage regulators (SVRs), and shunt capacitors, traditionally operate autonomously based on local signals such as bus voltage [44]. Therefore, this is a non-coordinated approach where devices connected to the same distribution feeder are not communicating amongst each other.

This methodology served DNOs well for many years until the recently when there was a significant increase DER interconnections. When specifically focusing on DER-PV inverter based multi-megawatt facilities, the main operational challenge that arises for DNOs is the possibility of long term voltage rise and frequent highly variable voltage deviations [44]. Today, IEEE Standard 1547 restricts DER-PV inverters to participate in voltage/reactive power control [45]. Therefore, the inverters are set to only operate in power factor (PF) control mode with a set point extremely close to unity PF. On weak distribution systems, fixed PF control can have a negative effect on the Point of Interconnection (POI) voltage and therefore adversely impact system wide voltage [46]. With a high penetration of DER-PV on a distribution network that uses simply decentralized voltage regulation techniques, new issues can arise such as a temporary out-of-firm (OOF) voltage conditions resulting in a drastic increase of operations OLTCs

and/or SVRs will experience. Therefore, there is a need for DNOs to consider alternative methods which combine the existing distribution network devices with new digital control and sensing technologies. This method will shift the distribution system from its current passive form to an active network allowing new VSCs associated with DERs to participate in voltage regulation and respond quickly to prevent potential OOF operating conditions by compensating accordingly [47].

One method of interacting with traditional centralized OLTCs with inverter-based DER-PV generators in volt/VAR control has been proposed in [48] utilizing a discrete particle swarm optimization technique to determine future tap operations. Two inverter control strategies, fixed PF and fixed PF-fixed Q (where Q being dependent on the PV generation level), were compared to the IEEE 1547 constraint of minimal reactive power injection. A centralized coordination controller of distributed energy storage systems (DESS) was proposed in [49] with an objective to relieve the operational stresses on OLTC/SVR due to variable generation of DER-PV facilities as well as shave peak load. When the OLTC observes a voltage outside of the bandwidth, distress signals are sent to the coordination controller which in turn broadcasts charging commands to all DESS connected on the distribution feeder. This will mitigate reverse power flow and thus directly impacting head-of-feeder voltage.

Another method in mitigating voltage regulation issues and enable the accommodation of a larger penetration level of DER-PV, [46] proposed a peer-to-peer multiagent, or distributed control technique which enabled the DER-PV unit(s) to coordinate with the traditional utility regulation devices. In order for this distributed

control technique to work properly, new two-way communication avenues between all participating equipment is required. This can be accomplished via fiber optics, wireless, or power line communication (PLC). A PLC technique seems to be the most promising because of sufficient data transmission rates of around 500 kbps and is a very cost competitive option to implement since it exploits the existing power lines [46].

Input-Output logic was mapped to construct the LTC/SVR and distributed generation (DG) decision makers. The LTC/SVR inputs consisted of the voltage deviation between field measurements and the voltage setpoint, average predicted excessive tap operations, field agent propose messages, and field agent request messages. Each input scenario was mapped to corresponding outputs which included required tap position, an updated voltage set point, reply messages to other field agents, and a negotiation message amongst network field agents such as DG unit(s) [46].

The DG decision maker was constructed in a similar manner but with inputs such as the state of local voltage (if a violation is observed) and the current DG reactive power injection level set point. Additional inputs were included to facilitate two-way communication avenues between neighboring devices, accepting messages such as CFP, reply to proposals, and reply to requests. Outputs consisted of the DG's future real and reactive set points, the required inverter voltage set point, and purpose/request messages informing the network field agents of its change in operational state [46].

Having purpose, request, and negotiation messages being transmitted and received between all active voltage regulation devices enables coordination between all agents when responding to temporary OOF voltage conditions resulting from extreme

ramping events of DER-PV generation output. The downfall of this proposed multi-agent control is the assumption the DNO can control customer owned DER-PV inverters. Because of how current regulations and existing purchase power agreements (PPAs) were written, the DNOs do not have access to the facility's inverter controls. Therefore, an alternative technique is introduced where a utility-owned BESS is installed along the distribution feeder's main conductor upstream of a central DER-PV facility. Since the DNO owns the BESS, the converter can be externally controlled to participate in voltage regulation. Current efforts are underway to implement advanced distribution automation (ADA) which integrates sensing/monitoring, control, and protection to one master platform. With higher penetrations of DERs, Electric Vehicles, storage, and microgrids; a fourth generation Distribution Management System (DMS) is required by 2020 coined a distributed energy resource management system (DERMS) [50]. DERMS will enable coordination between ADA and DERs to optimize system performance and facilitate advanced management and forecasting control algorithms of DERs.

With a future DERMS in operation, a proposed DER management and forecasting control algorithm branded as a Master Energy Coordinator (MEC) can be implemented at the individual distribution substation level. Advanced two-way communication infrastructure is required where information will be passed between the distribution substation, the energy storage system, and any DER facilities. This will form what is commonly known as a Neighborhood Area Network (NAN) [22]. Field analog measurements such as single phase voltages, real through powers and reactive through powers are captured from the NAN and connected to individual Intelligent Electronic

Devices (IEDs) [22]. This information is passed through a Data Concentrator to the master substation computer which transmits up to the DMS. Afterward, this information is stored in a Supervisory Control and Data Acquisition (SCADA) historian database. The local DNO sponsoring this project requires an electronic recloser or automatic switch with communication capabilities to be placed directly before the point of interconnect (POI) with any DG facility over 1MW. Therefore, some SCADA data points are already available for integration into the MEC. Additional sensors will need to be installed to provide feedback on SC reactive power injection levels, OLTC/SVR tap positions, power injection levels at the BESS POI, and most importantly, a means of estimating the BESS's State-of-Charge (SoC).

The generation level of a DER-PV facility under a clear sky irradiance profile is very predictable in that the output will gradually increase as the day progresses, reaches a peak close to solar noon, and then gradually decreases until the sun passes Earth's observable horizon. To more effectively utilize a BESS to mitigate the negative impact from potential reverse power flow from a DER-PV facility on a distribution feeder, a charging strategy proposed in [51] suggests to have the BESS follow the same general profile; ramping-up the charge rate in the morning and ramping down the charge rate in the evening. Since the BESS has a limited amount of available energy capacity, it is important to use the asset wisely [51]. Preventing the BESS in charging too quickly before peak solar generation will ensure that there is enough capacity available to mitigate unacceptable reverse power flow and/or voltage levels. A charge rate schedule is

required to plan for this peak solar irradiance period as well as have the BESS fully charged before solar generation ceases.

On top of this functionality, the energy captured during the period of solar generation can be dispatched to provide energy during the peak hours of each day at the distribution substation level [52]. A Sodium-Sulphur BESS was selected for this project due to its high power, high energy density, minimal space footprint, and a fast response time (2 milliseconds). The battery cells were housed in a separate house within the distribution substation and the system was connected directly to the 11kV main bus. If a distribution substation has a small chance of exceeding OOF MVA ratings but has a large penetration of DER-PV on certain distribution feeders, a similar approach can be implemented where a smaller BESS can be connected to an individual feeder, upstream of a DER-PV facility. In this way, the battery system will be able to contribute to peak loading conditions and more effectively alleviate tap changers operational stresses.

5.2 A Novel Master Energy Coordinator Reliant on BESS and DER-PV Operation

The primary objective for the proposed Master Energy Coordinator (MEC) is to adapt the BESS controller's charging and discharging schedules so that the BESS will not be discharged to unnecessary levels. This will ensure the BESS is efficiency utilized and therefore directly extends the operational life of this asset. This centralized coordinator can be simply divided into three main functions, each contributing to proper coordination between voltage regulation devices and the BESS on a day-to-day basis. The primary function of the MEC (MEC-F1) is to adjust the charging schedule based on known solar irradiance profiles and the BESS's estimated Depth of Discharge (DoD) prior to a solar

generation period. The secondary function (MEC-F2) is to perform a day-ahead lookout at the forecasted load and estimate when this will occur. The results of this will drive the tertiary function (MEC-F3) of determining if the BESS peak shaving controller should be enabled during the given day of operation or hold the BESS in idling mode until the consecutive day's morning peak is projected to occur.

The first function of the MEC (MEC-F1) is driven from three inputs: the day-of-year's clear-sky irradiance (CSI) profile, the direct beam clear-sky irradiance (B_{ncl}) profile, and the present DoD during pre-daylight hours. In Figure 5.2, these inputs are highlighted in red. The CSI and B_{ncl} profiles are derived from the Ineichen & Perez corrected Kasten Model [37, 38]. This model is driven from DER-PV site location, site altitude, and derived solar azimuth and altitude angles. Details of the model formulation can be found in Chapter 4, Section 3.

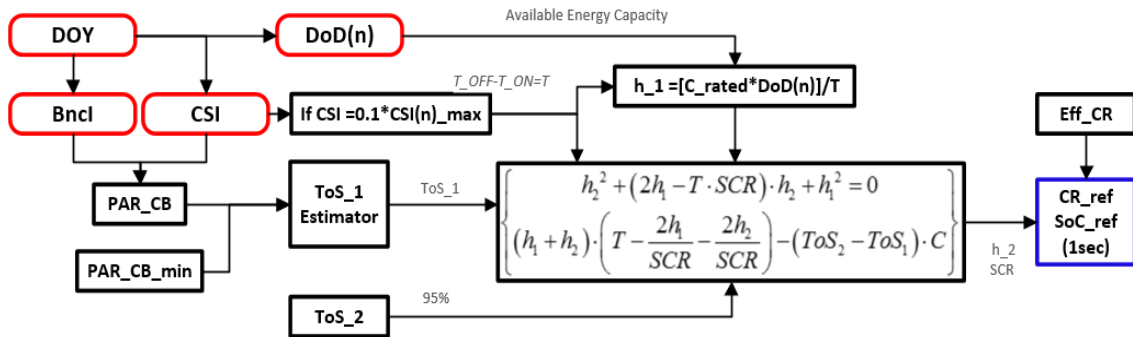


Figure 5.2: MEC-F1 Process Topology

The time at which the DER-PV will commence and cease generation (T_{ON} & T_{OFF}) can be estimated from referencing when the CSI profile intersects 10% of its peak. This 10% threshold can be tuned dependent on the DNO's preference. The concluded time instances formulate the extent of the BESS charging schedule (T) by

applying Eq. (5.1). When assuming a constant charging schedule, the charge rate (h_1) required to charge the BESS to 100% SoC can be found with Eq. (5.2). The initial DoD percentage, set by the peak shaving function, was referenced to calculate the useable energy capacity for the upcoming charging cycle.

$$T = T_{OFF} - T_{ON} \quad (5.1)$$

$$h_1 = \frac{C_{B, rated} \cdot DoD(n)}{T} \quad (5.2)$$

Altering the constant charge rate (CR) profile to one that better aligns with solar PV generation, the charging rate will increase from zero at the start of the period T , when the battery is at its maximum DoD for that specific day, at a slope of charging rate (SCR) until the first SoC threshold is met (ToS_1). Then, the CR saturates at a constant value until the second SoC threshold is met (ToS_2). The CR then decreases at the same SCR until reaching the end of the scheduled charging period. Eq. (5.3) can be used to enforce this construction methodology with a visual depiction presented in Figure 5.3. [51]

$$CR_r(t) = \begin{cases} CR_r(t-1) + SCR \cdot \Delta t^{-1} & \text{if } t_{ON} \cdot \Delta t < t < t_2 \cdot \Delta t \\ h_1 + h_2 & \text{if } t_2 \cdot \Delta t < t < t_3 \cdot \Delta t \\ CR_r(t-1) - SCR \cdot \Delta t^{-1} & \text{if } t_3 \cdot \Delta t < t < t_{OFF} \cdot \Delta t \\ 0 & \text{for all else} \end{cases} \quad (5.3)$$

Where:

$$t_2 = \left(T_{ON} + \frac{h_1 + h_2}{SCR} \right), t_3 = T_{OFF} + \frac{h_1 + h_2}{-SCR}, \text{ and } \Delta t = 3600\text{sec}$$

Inputs that can be pre-defined to this methodology include: t_{ON} , t_{OFF} , ToS_1 , ToS_2 , and most importantly h_1 . Referencing Figure 5.3, in order to adjust the CR schedule to a

new shape, the blue and red areas (representing energy in kWh) are required to be held equal to ensure that the BESS has a 100% SOC at the end of the charging period.

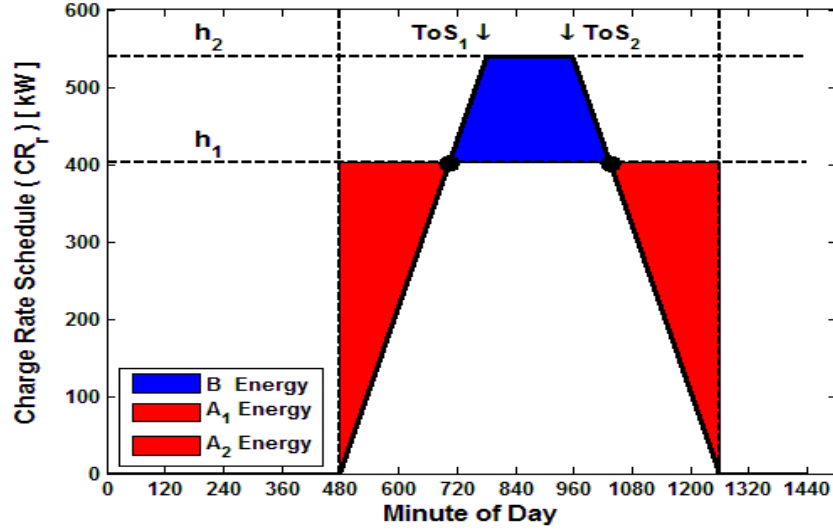


Figure 5.3: Methodology in Obtaining BESS Charge Rate Schedule

As presented in [51], a simultaneous solve of Equations (5.4 & 5.5) representing these two areas is conducted to arrive at the SCR and h_2 required to ensure 100% SoC. The resulting SoC reference profile can now be determined by applying Eq. (5.6), referencing the CR reference profile (CR_r) and BESS characteristics including energy capacity ($C_{B, rated}$) and charging efficiency (η_{CH}).

$$h_2^2 + (2 \cdot h_1 - T \cdot SCR) \cdot h_2 + h_1^2 = 0 \quad (5.4)$$

$$(h_1 + h_2) \cdot \left(T - \frac{2 \cdot h_1}{SCR} - \frac{2 \cdot h_2}{SCR} \right) - (ToS_2 + ToS_1) \cdot C_{B, rated} = 0 \quad (5.5)$$

$$SOC_r(t) = \frac{SOC_r(t-1) \cdot C_{B, rated} + \eta_{CH} \cdot CR_r(t) \Delta t^{-1}}{C_{B, rated}} \quad (5.6)$$

Inspecting Eq.'s (5.4 & 5.5), the only remaining inputs to construct the CR schedule profile are two SoC thresholds (ToS_1 & ToS_2). By procuring 5% of the

available energy capacity for the CR down-ramping period, ToS_2 is held constant at 95%. By doing this, the shape of the CR profile is solely dependent on ToS_1 . During the summer months, it is more probable that a DER-PV facility will generate for a longer extent of time. Therefore, the SoC threshold (ToS_1) to transition from a positive slope to a slope of zero can be tuned to this known fact. A larger ToS_1 will result in a smaller SCR and therefore a shorter time span when the CR is held constant but overall maximizing the CR real power magnitude (in kW).

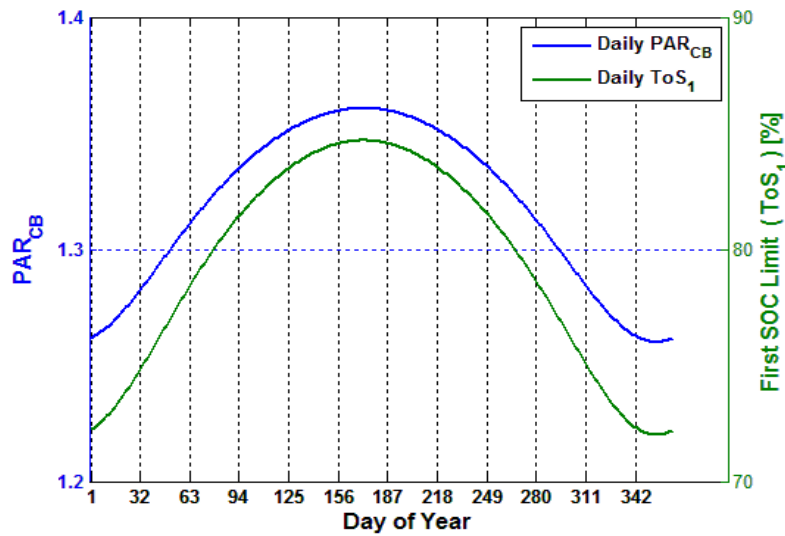


Figure 5.4: Projection of PAR_{CB} and Resulting SoC Limit

To arrive at a desired SOC threshold, a discovered relationship between the CSI's and B_{ncl} 's peak to average ratio (PAR) is utilized. After applying Eq. (5.7) on a daily basis throughout the 2014 year with the results shown above in Figure 5.4, the ratio between daily CSI and B_{ncl} 's PAR (PAR_{CB} & PAR_{BN}) had a maximum of 1.361 during the summer solstice and a minimum of 1.260 ($PAR_{CB,min}$) during the winter solstice.

$$PAR_{CB} = \frac{PAR_{CB}}{PAR_{BN}} = \frac{\frac{\max(CSI)}{\max(BncI)}}{\frac{\max(CSI)}{\max(BncI)}} \quad (5.7)$$

It was essential that PAR_{CB} had this relationship because it enabled a means for ToS_1 to be adaptive on a day-to-day basis. PAR_{CB} was converted to ToS_1 via Eq. (5.8). This was done by normalizing the PAR_{CB} profile with a base of $PAR_{CB,min}$ and then being positively offset by $ToS_{1,min}$. To ensure the target threshold never violates the maximum DoD of the BESS, Eq. (5.9) was used to derive $ToS_{1,min}$.

$$ToS_1 = ToS_{1,min} + (PAR_{CB} - PAR_{CB,min}) \cdot PAR_{CB,min} \quad (5.8)$$

$$ToS_{1,min} = (1 - DoD_{max}) \cdot (1 + (1 - \eta_{CH})) \quad (5.9)$$

To test the functionality of MEC-F1, the winter and summer solar solstice (12/21 and 6/21) associated clear-sky irradiance profiles were selected and shown below in Figure 5.5. From inspection, a major shift in the magnitude and timespan is observed with 6/21 offering approximately double the solar energy compared to 12/21.

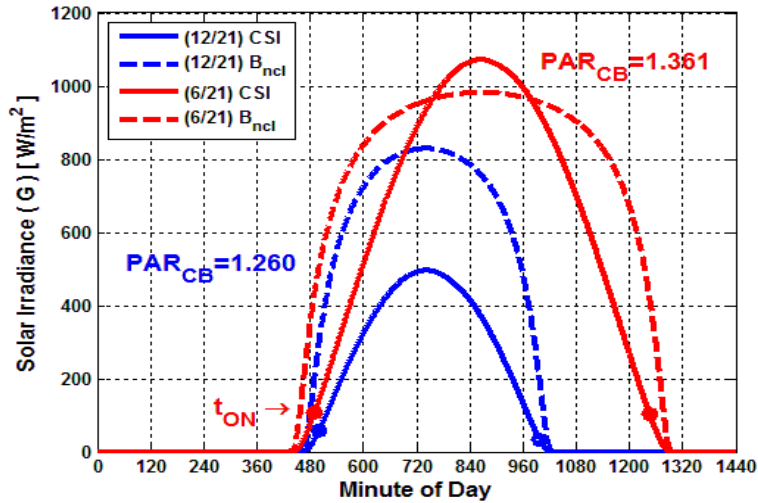


Figure 5.5: Winter and Summer Solstice CSI and B_{ncl} Profiles

For illustration purposes, a BESS was selected with a 1000kW maximum power rating, a total energy capacity of 12,121kWh, and a DoD_{\max} of 33%. Two scenarios were created per selected day by setting the initial DoD before the solar generation window to 100% and 50% of the DoD_{\max} . These BESS characteristics along with derived solar CSI and B_{ncl} profiles associated Site #4 introduced in Chapter 4 Section 3, were inputted into the MEC-F1 (Figure 5.2). The resulting charge rate and state of charge schedules are provided below in Figure 5.6 (a) and (b) respectively.

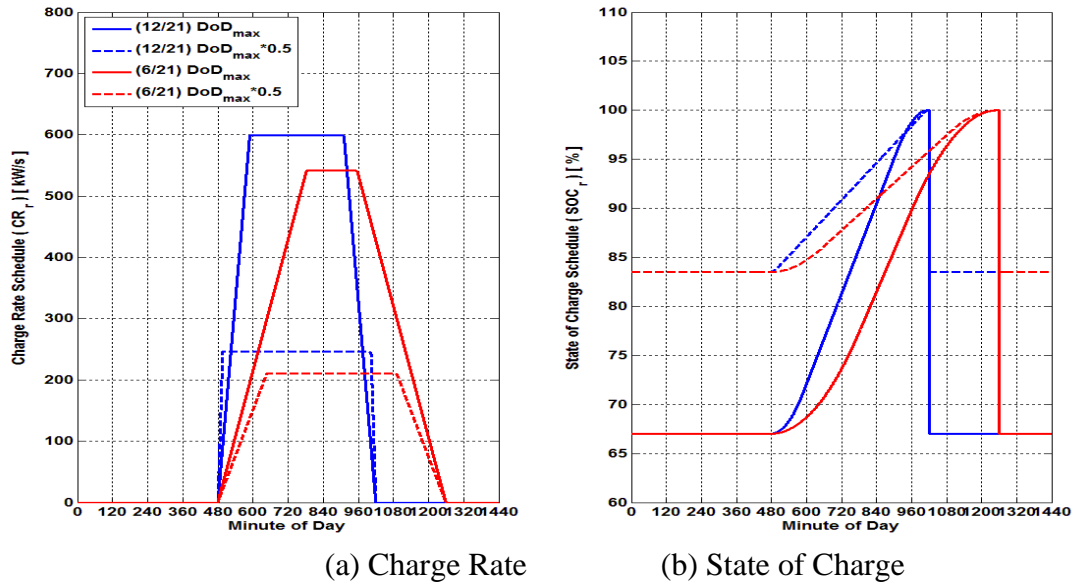


Figure 5.6: BESS Operation Schedule during Solar Generation Window

With a higher initial DoD, the overall CR profile decreases to a lower magnitude translating into there being less energy capacity available for the BESS to charge during the solar generation window. It is important to note that the BESS charging controller will adapt to the variable nature of DER-PV, therefore the SoC will deviate away from the schedule. The final SoC may not reach 100% especially during low irradiance days when the initial DoD was set too high. Therefore, additional forecasting needs to take

place where the DER-PV's daily energy production is estimated based off of historical data and next-day VI and CI coefficients. This will ensure the available energy capacity is fully utilized. MEC-F2 accomplishes this task by concluding and enforcing a DoD target during the BESS's discharging mode of operation.

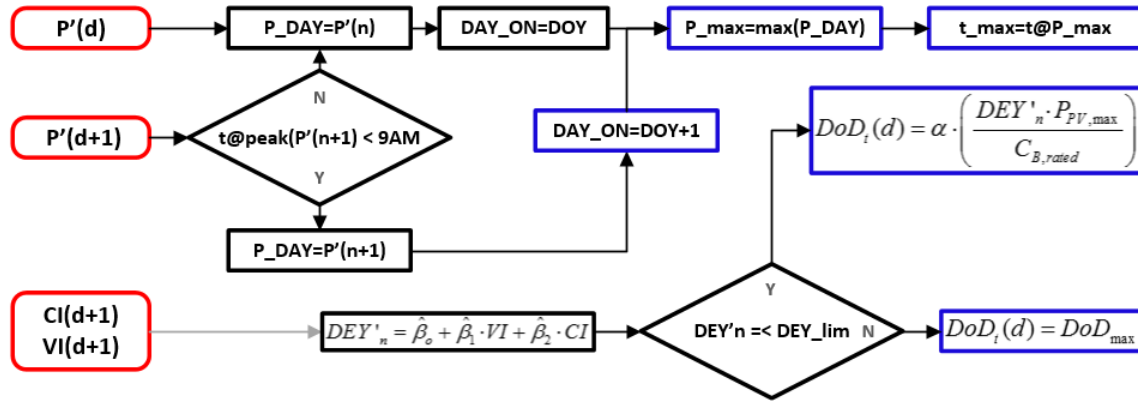


Figure 5.7: MEC-F2 Process Topology

The overall processing scheme of the MEC's secondary function (MEC-F2) is presented in Figure 5.7. This function is responsible for peak load projections and setting the BESS discharge mode's target depth of discharge (DoD_t). The initial process consists in estimating the daily maximum load and associated time instance using projected load profiles of the present and subsequent day. If the next day's peak load time was before 9AM, then the MEC-F2 would generate a flag and transmit it to the connected BESS to prevent discharging until the next day. This coordination will ensure the BESS will be used when it is needed most, making its operation more cost effective. If this was not the case, the MEC-F2 would enter normal operation in which the second process would estimate the DoD_t and require the BESS controller to not exceed this limit during its peak shaving discharge mode. To avoid unnecessary wear and tear on the BESS from

discharging constantly to its maximum DoD, the target DoD was set to a function on an estimate of the upcoming day's solar generation daily energy yield (DEY).

$$DEY = \sum_{t=1}^{1440} DEY + P(t)_{PV} \cdot 60^{-1} \quad (5.10)$$

$$DEY_n = \frac{DEY}{P_{PV, \max}} \quad (5.11)$$

To form this estimate, a linear regression model was constructed with historical variability index (VI) and clear-sky index (CI) as the independent variables and a normalized DEY (DEY_n) as the dependent variable. Utilizing annual historical DER-PV plant data, Eq.'s (5.10 & 5.11) were applied to calculate DEY_n on a daily with units of per-unit-hours (p.u.h.). The relationships between these independent variables and recorded daily energy yields associated with Site #4 are presented in Figure 5.8.

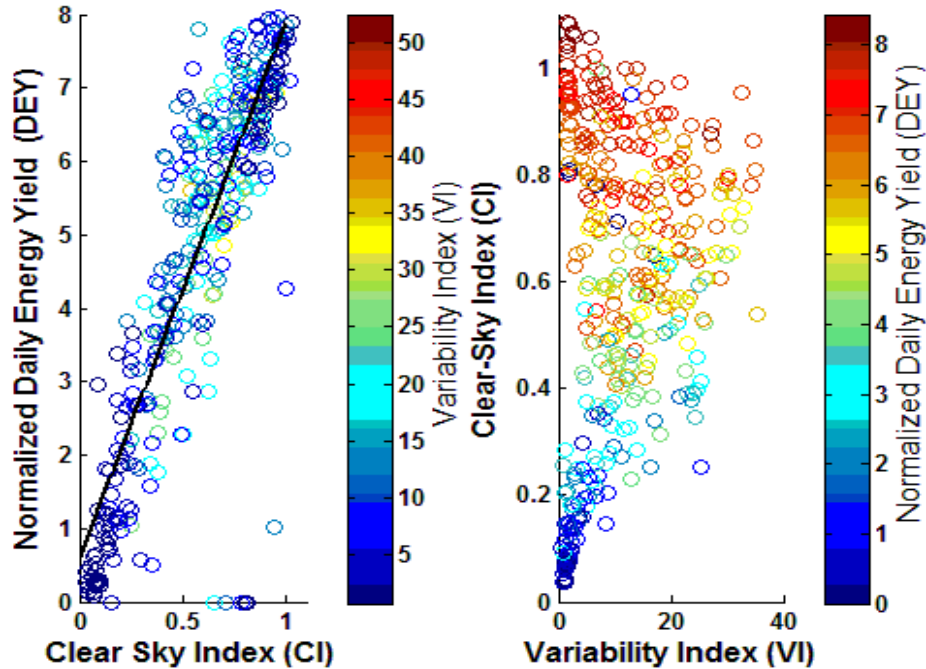


Figure 5.8: Relationship between Solar Coefficients and Observed DER-PV Normalized Daily Energy Yield

Observe how CI has a very linear relationship with the DEY_n while VI imposes an expansion of DEY_n . From this, it was concluded that the VI and CI solar coefficients are possibly statistically significant in the magnitude of observed DER-PV energy production. A linear regression model, as proposed in Eq. (5.12), was constructed based on a random selection of 90% of available daily historical DEY_n , VI, and CI. A least squares regression analysis was conducted on this selected training dataset in order to arrive at the linear model's coefficients ($\hat{\beta}_i$). The resulting coefficient values are shown in Table 5.1 with individual p-values signifying if a coefficient is statistically significant.

$$DEY'_n = \hat{\beta}_o + \hat{\beta}_1 \cdot VI + \hat{\beta}_2 \cdot CI \quad (5.12)$$

The p-value of VI signifies that it possibly insignificant in predicting the DEY_n due to it being slightly greater than the typical level of significance of 0.05. Because of the known fact that the variability of solar irradiance significantly impacts the generation profile of a DER-PV facility, VI was kept in the model. The overall R^2 of this regression model was found to be 0.8042 with residual standard error of 1.036p.u.h. From these metrics, it can be concluded that this model is sufficiently accurate in predicting the highly variable and chaotic daily DER-PV electric generation yield.

Table 5.1: Linear Regression Results

Coefficient	Value	S.E.	t-value	Pr(> t)
$\hat{\beta}_o$	0.4519	0.1427	3.167	0.00169
$\hat{\beta}_1$	0.0135	0.0069	1.954	0.05153
$\hat{\beta}_2$	7.2859	0.2101	34.67	<2e-16

To convert the estimated DEY_n (DEY'_n) to a target DoD for the peak shaving controller, a peicewise linear function is implemented, as shown in Eq. (5.13). This

function is dependent on the BESS energy capacity ($C_{B, \text{rated}}$), the BESS maximum depth of discharge (DoD_{max}), and the size of the DER-PV facility ($P_{PV, \text{rated}}$). Since the BESS has a limited available energy capacity, a factor (α) was calculated by Eq. (5.14) which references an annual average of observed DEY ($\overline{\text{DEY}}$). The MEC-F3 piecewise function enforces a DEY' limit found by Eq. (5.15). This will ensure that the DoD'_t will always be less than the DoD maximum during projected below average solar generation days.

$$\text{DoD}_t = \begin{cases} \alpha \cdot \left(\frac{\text{DEY}'_n \cdot P_{PV, \text{max}}}{C_{B, \text{rated}}} \right) & \text{if : } \text{DEY}'_n \leq \text{DEY}_\alpha \\ (\text{DoD}_{\text{max}}) & \text{if : } \text{DEY}'_n > \text{DEY}_\alpha \end{cases} \quad (5.13)$$

$$\alpha = \frac{C_{B, \text{rated}}}{\overline{\text{DEY}} \cdot P_{PV, \text{max}}} \quad (5.14)$$

Where:

$$\text{DEY}_\alpha = \frac{\text{DoD}_{\text{max}} \cdot C_{B, \text{rated}}}{\alpha \cdot P_{PV, \text{max}}} \quad (5.15)$$

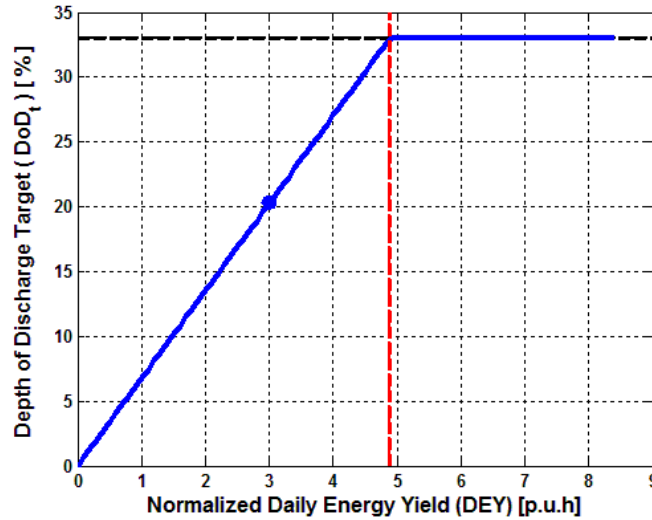


Figure 5.9: MEC-F2 Formulation of Target DoD Enforced during Peak Shaving

To show the functionality of the MEC-F2, if the same BESS previously described is connected to a distribution feeder with the presence of a 3MW DER-PV facility, the α would equal 0.2739. When referencing Site #4's historical plant measurements for the annual average DEY, the DEY_{α} would equal 4.8857 p.u.h. The resulting piecewise function responsible in concluding the DoD target is shown above in Figure 5.9. The dashed red line represents the calculated DEY_{α} . If MEC-F2, process 2 predicts a DEY of 3 p.u.h, the target DoD enforced on the BESS peak shaving controller would be 20.3% (shown as a blue datapoint).

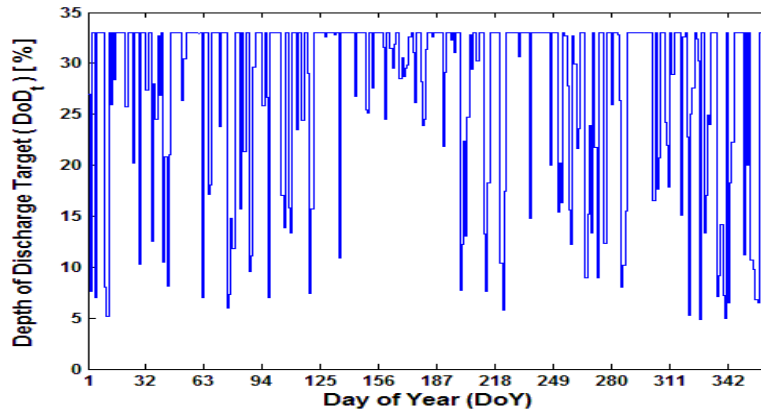


Figure 5.10: Resulting Target DoD from a Static Annual Simulation of MEC-F2

The results of a static annual simulation of MEC-F2 assuming an initial 100% SoC at each dispatch cycle is presented in Figure 5.10. Note how the maximum DoD was reached more frequently during the summer months and landed extremely low target points during the early winter months. This result illustrates that the MEC-F2 has builtin processes and models to predict when the distribution feeder will experience its daily peak load and the ideal level of BESS discharge in preparation for the coming day's DER-PV electric generation production.

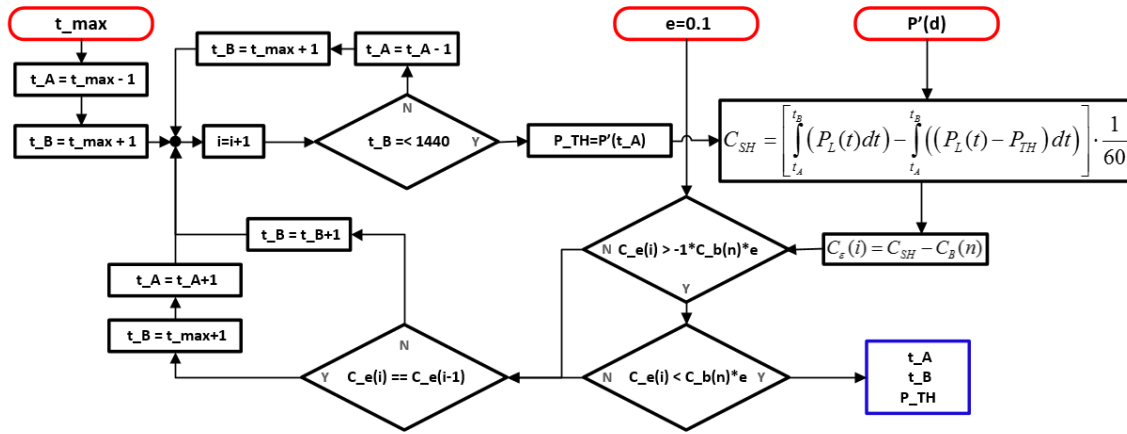


Figure 5.11: MEC-F3 Process Topology

The Master Energy Coordinator third function's (MEC-F3) goal is to estimate when the BESS peak controller should be enabled and the power threshold it should enforce. This function accepts three inputs: the time of the upcoming peak load (t_{\max}) provided by MEC-F2, the projected distribution feeder load shape, and an error threshold (e) set to 0.1 or 10% of energy available. The overall process topology can be viewed in Figure 5.11. MEC-F3 iteratively solves for the power threshold (P_{TH}) necessary for peak load coverage and expenditure of all available energy (E_B), determined by Eq. (5.16).

$$E_B(n) = SOC_B(n) \cdot C_{B, rated} \cdot DoD_t(n) \quad (5.16)$$

The overall algorithm consists of first obtaining the power magnitude ($P'(t_A)$) at the peak loading period start time (t_A). Then, the end time (t_B) is increased at a 1 minute interval until either the projected difference in energy is within 10% of the available BESS energy or that the previous error is equal to the present error. In the later event, t_B is reset and t_A is moved back in time to arrive at a new power threshold. During the case when t_{\max} is less than 540min (9AM) and t_B is greater than 630min (10:30am), the end

time instead is reset. Having this logic implemented prevents an overlap between the discharge and charging period of the BESS. The MEC-F3 algorithm continues until the projected expended energy is within 10% of the known available stored energy.

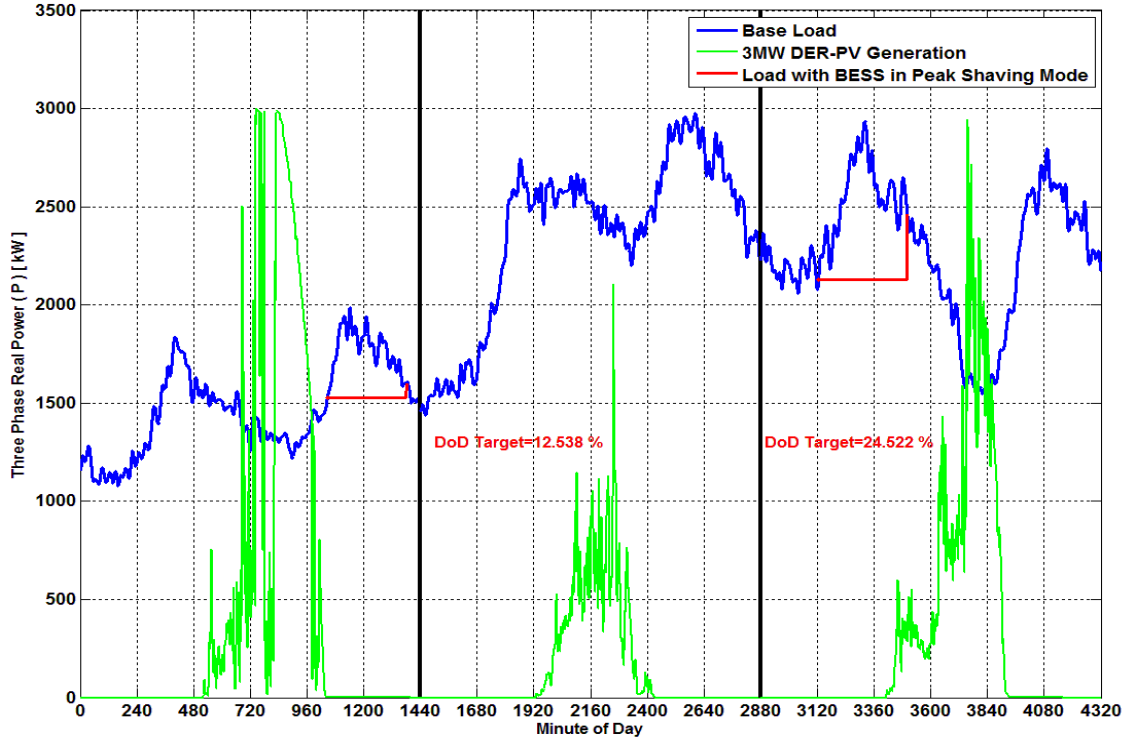
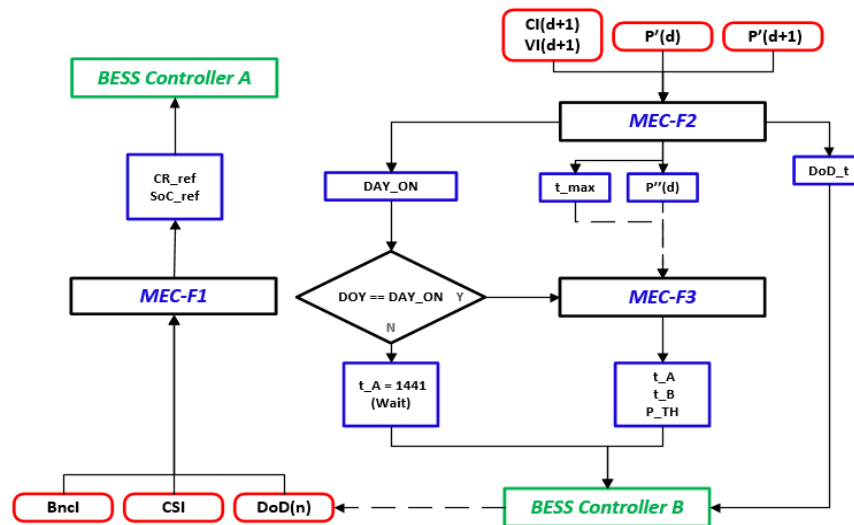


Figure 5.12: A Three Day Snapshot (2/3 – 2/5) for Testing the MEC's Functionality

For an example of the overall coordination between MEC-F2 and MEC-F3, a three day snapshot was obtained of Feeder 03 load and output from a connected 3MW DER-PV facility. During day #1, MEC-F2 projected an evening peak during day #2. Therefore, the peak shaving controller was enabled and MEC-F3 selected t_A and P_{TH} . MEC-F2 also projected DER-PV to be generating below average during day #2. Therefore, the target DoD was set to 12.548%. Proceeding to day #3, MEC-F2 projected a morning peak occurring. Therefore, the stored energy was held during the day #2's

evening peak. The target DoD for day #3 peak shaving was almost doubled due to MEC-F2 predicting an increase in the daily DER-PV generation. The generation profiles shown in green confirm this prediction.



5.3 Distribution Equipment Controllers under the Master Energy Coordinator

Communication between voltage regulation equipment and the master distribution substation computer is essential in order to implement the proposed MEC. Therefore, it was assumed two-way communication infrastructure is in place from the substation to the feeder's on-load tap chargers (OLTCs), Switch Capacitors (SCs), and most importantly connected BESS. The overall communication network topology is displayed in Figure 5.14 with OpenDSS [20] as the power flow simulator. Since only necessary field equipment measurement points were pulled over the COM interface during the one second time step Quasi Static Time Series simulation, the capabilities of a modern DSCADA communication system were properly modeled.

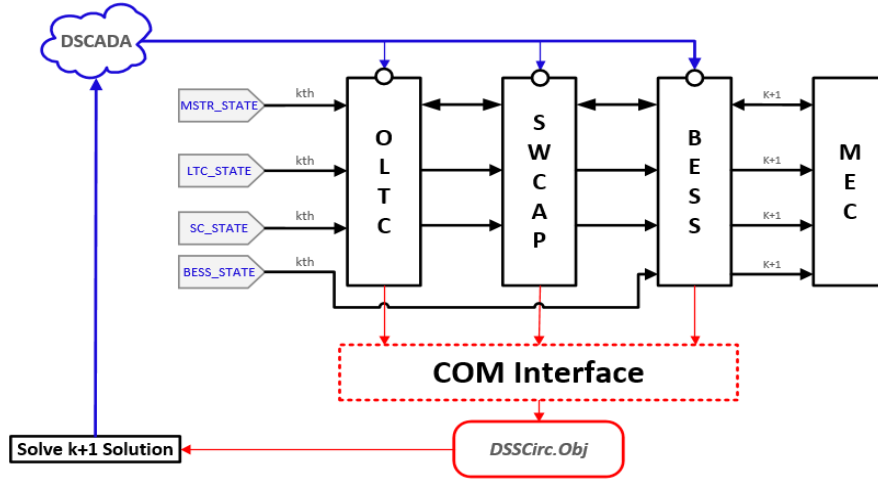


Figure 5.14: Communication Architecture of Incorporating a MEC and BESS

Custom controllers are modelled for existing OLTCs and SC banks with the control logic presented in Figures 5.15 and 5.16 respectively. The OLTC controller was set to sequential mode [31] while the SC controller is set to reactive power mode. Each of these field agent controllers transmitted indicator variables as presented in Table 5.2 to the

master substation computer where the MEC would interpret the feedback of the current and any requests to change states. The OLTC and SC controllers incorporate a coordination flag (F_CAP_CL), as shown in red, to signify if the shunt capacitor can be used to compensate an observed OLTC control voltage violation. For example, if the OLTC experiences a low voltage event (LV=1) and the switched capacitor is current de-energized, a F_CAP_CL=1 would transmit to the master substation computer. If accepted by the MEC, this override command to energize would be transmitted to the SC even if the observed reactive power is not above the set threshold.

Table 5.2: Input Output Data Point Tags of an OLTC & SC Controller

OLTC Controller I/O		Switch Cap Controller I/O	
VIO_LTC_TIME	Recorded time of voltage violation	VIO_CAP_TIME	Recorded time of kVAR violation
SVR_TMR	Internal VR Relay Timer	SC_TMR	Internal SC Relay Timer
HV	Boolean if VRR Requests a Buck Op.	SC_CL	Boolean if Relay Requests an Close Op.
LV	Boolean if VRR Requests a Buck Op.	SC_OP	Boolean if Relay Requests an Open Op.

Other conflicts can arise between the OLTC and SC such as when both timers are coincidentally incrementing to change states. During such an event, the MEC will send an override command to each field agent, resetting the timers and immediately altering the state of one piece of equipment. Having the ability to reset voltage regulation equipment relay timers is especially important when incorporating the BESS controller because this can provide additional time for the BESS to respond to HV/LV events and ramp up/down its present charge rate (CR) or discharge (DR) in attempts to bring the head-of-feeder voltage back within the desired bandwidth.

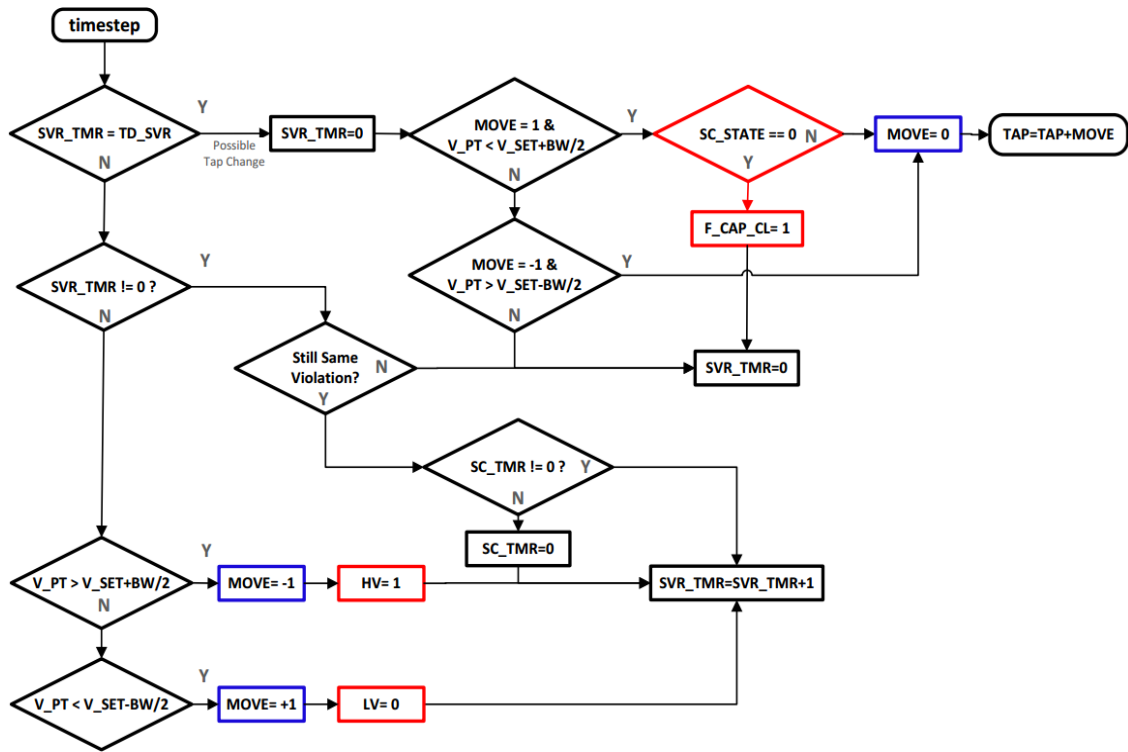


Figure 5.15: Feeder On-Load Tap Changer Time Sequential Controller

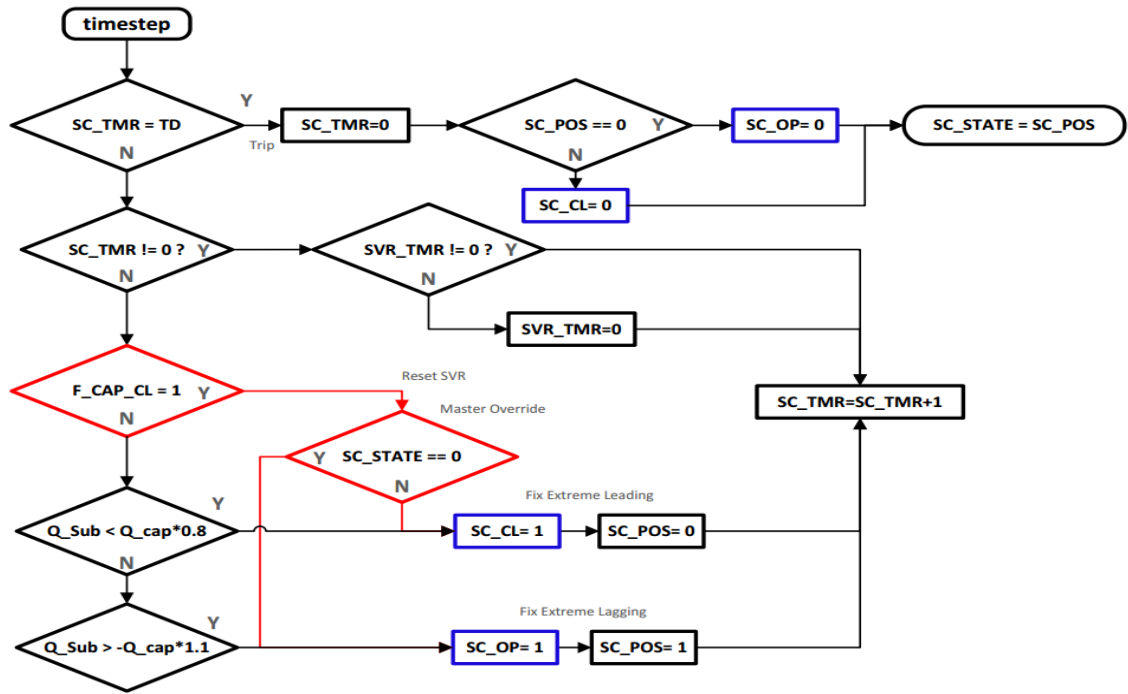


Figure 5.16: Switch Capacitor Reactive Power Controller

The responsibility of the BESS Controller is to dispatch the battery's charging and discharging rates according to the current operational state of the distribution feeder. This controller can be divided into three main functions. The primary function of the BESS is to mitigate long term reverse power flow introduced by a DER-PV facility located downstream by following a charge rate schedule (produced by MEC-F1) that closely aligns to a clear-sky irradiance profile. The secondary function is to respond to extreme short term DER-PV generation deviations, damping the feeder's power derivative by either providing power during a loss-of-generation event or consuming power during a fast gain-of-generation event. The third function is to implement peak shaving operation during a desired time and at a certain feeder load threshold, both provided by MEC-F3. The first two functions are incorporated into 'Controller A' and the third function is incorporated into 'Controller B' as depicted in Figure 5.17. These two controllers are only enabled during the desired times, either when the DER-PV facility is generating above a certain threshold or that the time of operation is with the peak shaving window.

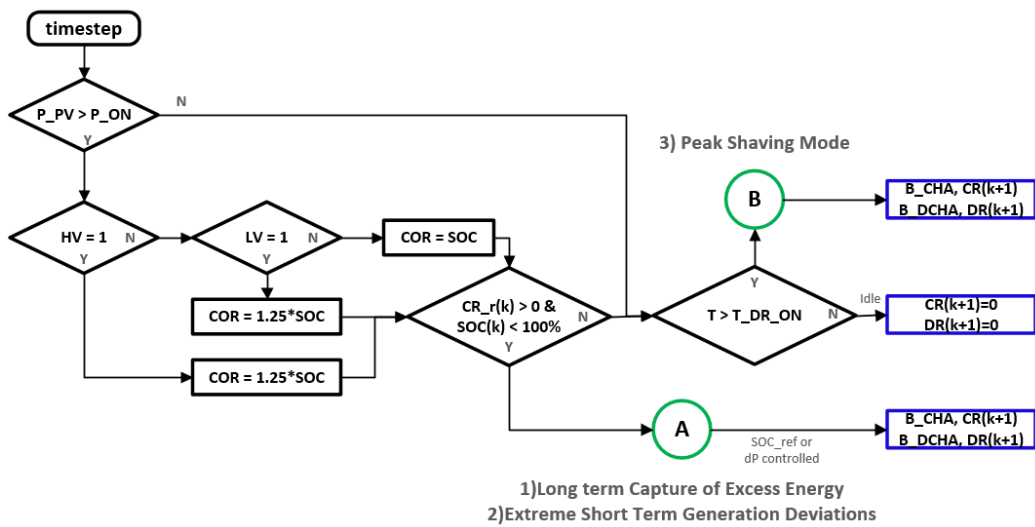


Figure 5.17: BESS Controller Logic & Topology

The overall BESS controller adapts to select feedback from the field including the DER-PV POI real power measurements and the head-of-feeder OLTC Boolean flags signifying if a high voltage or low voltage event is being experienced. The CR or temporary DR during DER-PV operation can be amplified by a factor labelled COR or the change of rate. If the OLTC is experiencing a violation, the BESS controller defines the COR gain to 125% greater than the normal level. The larger this gain increase, the quicker the BESS will respond to an OLTC voltage violation event. The COR factor is then passes into Controller A's logic, as shown in Figure 5.19. A1 and A2 gains (shown in green) are then directly altered to implement the desired response of the CR or DR. The controller dispatches a new CR/DR command every 5 seconds and quickly responds to strictly one of three major operational cases previously discussed.

Experiencing extreme deviations in DER-PV output is a widely known fact in the power systems industry and can drastically impact the operation of voltage regulation equipment. Hence, the first operational case was positioned as priority. The BESS Controller 'A' accepts field measurements from the DER-PV facility and internally calculates Eq. (5.17) to obtain the power deviation at each dispatch interval or $k = 5\text{sec}$.

$$dP_{PV}(k) = P_{PV}(k) - P_{PV}(k-1) \quad (5.17)$$

A predefined deviation threshold (P_{TH}) was selected to be 0.01 kW/5sec based on analyzing Site #6's historical plant output. Each day was classified by its VI and CI according to Sandia National Laboratory's Classification Scheme [18]. Figure 5.18 presents a selected day from each category to display the difference between observed $dP_{PV}(k)$ magnitudes and regularity. When enforcing a P_{TH} of 0.01kW/5sec, Site #6's

power deviations would only cause a violation 2% of the total amount of 5 second intervals when the DER-PV facility could possibly generate. This translates into approximately 101 hours throughout a year of operation in which the BESS controller will experience a power deviation violation. Therefore, this threshold was deemed appropriate due to the BESS now only responding to extreme cases. Note that P_{TH} will require tuning if the controller is applied to a different facility because power deviations can depend on the system's size, orientation, configuration, and location.

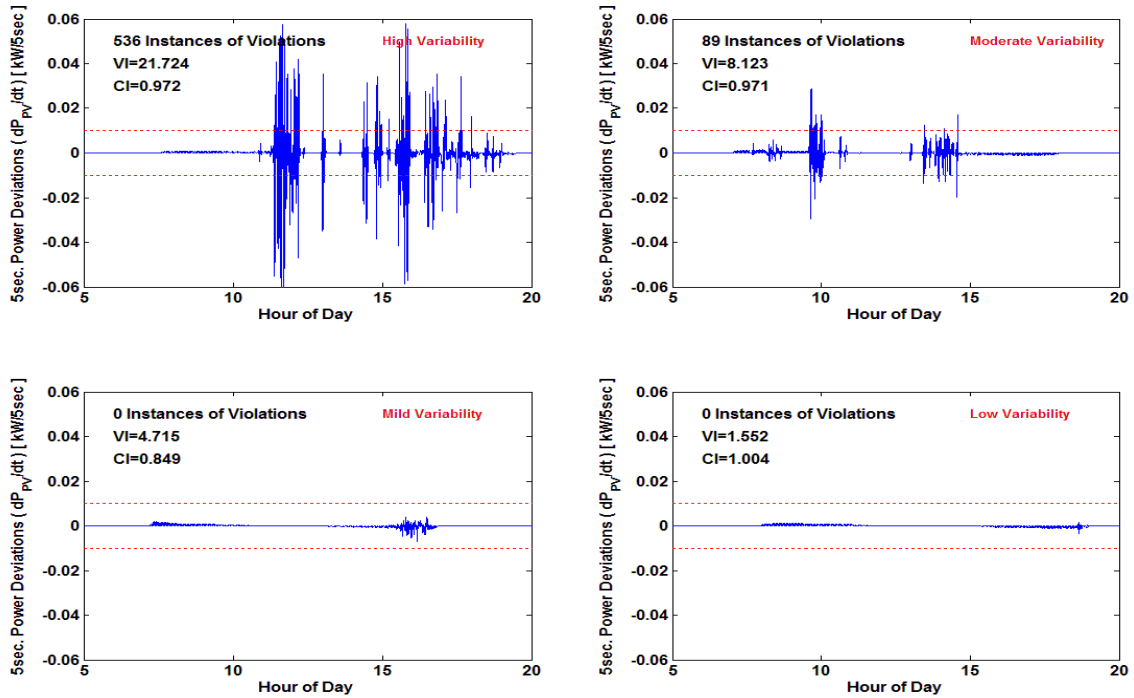


Figure 5.18: Four Daily Samples of DER-PV Five Second Real Power Derivatives

In the event that an observed derivative is negative and less than $-P_{TH}$, then it can safely be assumed the DER-PV facility is experiencing an extreme decrease in generation. Acceleration gains (A1 or A2) are applied to the observed PV derivative and either added to $CR(k)$ or subtracted from $DR(k)$ as shown in Eq. (5.18). If this event

extends for a long period of time, then there is a chance the controller will switch to short term discharging mode [51] where the BESS becomes a generator and injects power. Once the DER-PV's generation begins to ramp up, the observed PV derivative changes to a positive value. In this situation, the same acceleration gains will be used except opposite in sign. If the BESS is in discharging mode during this event, Eq. (5.19) is applied to gradually decrease the magnitude of the DR. If the next dispatched DR is determined to be less than zero, then the BESS reverses to charging mode and sets the CR equal to the recently determined DR, thus consuming power again.

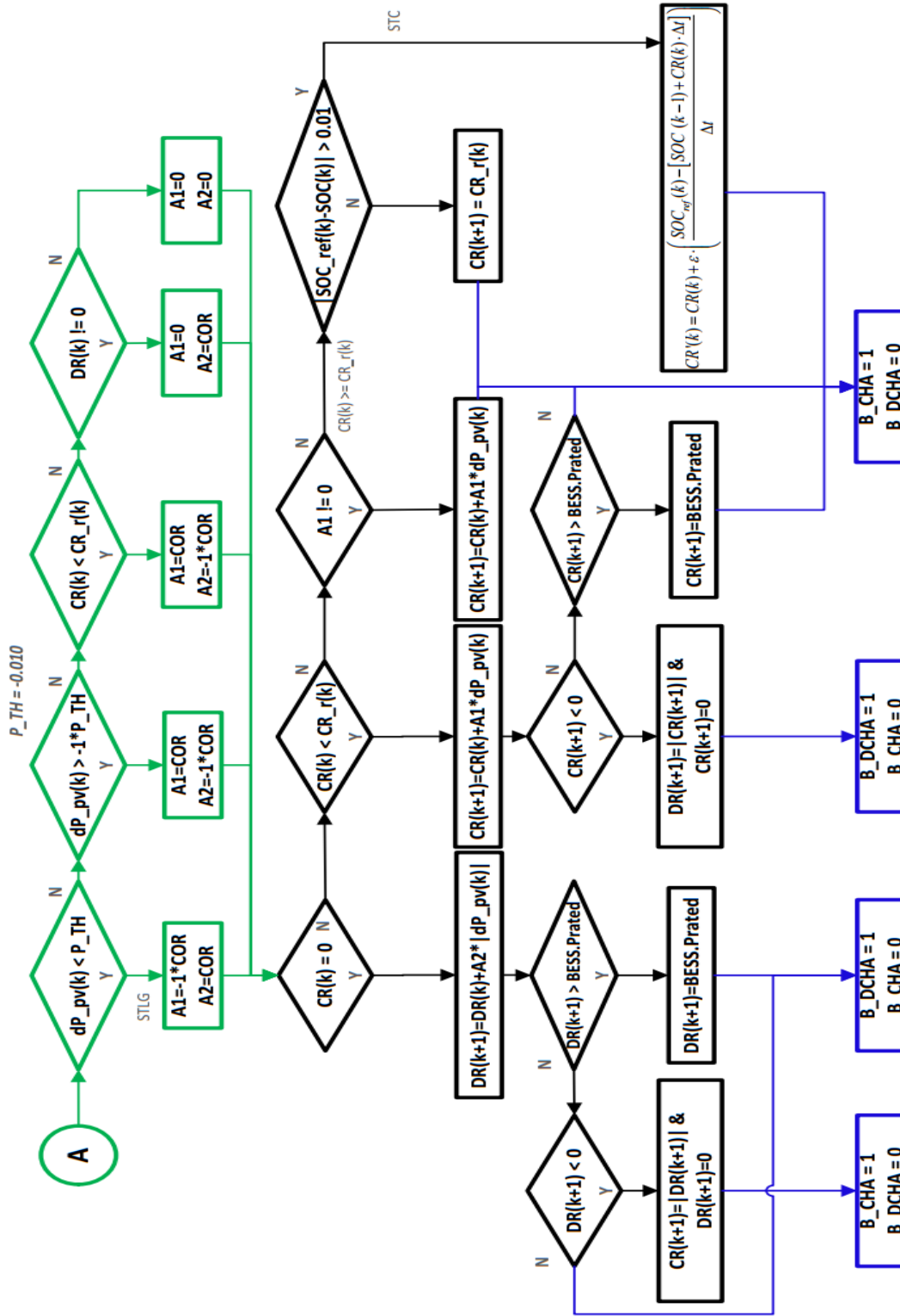
$$CR(k+1) = CR(k) + A1 \cdot |dP_{pv}(k)| \quad (5.18)$$

$$DR(k+1) = DR(k) + A2 \cdot |dP_{pv}(k)| \quad (5.19)$$

Onto the second situation when the DER-PV power deviation does not violate the threshold and the estimated SoC of the BESS is below the scheduled value, the scheduled CR will be adjusted by a factor determined by Eq. (5.20) [51]. This will continue until the SoC is again within 1% of the scheduled level. During extremely variable days, a situation can arise when the required CR to bring the battery's SoC back up to the schedule surpasses the rating of the BESS. Therefore, a limiter is enforced so that the CR saturates at the equipment's rated kW.

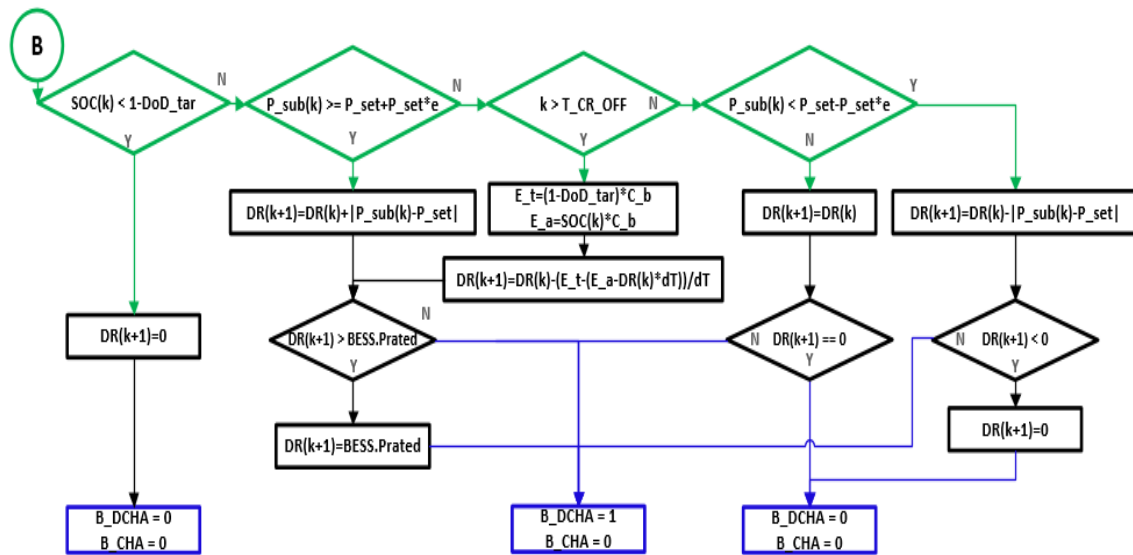
$$CR(k+1) = CR(k) + \frac{SOC_{ref}(k) - [SOC(k-1) + CR(k) \cdot \Delta t]}{\Delta t} \quad (5.20)$$

The last situation is simply the BESS operating under normal conditions, typically when minimal power deviations are observed or the SoC is within the 1% threshold. In such a situation, the BESS will follow the charge rate schedule produced by MEC-F1.



5.19: BESS Controller A - Enabled during a Solar Generation

The BESS charging mode of operation is scheduled to complete when the known CSI profile falls below the 10% threshold, originally determined by MEC-F1 on a day-to-day basis. Once time exceeds this estimate and DER-PV is generating less than 10% of its nameplate, Controller B is enabled and will operate sometime before the next solar generation window. MEC-F2 communicates with Controller B in regards to when peak shaving should be enabled, either during the present evening or coming morning. The exact time at which the peak shaving operation will commence (t_A) is determined by MEC-F3. Once time surpasses this threshold, Controller B will enforce the predetermined power level set point (P_{SET}) and alter the BESS's DR accordingly in order to hold the head-of-feeder load within a certain bandwidth (BW). The BW's size is dependent on the DNO's choice of the allowable percent error (e) currently fixed at 1%. Figure 5.20 displays the internal logic of controller B, providing known functionality of peak shaving operation and also guaranteeing the target DoD will be met before completion.



5.20: BESS Controller B - Enabled during a Peak Loading

Controller B is unique in that it constantly checks to see if the BESS's Depth of Discharge (DoD) is less than the MEC-F3 target DoD (DoD_t). If this condition is met, then the controller will continue the basic peak shaving functionality. If this condition is violated, then the DR is immediately set to 0kW and the BESS is placed in idling mode. When the estimated termination time of discharge (t_B) is exceeded, the controller will alter the DR in attempts to reach DoD_t . A limiter is enforced so that the calculated DR saturates at the equipment's rated kW. Incorporating this additional logic will ensure the BESS has the proper level of energy capacity in preparation for charging during the next day's DER-PV generation window.

Incorporating this high level of functionality enables the BESS to continuously operate and consecutively cycle throughout time, making it a powerful solution for BESS operation in a Smart Grid environment. At this point, the four components shown in Figure 5.14 have been explained in detail including the Master Energy Coordinator (MEC), an OLTC controller, a SC controller, and most importantly a novel BESS controller. To verify the operability between the centralized MEC and field agent controllers, QSTS simulation will be performed with OpenDSS on various single day scenarios of coincident load and PV generation and lastly a three day continuous run.

5.4 Benchmarking the Centralized MEC and Associated Field Agent Controllers

In order for the centralized MEC to possibly become an actual DER Management and Forecasting Controller, multiple simulations are required to observe the decisions made by the MEC and the responses of the OLTC, SC, and BESS controllers. Each simulation will introduce a unique scenario of coincident load and DER-PV

generation; further verifying the quality of interoperability between the MEC and field agents. Feeder 03 was selected for this benchmarking process with a hypothetical 3MW DER-PV facility connected downstream from the switch capacitor with its POI visualized in Figure 5.21. Referencing [53], a Utility T&D Advanced Lead Acid Battery Bank was selected with equipment characteristics provided in Table 5.3. This 1,000kW BESS, connected upstream of the 3MW DER-PV facility, has an energy capacity of 4,000kWh available for charging and discharging (per cycle) if respecting the rated DoD.

Table 5.3: Selected Advanced Lead Acid Battery Bank Characteristics

Parameter	Quantity
Output Power Maximum	1,000 kW
Total Energy Capacity ($C_{B, \text{rated}}$)	12,121 kWh
Depth of Discharge (DoD) Maximum	33%
Available Energy Capacity	4,000 kWh
Discharge Efficiency	96.7%
Charge Efficiency	93.0%
Roundtrip Efficiency	90.0%
Total Plant Cost (TPC)	4.855 Million \$
Plant Life (PL)	15 Years

The selected location of the BESS can of course be altered to a more optimum position with respect to feeder topology and load density. For demonstration purposes, this location was selected so that it was guaranteed the BESS will directly impact the OLTC operations and have the ability to supply power to both feeder main branches during peak shaving operation. Typically, a 1,000kW BESS has an associated controllable power converter (SVC) to transform the DC voltage to an AC synchronized waveform connected immediately before a 480V/12kV step-up transformer [53]. This converter must have communication avenues available to enable the MEC control in

setting reference charge rate schedules; SoC schedules, and a daily DoD target level. It must also have the capability to receive and transmit data packets to and from the master computer station. And lastly, the power converter must have onboard computational power to execute the proposed BESS control algorithm and instantly alter the control settings of the power converter to cycle the charging and discharging states.

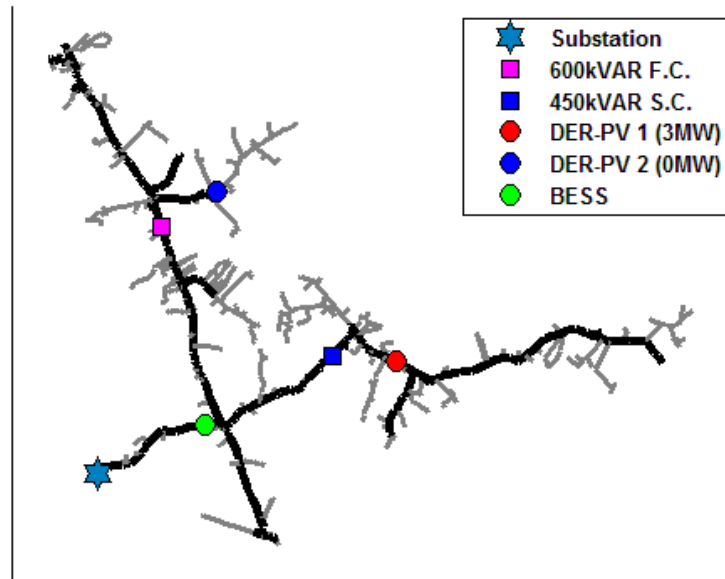


Figure 5.21: Feeder 03 Topology and Point of Interconnection Locations of Proposed DER-PV & BESS

Four single-day simulations were conducted, each introducing a different situation to the Master Energy Coordinator and the BESS controller. For comparison purposes, three scenarios per day were conducted including: base case without any DERs, with only the DER-PV connected, and lastly with the DER-PV and BESS connected. The DER-PV facility's output was controlled by historical POI measurements associated with Site #06, previously introduced in Chapter 4 Section 3 and utilized in Section 4. Before each 24 hours simulation, MEC-F2 was statically called to generate the target DoD from the

previous day to initialize the SoC of the BESS. Immediately before the DER-PV was projected to start generating, the CR reference profile was updated via MEC-F1 to reflect the initial state of charge of the BESS. Details on what each day's coincident load and solar energy profile introduced to the MEC and agent controllers are located below.

1. 5/24 introduced a DER-PV generation profile associated with a clear sky solar irradiance day. The feeder's daily load shape provided an evening peak condition.
2. 10/15 introduced a DER-PV generation profile associated with a highly variable solar irradiance day. The feeder's daily load shape did not have a pronounced peak but did still occur in the evening.
3. 2/3 introduced a DER-PV generation profile associated with a highly variable solar irradiance day. The feeder's daily load shape provided an evening peak condition but did not discharge to maximum DoD due to a MEC-F2 command.
4. 11/23 introduced a DER-PV generation profile associated with a low solar irradiance day. The feeder's daily load shape provided a morning peak condition.

The OpenDSS QSTS results of each 24 hour run are presented in Figures 5.22 through 5.26. Average simulation time with the MEC/BESS controllers implemented took approximately 7 minutes to complete, even under a 1 second resolution and a BESS charge/discharge dispatch rate of 5 seconds. Simulations were conducted on a P.C. with an Intel i5-3570 CPU @ 3.40GHz, 16GB of RAM, and a 64-bit Windows 10 O.S.

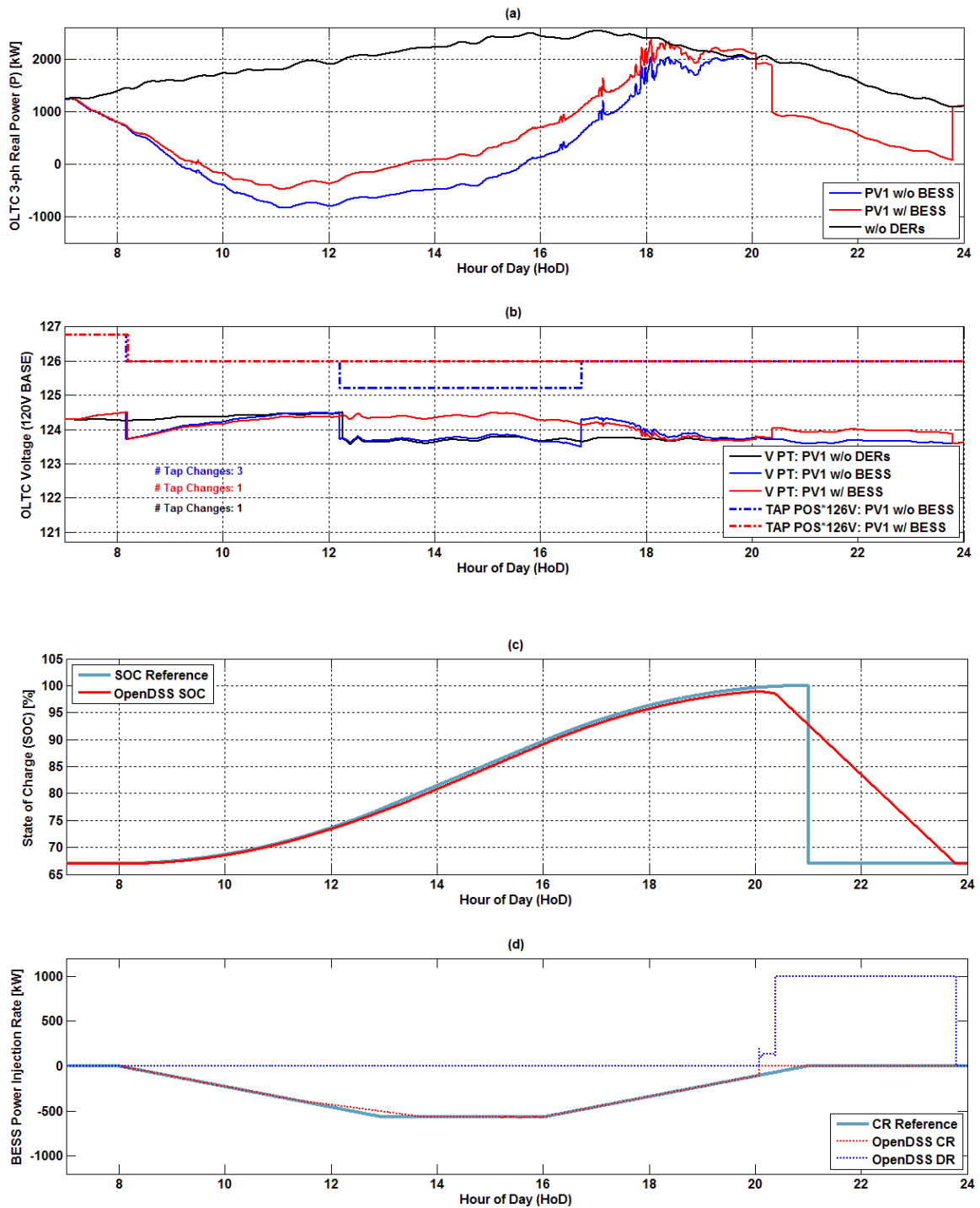


Figure 5.22: Results of Example Day #1 (5/24/2014); Stable DER-PV with Evening Peak and High Projected Next-Day Solar Energy

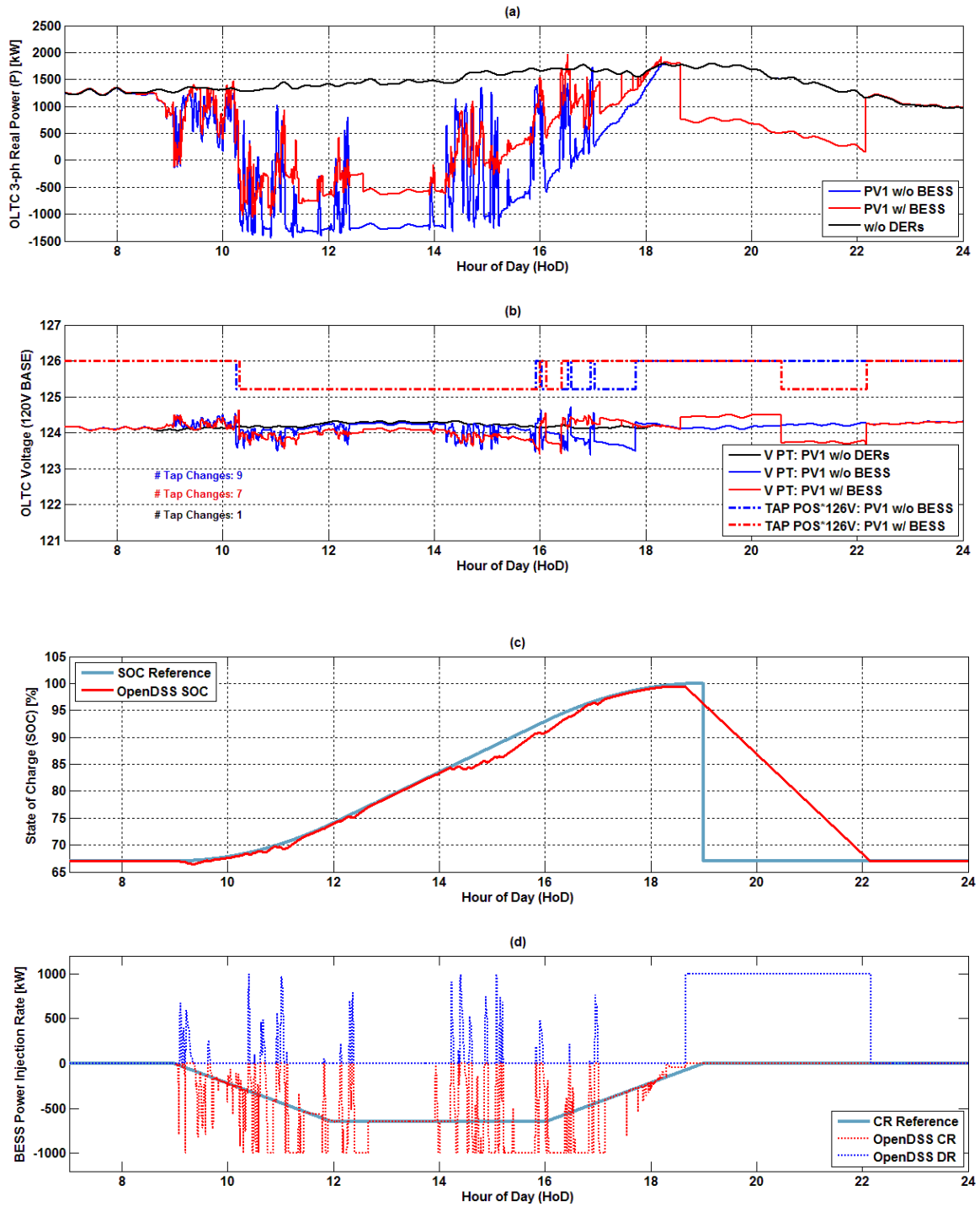


Figure 5.23: Results of Example Day #2 (10/15/2014); Highly Variable DER-PV with Evening Peak and High Projected Next-Day Solar Energy

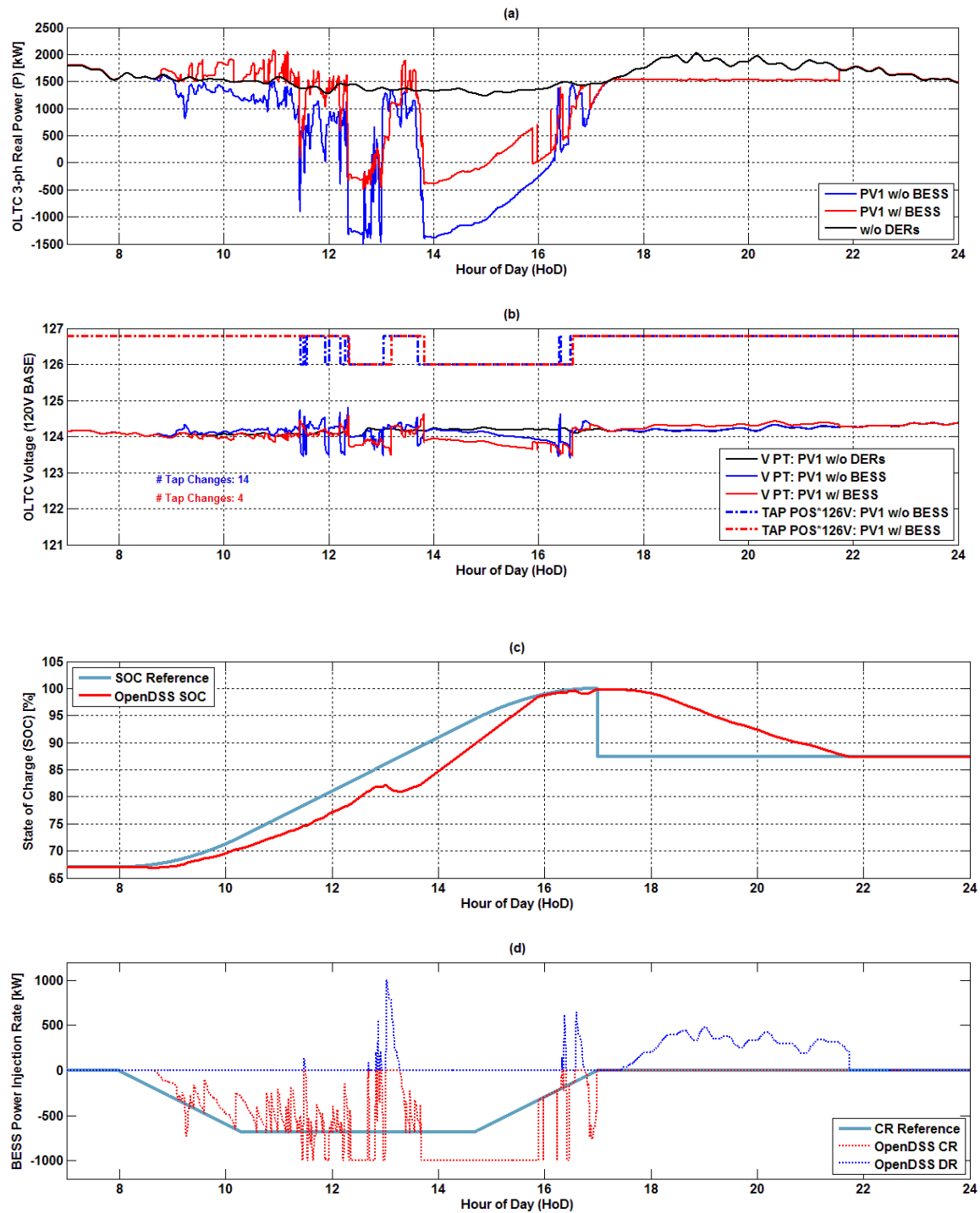


Figure 5.24: Results of Example Day #3 (2/3/2014); Variable DER-PV with Evening Peak and Below Average Projected Next-Day Solar Energy.

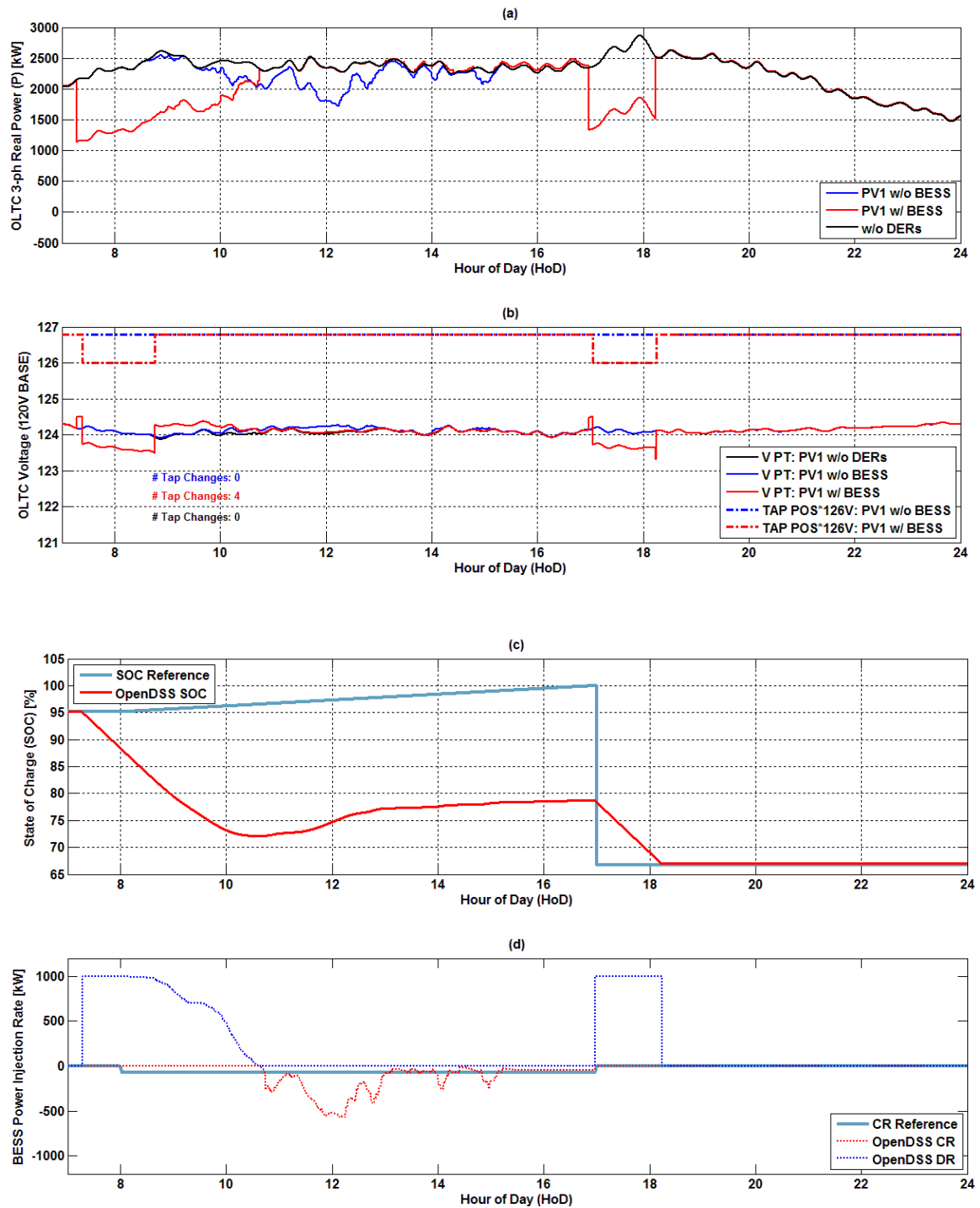


Figure 5.25: Results of Example Day #4 (11/23/2014); Low DER-PV with Morning Peak and High Projected Next-Day Solar Energy

Referencing the previous four pages, the figure (a)'s provide head-of-feeder three phase real power measurements from each DER deployment scenario. The figure (b)'s provide measured OLTC control voltage across the secondary winding Potential Transformer (PT) along with the tap position multiplied by 126 again from each DER deployment scenario. The figure (c)'s provide the MEC-F1 reference SoC profile along with actual BESS SoC trajectory. And lastly, figure (d)'s provide the MEC-F1 reference CR profile and the associated measured CR and DR captured via OpenDSS simulation.

From inspection, the OLTC controller sufficiently kept the head-of-feeder voltage within the constraints by initiating the necessary tap change after its internal timer exceeded the programmed time delay. The OLTC controller also successfully informed the BESS controller via Boolean indicators to amplify its response when violations occurred by observing the decrease in the number of cumulative tap changes on Days #1 through #3. Day #3 presented the stress from excessive tap changes being significantly alleviated when the number of tap changes decreased from 14 to 4. One negative side effect discovered when using the BESS for peak shaving is that the sudden decrease in load can result in additional boost / buck operations, as captured in Day #4.

Overall, the BESS Controller A performed exactly as expected, attempting to follow the scheduled SoC and recovering after extreme DER-PV ramping events. When observing the power flow results of Day #1, the BESS charge rate trajectory deviated very seldom away from the scheduled CR, thus operating exactly as expected. When observing the charge / discharge trajectories on Days #2 and #3, the short term change of rate functionality was confirmed to work properly. Short term discharging operation even

took place during these days to dampen the sudden increases in DER-PV generation (identified by the blue spikes of DR). Day #4 introduced a unique situation when the BESS was charged to only 78% SoC due to the DER-PV not generating above 10% of its nameplate the majority of the day. Fortunately, the DoD after the morning peak shaving event was set to 27% due to the MEC-F2 predicting the DER-PV was going to generate below average.

The BESS controller B also performed as expected with the BESS peak shaving operation occurring during the time intervals established by MEC-F3. During these time periods, the head-of-feeder load was held at the commanded P_{TH} level until either the peak shaving time period was surpassed or the target DoD was reached. Since these simulations were of 24 hour spans, a significant benefit of implementing this Master Energy Coordinator was not highlighted. Due to the robustness in logic, the MEC can sustain the BESS in cyclic operation over consecutive days by intelligently controlling the energy capacity available at the start of the solar PV charging period. To illustrate this, a three day consecutive simulation was conducted from 2/3 to 2/5. The original load shape and DER-PV generation load shapes experienced on Feeder 03 can be found in Figure 5.12 when the coordination between MEC-F2 and MEC-F3 was tested. The results of this QSTS simulation can be found below in Figure 5.26 providing the base case without any DERs, solely with the DER-PV in operation, and lastly with the BESS connected and controlled by this novel MEC. Day #1 provided an above average DER-PV energy yield while Days #2 and #3 experienced below average. Also, Day #1's load peaked during the evening hours while Day #3's load peaked during the morning hours.

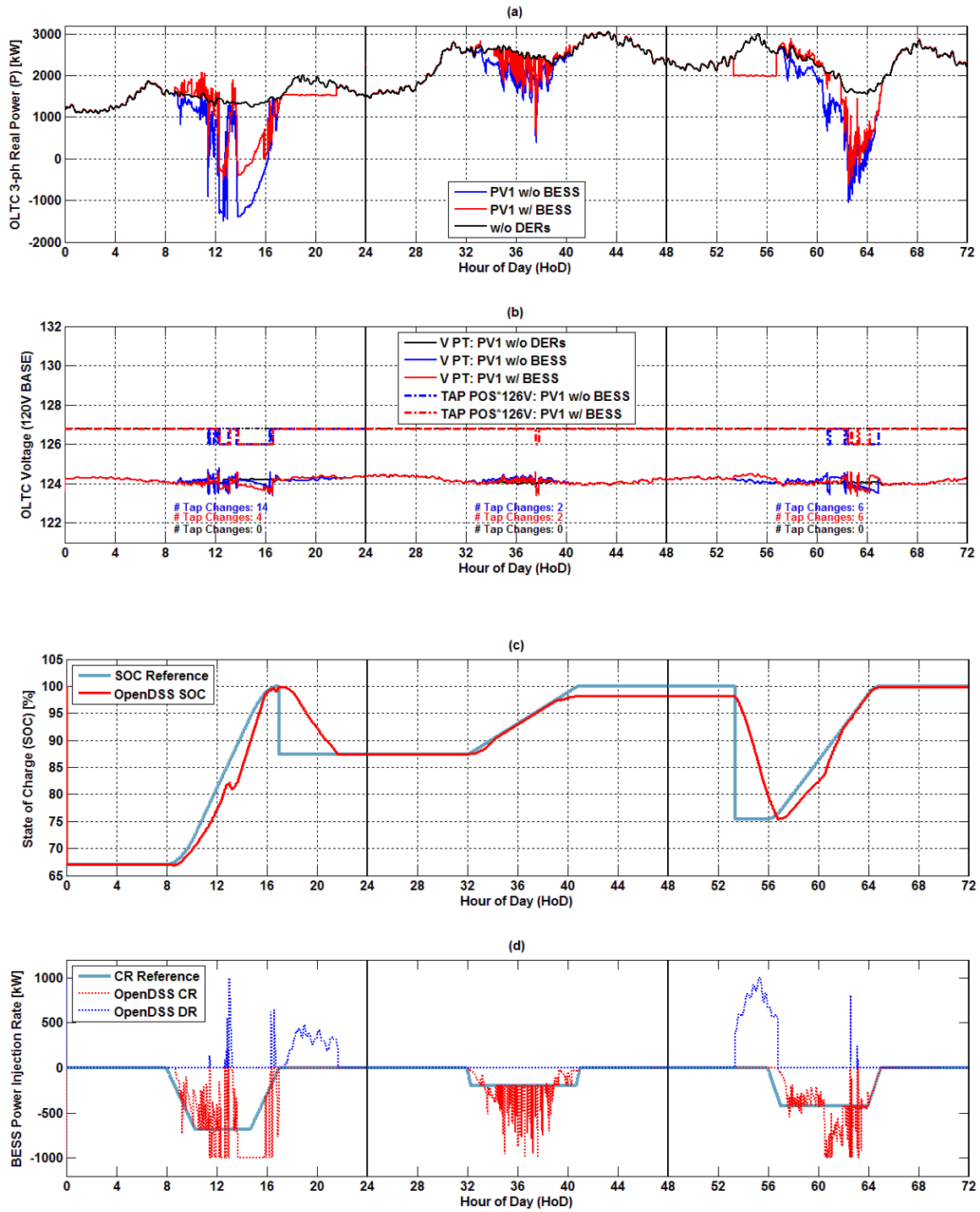


Figure 5.26: Results of a Consecutive Three Day Run (2/3 to 2/5)

The BESS was successfully charged to the target SoC on Days #1 and #3 but was not able to during Day #2. This was due to the DER-PV dropped below the 10% nameplate threshold before the charging period was complete. Inspecting the BESS charge and discharge rates provides insight into how the BESS was dispatched through the variable DER-PV generation window and peak shaving operation. The BESS output varied successfully to dampen the effect of extreme DER-PV ramp rate events. Two peak shaving events occurred during this three day simulation due to MEC-F2 predicting a morning peak during Day #3 and correspondingly holding the stored energy from Day #2 until approximately 5AM (Hour 53).

Illustrated in this example, the BESS can be considered a dispatchable generation source and utilized by network operators to combat resulting extreme ramping of conventional generation during the morning or evening transition periods. The future distribution grid is guaranteed to experience a high penetration of distributed energy resources. With the uncontrollable nature of renewable energy sources now generating electricity reaching a significant penetration level, DNOs and ISOs will require additional sensing/monitoring, control, and protection. Advanced two-way communication between controllable network devices will facilitate Advanced Distribution Automation necessary if implementing DER management and forecasting control algorithms such as the proposed Master Energy Coordinator (MEC).

Dispersing battery energy storage systems on the individual distribution feeder level is just one possible solution to mitigating the adverse operational tap changer stresses and OOF voltage conditions introduced with DER-PV generation. If IEEE 1547

is revised to allow PV inverters to participate in voltage regulation, the need for a DER management system (DERMS) will be even more prominent. A DERMS platform will need to be capable of accepting numerous field measurement points and dispatching commands to all controllable equipment such as automatic switches, OLTC/SVRs, SCs, BESSs, and DER-PV Inverters.

In conclusion, the Master Energy Coordinator coherently establishes when the feeder-connected BESS should charge during a DER-PV's generation window and even when the BESS should discharge during the distribution network's peak loading condition. This coordination scheme and associated equipment controllers fulfilled the three main goals of mitigating reverse power flow and long-term high voltage events, decreasing the additional operational stress on the OLTCs by dampening the extreme short-term generation ramp rates, and lastly discharge the captured energy during the most cost effective times. The standard practices Distribution Network Operators followed for years were designed based off the assumption power flowing from the utility connection point to connected loads. With the advent of DER-PV, this assumption is nullified due to power injection points being hosted downstream from the substation and if surpassing local load will introduce reversing power flow. Grid Modernization initiatives can find solutions to alleviate operational issues that can arise by integrating new technology and control schemes into the existing network's voltage regulation techniques. Distribution networks have potential to host significant amounts of renewable generation. For this to become a reality, it is essential that existing DNO platform management systems migrate to incorporate advanced DER coordination techniques.

REFERENCES

- [1] A. Clarke, "Steps Toward a Net-Zero Campus with Renewable Energy Resources," Paper 1416, All Dissertations, Clemson University, http://tigerprints.clemson.edu/all_dissertations/1416, 2014.
- [2] S. Electric. (2014, 10/1/2014). *Optimize enterprise energy performance with StruxureWare software*. Available: <http://www2.schneider-electric.com/sites/australia/en/solutions/struxureware/struxureware-applications.page>
- [3] M. J. Reno, A. Ellis, J. Quiroz, and S. Grijalva, "Modeling Distribution System Impacts of Solar Variability and Interconnection Location," in *3rd European American Solar Deployment Conference (PV Rollout)*, 2013.
- [4] T. O. Company. (2014). *Okoguard-Okoseal Type MV-105, 15kV Shielded Power Cable*. Available: http://okonite.com/Product_Catalog/section2/section2-pdfs/2-8.pdf
- [5] W. H. Kersting, *Distribution System Modeling and Analysis*, 3 ed.: CRC Press, 2002.
- [6] G. M. Masters, *Renewable and Efficient Electric Power Systems*, 2 ed.: IEEE Press, 2013.
- [7] C. Ameresco Solar - Green, Sustainable. (2012). *190W and 200W Photovoltaic Modules 4190J and 4200J*. Available: <http://www.amerescosolar.com/sites/default/files/Ameresco%20Solar%204200J.pdf>
- [8] J. L. W. W. J. Xiang, "A Simple Sizing Algorithm for Stand-Alone PV/Wind/Battery Hybrid Microgrids," *Energies*, vol. 5, 2012.
- [9] P. K. C. Wong, R. A. Barr, and A. Kalam, "Voltage rise impacts and generation modeling of residential roof-top photo-voltaic systems," in *Harmonics and Quality of Power (ICHQP), 2014 IEEE 16th International Conference on*, 2014, pp. 229-233.
- [10] N. P. Papanikolaou, E. C. Tatakis, and A. C. Kyritsis, "Analytical model for PV - Distributed generators, suitable for power systems studies," in *Power Electronics and Applications, 2009. EPE '09. 13th European Conference on*, 2009, pp. 1-10.
- [11] C. B. White. (2015). *Utility-scale solar in South Atlantic region dominated by North Carolina, Georgia*. Available: <https://www.eia.gov/todayinenergy/detail.cfm?id=24192>
- [12] Eaton. (2016). *CYME Power Engineering Software, Distribution System Analysis*. Available: <http://www.cyme.com/software/cymdist/>
- [13] I. American National Standards Institute, "ANSI C84.1 - American National Standard For Electric Power Systems and Equipment- Voltage Ratings (60 Hertz)," ed. Rosslyn, VA: National Electrical Manufacturers Association, 2011.
- [14] H. Wan, J. D. McCalley, and V. Vittal, "Increasing thermal rating by risk analysis," *IEEE Transactions on Power Systems*, vol. 14, pp. 815-828, 1999.
- [15] T. A. Short, *Electric Power Distribution Handbook*, 1 ed. Boca Raton, FL: CRC Press, Taylor & Francis Group, 2003.

- [16] T. Gonen, *Electric Power Distribution Engineering*, 3 ed. Boca Raton, FL: CRC Press, Taylor & Francis Group, 2014.
- [17] MERRA, "Wind Speed Measurements," M. a. A. a. I. S. C. (MDISC), Ed., ed: NASA, 2015.
- [18] EPRI, "Alternatives to the 15% Rule: Final Project Summary," Palo Alto, CA 3002006594, 2015.
- [19] G. C. Lampley, "Volt/VAR control at Progress Energy Carolinas past, present and future," in *Power and Energy Society General Meeting, 2010 IEEE*, 2010, pp. 1-3.
- [20] EPRI. (2015). *Open Distribution System Simulator (OpenDSS)*. Available: <http://sourceforge.net/projects/electricdss/>
- [21] M. J. Reno and K. Coogan, "Grid Integrated Distributed PV (GridPV) Version 2," Sandia National Labs, SAND2014-20141.
- [22] M. S. Thomas and J. D. McDonald, *Power System SCADA and Smart Grids*. Boca Raton, FL: CRC Press, Taylor & Francis Group, 2015.
- [23] N. E. C. Cornwall. (2015). *Solar Position Calculator*. Available: <http://www.esrl.noaa.gov/gmd/grad/solcalc/azel.html>
- [24] R. L. Ott and M. Longnecker, *An Introduction to Statistical Methods and Data Analysis*, 6 ed. Belmont, CA: Brooks/Cole CENAGE Learning, 2010.
- [25] K. Coogan, M. J. Reno, S. Grijalva, and R. J. Broderick, "Locational dependence of PV hosting capacity correlated with feeder load," in *T&D Conference and Exposition, 2014 IEEE PES*, 2014, pp. 1-5.
- [26] R. Seguin, J. Woyak, D. Costyk, J. Hambrick, and B. Mather, "High-Penetration PV Integration Handbook for Distribution Engineers," January 2016.
- [27] S. Ong, C. Campbell, P. Denholm, R. Margolis, and G. Heath, "Land-Use Requirements for Solar Power Plants in the United States," June 2013.
- [28] R. van Haaren, M. Morjaria, and V. Fthenakis, "Empirical assessment of short-term variability from utility-scale solar PV plants," *Progress in Photovoltaics: Research and Applications*, vol. 22, pp. 548-559, 2014.
- [29] J. E. Quiroz, M. J. Reno, and R. J. Broderick, "Time series simulation of voltage regulation device control modes," in *Photovoltaic Specialists Conference (PVSC), 2013 IEEE 39th*, 2013, pp. 1700-1705.
- [30] R. J. Broderick, J. E. Quiroz, M. J. Reno, A. Ellis, J. Smith, and R. Dugan, "Time Series Power Flow Analysis for Distribution Connected PV Generation," Sandia National Laboratories, SAND2013-0537, Albuquerque, New Mexico 2013.
- [31] C. P. Systems. (1992). *Cooper Power System's VR-32 Regulator and CL-2A Control Installation, Operation and Maintenance Instructions Parts Replacement Information*. Available: http://www.cooperindustries.com/content/dam/public/powersystems/resources/library/225_VoltageRegulators/S225105.pdf
- [32] Y. Agalgaonkar, B. C. Pal, and R. A. Jabr, "Distribution voltage control considering the impact of PV generation on tap changers and autonomous regulators," in *PES General Meeting / Conference & Exposition, 2014 IEEE*, 2014, pp. 1-1.

- [33] M. McGranaghan, T. Ortmeier, D. Crudele, T. Key, J. Smith, and P. Barker, "Renewable Systems Interconnection Study: Advanced Grid Planning and Operations " Sandia National Laboratories SAND2008-0944 P Albuquerque, New Mexico 2008.
- [34] L. Ruey-Hsun and C. Chen-Kuo, "Dispatch of main transformer ULTC and capacitors in a distribution system," *IEEE Transactions on Power Delivery*, vol. 16, pp. 625-630, 2001.
- [35] M. Prevallet and T. Johnson. (2013). *Integrated Volt/VAR Control* Available: http://assets.fiercemarkets.net/public/smartgridnews/Optimizing_Voltage.pdf
- [36] J. S. Stein, C. W. Hansen, and M. J. Reno, "The Variability Index: A New and Novel Metric for Quantifying Irradiance and PV Output Variability," *World Renewable Energy Forum, Denver, CO*, 2012.
- [37] M. J. Reno, C. W. Hansen, and J. S. Stein, "Global Horizontal Irradiance Clear Sky Models: Implementation and Analysis," Sandia National Laboratories SAND2012-2389, Albuquerque, New Mexico 2012.
- [38] P. Ineichen and R. Perez, "A new airmass independent formulation for the Linke turbidity coefficient," *Solar Energy*, vol. 73, pp. 151-157, 2002.
- [39] M. Kashem, A. Le, L. Gerard, and N. Michael, "Minimising Voltage Deviation in Distribution Feeders by Optimising Size and Location of Distributed Generation," presented at the AUPEC 2005 CD Proceedings: Australasian Universities Power Engineering Conference, Tasmania, Australia, 2005.
- [40] P. Kruger, *Alternative Energy Resources. The Quest for Sustainable Energy* vol. 1. Hoboken, New Jersey: John Wiley & Sons, Inc., 2006.
- [41] A. Mohd, E. Ortjohann, A. Schmelter, N. Hamsic, and D. Morton, "Challenges in integrating distributed Energy storage systems into future smart grid," in *2008 IEEE International Symposium on Industrial Electronics*, 2008, pp. 1627-1632.
- [42] S. Jahdi, O. Alatise, and P. A. Mawby, "The impact of silicon carbide technology on grid-connected Distributed Energy resources," in *IEEE PES ISGT Europe 2013*, 2013, pp. 1-5.
- [43] P. Denholm, M. O'Connell, G. Brinkman, and J. Jorgenson, "Overgeneration from Solar Energy in California: A Field Guide to the Duck Chart," Golden, CO 2015.
- [44] Y. P. Agalgaonkar, B. C. Pal, and R. A. Jabr, "Distribution Voltage Control Considering the Impact of PV Generation on Tap Changers and Autonomous Regulators," *IEEE Transactions on Power Systems*, vol. 29, pp. 182-192, 2014.
- [45] "IEEE Standard for Interconnecting Distributed Resources with Electric Power Systems - Amendment 1," *IEEE Std 1547a-2014 (Amendment to IEEE Std 1547-2003)*, pp. 1-16, 2014.
- [46] H. E. Farag, E. F. El-Saadany, and R. Seethapathy, "A Two Ways Communication-Based Distributed Control for Voltage Regulation in Smart Distribution Feeders," *IEEE Transactions on Smart Grid*, vol. 3, pp. 271-281, 2012.
- [47] K. Moslehi and R. Kumar, "A Reliability Perspective of the Smart Grid," *IEEE Transactions on Smart Grid*, vol. 1, pp. 57-64, 2010.

- [48] A. R. Malekpour and A. Pahwa, "Reactive power and voltage control in distribution systems with photovoltaic generation," in *North American Power Symposium (NAPS), 2012*, 2012, pp. 1-6.
- [49] X. Liu, A. Aichhorn, L. Liu, and H. Li, "Coordinated Control of Distributed Energy Storage System With Tap Changer Transformers for Voltage Rise Mitigation Under High Photovoltaic Penetration," *IEEE Transactions on Smart Grid*, vol. 3, pp. 897-906, 2012.
- [50] M. Venkata and G. Brice. (2015). *Next Generation Distribution Management Systems (DMS) and Distributed Energy Resource Management Systems (DERMS)*. Available: http://www.nrel.gov/esi/pdfs/agct_day1_venkata.pdf
- [51] M. J. E. Alam, K. M. Muttaqi, and D. Sutanto, "Mitigation of Rooftop Solar PV Impacts and Evening Peak Support by Managing Available Capacity of Distributed Energy Storage Systems," *IEEE Transactions on Power Systems*, vol. 28, pp. 3874-3884, 2013.
- [52] H. I. Elsayed, S. R. Chaudhry, and A. A. A. Al-Mahmoud, "PV, battery storage and energy conversion system for meeting peak load in a substation," in *Integration of Renewables into the Distribution Grid, CIRED 2012 Workshop*, 2012, pp. 1-4.
- [53] A. A. Akhil, G. Huff, A. B. Currier, B. C. Kaun, D. M. Rastler, S. B. Chen, *et al.*, "DOE/EPRI 2013 Electricity Storage Handbook in Collaboration with NRECA," Albuquerque, New Mexico 2013.